DELFT UNIVERSITY OF TECHNOLOGY

GRADUATE THESIS

Generating chip-to-chip entanglement by measurement with transmon qubits using engineered driving fields

Author:
J.J. WESDORP

Supervisor:
C. DICKEL
L. DICARLO

A thesis submitted in fulfillment of the requirements
for the degree of Master of Science

in

Qutech
Department of Quantum Nanoscience

September 30, 2017

Delft University of Technology

Abstract

Applied Physics
Department of Quantum Nanoscience

Master of Science

Generating chip-to-chip entanglement by measurement with transmon qubits using engineered driving fields

by J.J. WESDORP

We generate entanglement between two transmon qubits each coupled to a readout resonator and located on different chips via engineering a half-parity measurement. This measurement does not distinguish $|01\rangle$ from $|10\rangle$, thus if started in an initial full two-qubit superposition it will project the qubits to an odd Bell state 50% of the time. By post-selecting on measurement outcomes corresponding to $|00\rangle$ or $|11\rangle$ we have generated Bell-states of 51% (40%) concurrence or 75% (70%) Bell-state fidelity keeping 25% (50%) of the data. With a repetition rate of 5KHz based on state initialization by T_1 this corresponds to a 1KHz generation rate. We show that changing the cavity frequencies with tuning qubits and by driving with a second compensation pulse in a weakly coupled port we can reduce residual distinguishability in the odd subspace, making the protocol robust to fabrication imperfections. By shaping the pulse of the compensation drive we also generate an even-parity Bell state of similar concurrence. We found that thermal excitation results in an overestimate of concurrence in state tomography and show a simple method to correct for this by assuming mixed calibration points. We find good agreement of unconditioned measurement dynamics with theory using a reduced two-qubit only master equation. A 45% measurement efficiency was found using a stochastic master equation to model final state concurrence conditioned on the measurement result. This protocol could be used in modular 2D quantum computing architectures where entanglement is distributed with itinerant photons.

Contents

1 Introduction

This chapter will start with introducing the role of quantum computing in history in sec. 1.1. I will then explain some algorithms and communication schemes that could give a gain over classical technology. This is necessary, because a key element in all quantum algorithms is entanglement. After this, a brief introduction to quantum information processing and the important concept of measurement is provided in sec. 1.2. This project is about generating entanglement between two superconducting chips by doing a measurement, so the Chapter concludes with an overview of the protocol and comparable protocols demonstrated recently in sec. 1.3.

1.1 Quantum technology

Since the *first quantum revolution* in the 20th century by great physicists like Paul Dirac and Werner Heisenberg - where they explained fundamental flaws in our theory of nature - quantum Mechanics has become useful in many technological applications. By understanding that electrons can behave like waves and light as particles (photons) we have been able to improve core technologies that underpin the modern society, e.g the semiconductor industry found in all electronic devices, the accelerometer in your phone or solar cells as a renewable energy source. In the 21st century we have reached a stage where we not only use quantum mechanics to explain and improve technology, but actually use it to create completely new technology. This *second quantum revolution* [26] utilizes quantized states of matter and light and superpositions thereof to perform a fundamentally new way of computation, communication and simulation [29]. The field of quantum information processing [62] has matured rapidly in the last two decades and is now in active development by universities working together with industry giants such as Google, Intel, IBM and Microsoft [16, 17, 43, 44, 65].

1.1.1 Quantum computing and communication

A *quantum computer* - if physically realized - is often said to be able to give *exponential* speedup over its classical counterparts. Yes, the amount of information contained in N quantum bits is exponentially larger than that can be stored in N classical bits, but the difficulty lies in retrieving this information. A measurement of a quantum system probabilistically converts the information to a classical bit, so an exponential amount of measurements is needed to retrieve the stored information, nullifying the speedup! It is for this reason that relatively few realistic quantum algorithms have been developed able to obtain this, but nevertheless these do exist! The three well known are Shors algorithm [71] for exponentially speeding up the factoring of prime numbers, Grovers algorithm for quadratically speeding up database searches [40] and the Deutsch-Josza

algorithm [21] exponentially speeding up determining whether a function is balanced or not.

Prime factorization being a computationally hard problem is the key to modern RSA encryption systems. These are used in Internet-security and are the basis for the Http-secure protocol found in nearly all web pages. A quantum computer would allow one to break this security in polynomial time rendering the encryption useless. Paradoxically the field of *quantum communication* fixes this by introducing communication protocols between two parties that cannot be eavesdropped upon by a malicious third party without the first two knowing this [28].

1.1.2 Entanglement

Entanglement plays a key role in the functioning of the quantum algorithms and communication protocol defined above, but also in quantum networking [48, 6] and quantum teleportation [7]. Entanglement is the simple fact that there exist quantum states of two or more combined systems that cannot be written as a product of the individual systems. This means that there will always be a correlation between measurement outcomes of the individual systems. Entanglement was originally used as an argument *against* the validity of quantum mechanics by Einstein, Podolsky and Rosen [27] because it results in non-local interactions violating the local realism principles of general relativity. Bell [5] devised a test to check whether or not quantum mechanics could have a more fundamental underlying hidden-variables theory which in the 90's and more recently [41] was performed on real physical systems. Up to date all such experiments have pointed in favor of quantum mechanics and against local realism. Yet in these thesis we take a more practical approach and view entanglement simply as a resource needed for quantum information processing.

1.1.3 Distribution of entanglement

In order to make an actual quantum computer that is both useful and physically realizable D.DiVincenzo posed his famous 7 criteria [23]. These specified quantitative requirements on operation quality in order to reach fault tolerant computation. A problem that arose in many fault-tolerant computation schemes was the fact that most of them assumed two-qubit operations were possible between any pair of qubits. They only considered two-qubit operations since universal computation can be performed with only single qubit gates and one two qubit gate, e.g a CNOT gate. The practical constraint of only being able to do local operations, shortly led to the believe fault-tolerance was not achievable after all. A solution to this was proposed in the form of a 2-D fault-tolerance scheme requiring only local operations and measurements called surface-code [49]. Even though this solution avoids non-local operations on a chip, it is nevertheless interesting to look at possible schemes to do so and even more, look into schemes that allow operations between two chips! A modular quantum computing architecture would then be possible, linking up quantum processors with using photonic interconnects that preserve quantum information, a road that has been looked into for ion trap processors for example [54].

1.2 Information processing theory

1.2.1 Qubits and the density matrix

Quantum information processing is based on the quantum analog of the fundamental resource of classical computing: the quantum bit, or qubit in short. Besides the classical states $|0\rangle$ and $|1\rangle$ the qubit can also be in an arbitrary superposition of these two states $|\psi\rangle = \alpha |0\rangle + \beta |1\rangle$, which fundamentally distinguishes it from the classical bit and allows for a much richer set of algorithms and applications. When measure the bit we will always get a classical outcome limiting the obtained information(described quantitatively by Holevo's bound). The art in most quantum algorithms is therefore be about reducing the final outcome of its computation to a simple yes or no answer [40].

A system state $|\psi\rangle$ is revered to as a *pure state*. In reality and in most part of this experiment, we do not know in which state our system is exactly. So how do we describe partial knowledge about the system state? We can describe the system as being a mixture of pure states. For example, if we know that we had 50% change to initialize the system in $|0\rangle$ and 50% to initialize it in $|1\rangle$ we can describe the system by a *density operator* ρ, originally introduced by Von Neumann to ease calculations in quantum statistical mechanics [61]. In general any such mixture can be written as

$$\rho = \sum_i p_i |\psi_i\rangle \langle\psi_i| \tag{1.1}$$

where p_i is the probability for the system to be in state $|\psi_i\rangle$ and $\sum_i p_i = 1$ since the total probability to find a state must sum up to 1. For any finite dimensional system ρ can be written as a matrix and $|\psi\rangle$ as a vector, reducing most computations to an exercise of linear algebra. Normalization of the constituent pure states $|\psi_i\rangle$ results in the condition $\mathrm{Tr}\,(\rho) = 1$ for it to represent a physical system. An important property of the density matrix is its purity given by $\mathrm{Tr}\,(\rho^2)$ which is for a d-dimensional system a number between $\frac{1}{d}$ - indicating a maximally mixed state - and 1 - indicating a pure state. Another important property of density matrices is the ability to trace out subsystems using the *partial trace* [62]. This will allow us in simulations of both a resonator and a qubit to look at the qubits alone for example.

1.2.2 Fidelity

An important quantity used to compare two quantum states ρ, σ is the *fidelity* given by

$$\mathcal{F}\,(\rho, \sigma) = \mathrm{Tr}\,(\sqrt{\rho}\sigma\sqrt{\rho}) \tag{1.2}$$

which is symmetric in its arguments and lies between 0 and 1, where 1 indicates $\rho = \sigma$. Since the density operators represent an ensemble of pure states, we can see them as a probability distribution over these states. The fidelity can be seen as a quantum version of the overlap of these probability distributions, thus giving a measure of closeness of the two quantum states. In the case where ρ and σ have the same eigenvectors with different eigenvalues r_i, s_i respectively, the fidelity reduces to $\mathcal{F} = \sum_i \sqrt{r_i s_i}$, which is the classical fidelity between two probability distributions. We will use $\mathcal{F}$ extensively in this thesis to compare data and theoretical simulations.

1.2.3   Entanglement measures

Mathematically two states are entangled if their combined state cannot be written as a tensor product of the subsystems $|\psi_{AB}\rangle \neq |\psi_A\rangle \otimes |\psi_B\rangle$. This experiment is about entanglement generation, so how do we quantify how much entanglement we have generated? An often used number reported in literature is to use the fidelity of Eq. 1.2 to a state of *maximal entanglement*, which for our two qubit case are defined as

$$|\beta_{even}\rangle = \frac{|00\rangle + e^{i\phi}\,|11\rangle}{\sqrt{2}}, \qquad |\beta_{odd}\rangle = \frac{|01\rangle + e^{i\phi}\,|10\rangle}{\sqrt{2}} \tag{1.3}$$

where ϕ can be any phase. They are maximally entangled since if you measure the state of one of the qubits you know with certainty the state of the other. For states that have less than unity fidelity to any of the Bell states you thus gain only partial knowledge on the state of the other qubit by measuring the first.

Another often used measure of entanglement of the density matrix of two qubits is the *concurrence* [42] given by

$$\mathcal{C}\left(\rho\right) = \max\left(0, \lambda_1 - \lambda_2 - \lambda_3 - \lambda_4\right) \tag{1.4}$$

where λ_i are the ordered set of eigenvalues of the matrix $\sqrt{\sqrt{\rho}\left(\sigma_y \otimes \sigma_y\right)\rho^*\left(\sigma_y \otimes \sigma_y\right)\sqrt{\rho}}$ where σ_i are the Pauli spin matrices defined in Eq. 4.2 This has the advantage that it does not require a Bell state to compare to and it is also monotonically increasing in the amount of entanglement. Concurrence is a number between $0 \leq \mathcal{C}\left(\rho\right) \leq 1$, where 0 indicates no entanglement and 1 indicates a maximally entangled state.

1.2.4   Quantum measurements

The way we generate entanglement is by doing a measurement, but we also use it to actually know which state we ended up with via state tomography in Ch. 4. It is therefore useful to explain it in a formal way. We can describe a measurement by any set of measurement operators $\{A_m\}$. Doing a measurement probabilistically gives back a value m corresponding to measurement operator A_m, where the chance to obtain value m depends on the system state ρ being measured according to

$$p\left(m\right) = \mathrm{Tr}\left(\hat{A}_m^\dagger \hat{A}_m \rho\right) \tag{1.5}$$

The resulting state that we obtain is then given by

$$\rho_m = \frac{\hat{A}_m \rho \hat{A}^\dagger}{p\left(m\right)} \tag{1.6}$$

From the above equations we see that for the total probability of a measurement outcome to be one, we require $\sum_m \hat{A_m}^\dagger \hat{A_m} = I$. This construct is useful because it allows to describe both a "discrete" projective measurement and a continuous weak measurement based on the form of the A_m. A projective measurement was the kind originally described by the Born-rule, where we have an observable $\hat{M} = \sum_{j=0}^d m_j \hat{P}_{m_j}$ where $\hat{P}_{m_j} = |m_j\rangle\langle m_j|$ is the projector onto the eigenstate $|m_j\rangle$ of $\hat{M}$ corresponding to eigenvalue m_j and $\sum_j \hat{P}_{m_j} = I$. Note that the resulting states of this measurement will

be one of the $|m_j\rangle$ regardless of ρ. This is one of the main postulates of quantum mechanics: if we measure an observable we obtain one of its eigenstates with probability $\text{Tr}\,(|m_j\rangle \langle m_j| \rho)$. When we introduced density matrices we were to be able to describe partial information on a quantum state. This can be extended to the case of weak or indirect measurements where we - by looking at the measurement outcome - only obtain partial information on the system ρ. We can describe this by taking the A_m *not* to be projectors, but rather close to the identity. Say for example we have

$$A_0 = p\,|0\rangle \langle 0| + \frac{I}{2}, \qquad A_1 = \frac{I}{2} - p\,|0\rangle \langle 0| \tag{1.7}$$

If we measure outcome 0 we can say that we now have a higher chance that our state is actually 0 than we did before and if we measure 1 we know it has a higher chance to be one of the others. The previous sentence is essentially describing a Bayesian update on our probabilistic estimate of the state given a certain measurement outcome. With superconducting qubits we are often doing these *weak measurements* by looking at microwave photons coming from a cavity transformed to an integrated voltage over time, obtaining information about the state gradually [12]. We discuss the physics of this process in detail for a single qubit system in sec. 2.5.3, but we can view this as the value of p in the above story being an increasing function of the time interval we measure. In this way, a short measurement would give $p \ll 1$ and therefore only a small update on our knowledge of the state while measuring for a long time, e.g $p = \frac{1}{2}$ turns the measurement operator into a projector, ending up with a pure state.

1.2.5 Quantum non-demolition measurements

An important requirement for being able to do weak measurements to determine the original system state is the measurement being *quantum non-demolition* [11]. This essentially means we can measure the state without changing the original probability distribution of measurement outcomes. This can only be the case if the coupling term of in the Hamiltonian governing both the system and our observing system *commutes* with the system Hamiltonian. Otherwise due to time evolution of the Schrödinger equation the system will no longer be in an eigenstate of the original system, potentially changing the outcome probability distribution.

1.3 Research goal and outline

The goal of this research is to create entanglement between two superconducting Transmon qubits [50] on separate chips by performing a joint measurement on them. We use these 2D qubits because of their promising application in scalable quantum computer architectures. A similar experiment has been performed by Roch et al. [68] using 3D copper cavities instead of 2D transmons. The key concept in any entanglement by measurement scheme is *indistinguishability* of the measurement outcomes corresponding to the subspace one wants to entangle. We create this entanglement by using a continuous traveling coherent microwave light field entangling with both qubits before being amplified and subsequently measured. This has a high success rate(50% as explained below) and can even be made deterministic using feedback [57], already demonstrated

in two qubits coupled to the same resonator in [67, 76]. Recent other proposals for making use of the erasure of distinguishability has been proposed through using a phase-preserving amplifier [72] or using a beam-splitter with single photons [63, 59].
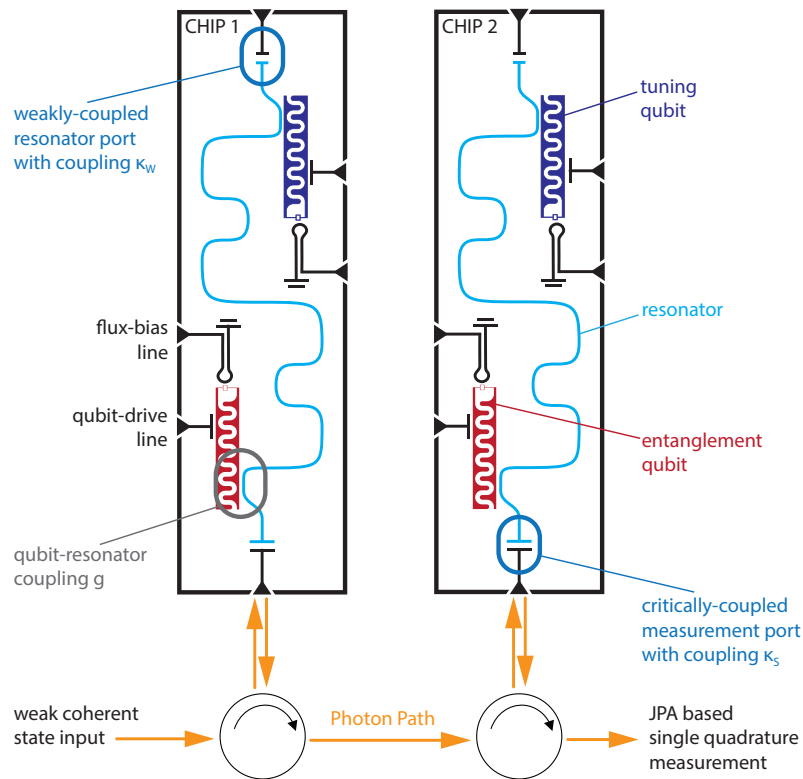
FIGURE 1.1: Schematic layout of the experiment. Measurement photons enter from the left through the strongly coupled ports. They are then reflected by a qubit state dependent reflection coefficient of each cavity in a cascaded manner. This generates entanglement between the measurement photons and the (red) entanglement qubits on both chips. The photons are subsequently read out, probabilistically projecting the qubits in an entangled subspace. Directionality is enforced by microwave circulators. Tuning qubits are included to allow for resonator tuning, improving the final state concurrence.

1.3.1   Basic scheme of the experiment

In Figure 1.1 we can see that we measure the 'entangling qubits' located on separate chips by sending photons through a feed line that is capacitively coupled to the two separate microwave cavities that are strongly coupled to these qubits. The input fields reflects off both cavities obtaining a qubit state dependent phase shift due to the dispersive interaction of the qubit with the cavity. This *entangles* the reflected photons with both cavities and we can then transfer this entanglement to the qubits alone by measuring the photons.

The measurement performed is a near perfect half parity measurement given by the operator $\hat{E} = \sigma_{z_1} + \sigma_{z_2}$, where σ_{z_i} is the Pauli z matrix on qubit i. We now start in a superposition state $|\psi\rangle = \frac{1}{2}(|00\rangle + |01\rangle + |10\rangle + |11\rangle)$, which can be created easily by local single qubit operations. Applying $\hat{E}$ to our state ψ gives identical output fields for the states $|01\rangle$ and $|10\rangle$ and we can fundamentally *not distinguish* these two states in our measurement, this thus projects the system into an odd bell state $\beta_{odd} = |01\rangle + |10\rangle$. We

can however tell $|00\rangle$ and $|11\rangle$ apart such that by starting with $|\psi\rangle$ we can at most get the measurement outcome that corresponds to projecting into the odd subspace 50% of the time and post-selection on the measurement outcome is required to herald the Bell state.

In order to reduce residual distinguishability caused by the two chips not being perfectly similar after fabrication, we have added extra tuning qubits and the possibility to drive the chips via a weakly coupled back-port. The tuning qubits allow for in-situ tuning of the resonator frequencies and the extra drive on the second chip allows us to compensate for differences in resonator loss rates. This drive also allows us to change the parity of the state by driving it with a different shape.

1.3.2 Thesis outline

We will start with explaining the physics behind a transmon qubit coupled to a cavity and in detail how a measurement is performed using input output theory in Chapter 2. We then discuss the experimental methods used to create the entangled states and typical tune up and calibration procedures in Chapter 3. A large part of this thesis was finding out - in an unbiased way - which result we actually had obtained performing our experiment via state tomography. This is therefore explained in Chapter 4. Chapter 5 explains the master equation model used to fit the data obtained from the experiment and the solution to the classical equations of motion needed for the compensation drive in the back-port. Chapter 6 shows the results on what entanglement was achieved and how the measurement process went. This is followed by a summary and conclusion in Chapter 7.

2 Circuit based Cavity Quantum electrodynamics

This chapter will explain the theory to understand the quantum hardware. We will start with an introduction to light matter interaction using an analogy to atoms in a cavity in sec. 2.1 and move on the superconducting circuit used in this experiment in sec. 2.1.1. We then describe the two main components of that circuit: the qubit in sec. 2.2 and the theory of a coplanar waveguide resonator and coherent states in sec 2.3. This is followed by sec. 2.4 describing coupling of the qubit to a resonator which is needed to be able to readout the qubit state via the resonator. Finally we give an introduction to input output theory and show how it can be used to understand the dynamics of a single qubit measurement in sec. 2.5.

2.1 Enhanced light matter interaction

In order to answer the question: "Why do atoms spontaneously emit light?", researches have investigated the effect of the surrounding of an atom on its emission rate [53]. It turns out that atomic emission rates not only change due to interaction with light, but also due to the mode environment surrounding the atom. The discovery that light matter interaction could be enhanced - and therefore better studied - by placing matter inside a cavity gave rise to the field called Cavity Quantum Electrodynamics [79]. The basic schematic for an atom interacting with a light field is shown in Fig. 2.1a. The cavity consists of two straight mirrors driven by a laser field. Due to the finite distance between the mirrors, the electromagnetic field only exists in modes of discrete energy. These single modes can be occupied containing quantized packets of energy also known as photons. The modes interact strongly with the dipole moment of the atom if the

(A)   (B)
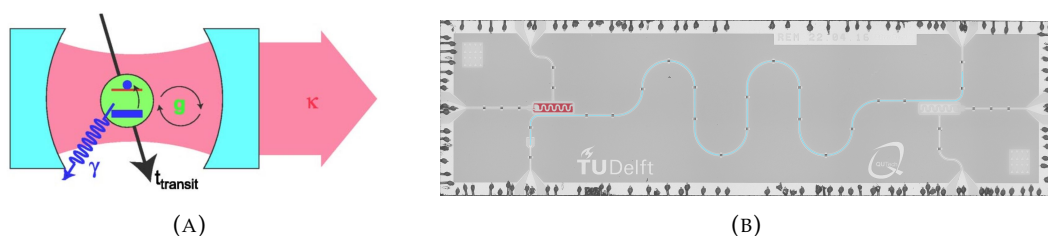
FIGURE 2.1: (A) Atom coupled to a cavity consisting of two mirrors for a finite time $t_{transit}$ as studied in CQED. Important parameters are the cavity decay rate κ the atom cavity coupling g and the atom intrinsic decay rate γ, adopted from [9]. (B) Circuit CQED version used in this experiment where the atom is replaced by a transmon qubit (indicated in red) and the cavity by a resonator(indicated in blue), but the parameters and mathematical description is the same as in (A).

atom is inside the cavity at an anti-node of the field mode [24]. This interaction depends on the qubit state if the transition frequency is far detuned from the cavity resonance frequency and can therefore be used to readout the state of the atom! This was the basic inspiration for the design of dispersive readout based superconducting circuits [9] used in this experiment and shown in Fig. 2.1b.

2.1.1 Superconducting circuits

In our superconducting circuit the cavity is replaced by an LC microwave resonator behaving like an harmonic oscillator. Atoms are also replaced by their artificial circuit versions and used as qubits. Based on the relevant quantum variable used for recreating the atom, e.g charge, phase or flux we can build different types of qubits each with their own advantages and disadvantages. A good review on the different types is given by [19], but in this experiment we use the transmon [50], an alteration of the cooper pair box CPB [58], which can be seen as a simple LC circuit with a small but important alteration. For a harmonic oscillator, the spacing between levels - e.g one, two or more photons in the same mode - has equal energy, meaning that if we drive the harmonic oscillator we will not just drive the $0 \rightarrow 1$ transition, but also the $1 \rightarrow 2$ and $2 \rightarrow 3$ transition etc. In order to be able to isolate the $0 \rightarrow 1$ transition to create a qubit, we need to increase the anharmonicity $\alpha = \omega_{12} - \omega_{01}$. This is done by replacing linear inductors with Josephson junctions [47], which are two slabs of aluminum separated by a few nm thick layer of insulating aluminum oxide. This acts as a non-linear inductor and decreases the higher state transition energies lifting the level spacing degeneracy. Making use of electrical circuits instead of light and atoms introduces another requirement: the system must be superconducting. This is to prevent dissipation of energy via the resistance of the material and the macroscopic coherence arising due to this [4] actually is the main reason we can engineer a single quantum in a macroscopically sized system!
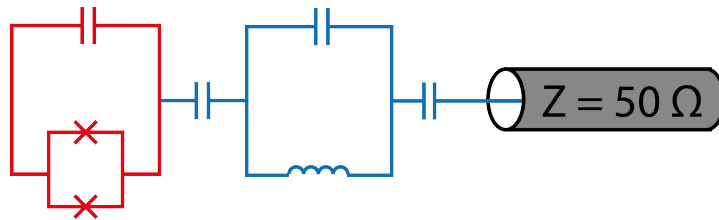
FIGURE 2.2: Circuit diagram of the flux tunable transmon coupled to a resonator and a 50 Ω impedance transmission line. In red, the transmon circuit consisting of two large superconducting islands with two Josephson junctions in a loop allowing flux tunability of the transmon frequency. In blue, the resonator coupled to the transmon as a simple LC oscillator neglecting higher order modes

2.2 Qubit implementation

2.2.1 The Cooper pair Box

The (flux tunable) CPB consists of two superconducting islands separated by two Josephson junctions forming a loop. The Islands are then capacitively coupled to a readout resonator and usually a direct drive line for single qubit operations as shown in Fig. 2.2.

Writing down the classical Hamiltonian from this circuit gives [8]

$$H = 4E_C \left(n - n_g\right)^2 - E_J \cos \phi \tag{2.1}$$

Where $E_c = \frac{e^2}{2C_\Sigma}$ is the charging energy or the energy cost of putting another charge on one of the islands due to the coulomb repulsion, n the amount of tunneled cooper pairs from one of the islands to another, n_g the offset charge of the environment in units of $2e$, E_J the effective flux tunable Josephson energy and ϕ the superconducting phase difference over the islands. We can write the Hamiltonian in a charge basis of units $2e$.

$$H = 4E_c \sum_{j=-N}^{N} |j\rangle \langle j| - E_J \sum_{j=N-1}^{N} \left(|j+1\rangle \langle j| + |j\rangle \langle j+1|\right) \tag{2.2}$$

Where N is number of charge states taken into consideration. As $N \to \infty$ this becomes exact.

2.2.2 Reduction of charge noise: the Transmon

The CPB has a very small superconducting island, therefore its transition energy ω_{01} is very sensitive to fluctuating charges in the substrate known as charge noise, which gives dephasing of the qubit state. A measure of sensitivity is given by the charge dispersion $\epsilon_i = E_i \left(n_g = 0\right) - E_i \left(n_g = \frac{1}{2}\right)$ as a function of the ratio $\frac{E_J}{E_C}$ as can be seen in Figure 2.3. Environmental offset charges will change n_g and - if $\frac{E_J}{E_C}$ is small - cause significant changes in ω_{01} giving dephasing of the qubit. The transmon qubit now reduces this sensitivity by increasing the size, and thus capacitance, of the islands going to a regime of $\frac{E_J}{E_C} \gg 1$. The downside of an increased $\frac{E_C}{E_J}$ ratio is a reduction of α, but this only goes algebraically with $\frac{E_J}{E_C}$ while the charge dispersion decreases exponentially [50].
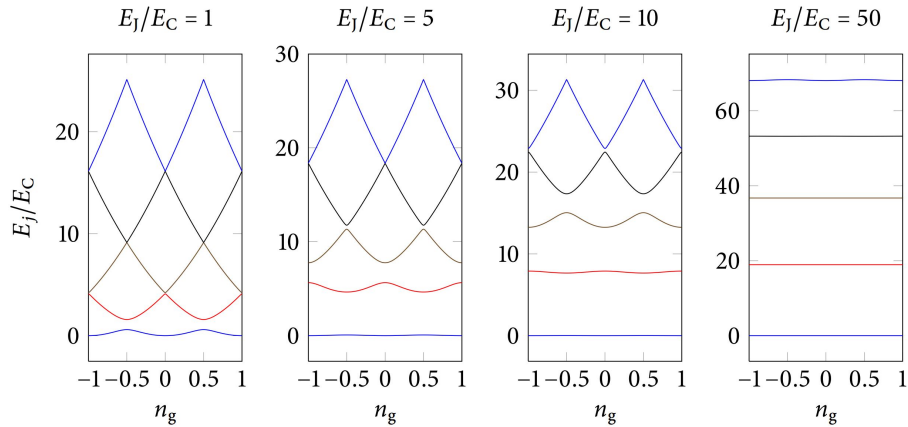
FIGURE 2.3: Sensitivity to environmental offset charges showing four energy levels E_i as a function of n_g. The charge dispersion decreases exponentially as a function of E_J/E_C, while the anharmonicity α only decreases algebraically. Figure adopted from [8].

2.2.3 Transmon eigenstates

The transmon is in the regime of $E_J/E_C \approx 50$. This means that seeing it as a charge state where the excited state differs from the unexcited by the tunneling of a cooper pair
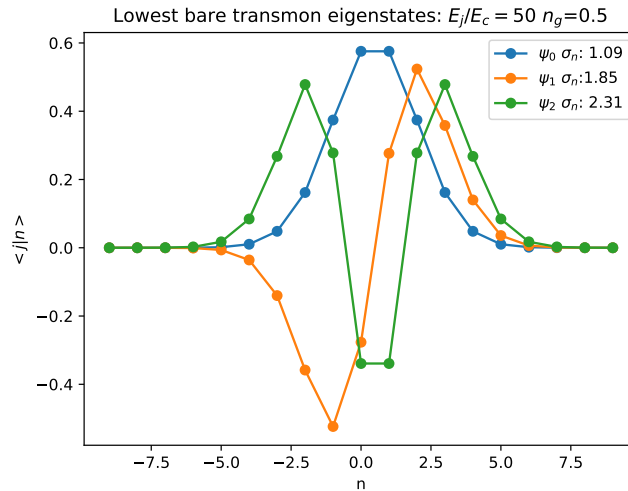
FIGURE 2.4: The three lowest bare eigenstates of the Transmon Hamiltonian 2.2 for typical experimental parameters $E_J/E_C = 50$, $\frac{E_C}{h} = 270MHz$ and $n_g = 0.5$. The fluctuations in cooper pair numbers $\langle \hat{n}^2 \rangle - \langle \hat{n} \rangle^2$ are given in the legend, showing that even the second excited state only fluctuates to about 2 cooper pairs, making the amount of tunneled cooper pairs still a reasonably valid quantum number. Figure simulated using Qutip [46].

is not completely valid. The superconducting phase difference $|\theta\rangle = \sum_{N=-\infty}^{\infty} e^{i\theta N} |N\rangle$ between the two islands, which is the conjugate of the charge state, will now also have a more well defined value. The best way to get intuition about these things is just to diagonalize the Hamiltonian from Eq. 2.2. This results in the first 3 ground states shown in Figure 2.4. Here we see an average fluctuation in tunneled cooper pairs of $\langle \hat{n}^2 \rangle - \langle \hat{n} \rangle^2 < 2$ for the ground and excited state.

Another useful property we obtain from the diagonalization are the transmon eigenenergies and therefore the transition frequencies between qubit states. By setting E_C via the capacitances of the islands we can roughly tune the ratio of E_J/E_C and these frequencies. They are typically in the low GHz regimes (5-20GHz) and should be larger than the thermal frequencies of $\approx$ 20mK found in dilution refrigerators: $\hbar\omega_{01} > k_b T_{dilution}$ [22]. Writing the Hamiltonian in the basis of transmon eigenstates $|j\rangle$, it will be diagonal

$$H_q = \hbar \sum_j \omega_j |j\rangle \langle j| \approx -\frac{1}{2}\hbar\omega_{01}\sigma_z \qquad (2.3)$$

where the right equation comes from assuming a perfect two level system and setting the ground state energy to be $-\frac{1}{2}\hbar\omega_{01}$.

2.2.4 Frequency tunability

For further post-fabrication fine tuning of the qubit frequencies, the transmon can have two Josephson junctions setup parallel in a loop forming a Superconducting quantum interference device(SQUID). If there is an external magnetic flux Φ_{ext} in units of the flux quantum $\frac{\hbar}{2e}$ present, the total Hamiltonian H_J expressed in phase differences over the two junctions is given by

$$H_J = -E_{J1} \cos \varphi_1 - E_{J2} \cos \varphi_2 \qquad (2.4)$$

Where the Josephson energies E_J depend on the thickness and transmission of the junction, and the phases satisfy due to the loop $\varphi_1 = \Phi_{ext} - \varphi_2$. This can be rewritten in the form

$$H_J = -E_J \cos \varphi = -E_{J\Sigma} \cos \left(\frac{1}{2}\Phi_{ext} \right) \sqrt{1 + d^2 \tan^2 \left(\frac{1}{2}\Phi_{ext} \right)} \cos \varphi \qquad (2.5)$$

where we introduced the asymmetry between the junctions $d = \frac{E_{J2}-E_{J1}}{E_{J\Sigma}}$, $E_{J\Sigma} = E_{J1} + E_{J2}$ and the new "phase" degree of freedom $\varphi = (\varphi_1 + \varphi_2)/2 - \arctan d \tan \left(\frac{1}{2}\Phi_{ext} \right)$ [78]. The SQUID essentially behaves like a single junction with an effective Josephson energy E_J as shown in Figure 2.4, where E_j is set by the asymmetry and the external flux which is used in Eq. 2.2. It allows tuning of E_J and therefore the qubit transition frequency.

2.3 The field inside the resonator

This section will describe the quantization of the electromagnetic field in a cavity, because that is the second main component in CQED and indicated in blue in our chip picture in Fig. 2.1b. Maxwell's equations, governing the mathematical relationship between magnetic and electric fields can be solved in a confined space without a source term for a vector potential A that relates to the electric field E and the magnetic field B via

$$\begin{aligned} \vec{B} &= \nabla \times A \\ \vec{E} &= -\frac{\partial A}{\partial t} \end{aligned} \qquad (2.6)$$

The solutions for A depend on the boundary conditions, but if we solve this in free space we obtain as solutions a set of orthonormal mode functions [79]

$$A(\vec{r}, t) = \sum_k \left(\frac{\hbar}{2\omega_k \epsilon_0} \right)^{1/2} \left[a_k u_k(\vec{r}) e^{-i\omega_k t} + a_k^\dagger u_k^*(\vec{r}) e^{i\omega_k t} \right] \qquad (2.7)$$

where $\vec{r}$ is the position coordinate, t is time, ω_k is the frequency for mode k, a_k the dimensionless Fourier component of mode k and u_k is the mode function - e.g a plane wave - which specific form depends on the boundary conditions and k is the mode index denoting different possible frequencies and polarizations.

Now in order to make calculations of the dynamics easier and satisfy the quantization of energy, we use a trick called *second quantization*. Since the geometry fixes the u_k we can basically describe all of the system dynamics independent of the specific geometry by looking at the dynamics of a_k alone. We replace these a_k with creation $\hat{a_k}$ and annihilation $\hat{a_k}^\dagger$ operators representing the creation and annihilation of the minimum single energy quantum (or photon) in the field mode k and they should satisfy the following commutation relations

$$[\hat{a}_k, \hat{a}_{k'}] = \left[\hat{a}_k^\dagger, \hat{a}_{k'}^\dagger \right] = 0, \left[\hat{a}_k, \hat{a}_{k'}^\dagger \right] = \delta_{kk'} \qquad (2.8)$$

where the commutator $[a, b] = ab - ba$. These are called the *bosonic commutation relations* for the fact that we can have an infinite amount of photons in each mode. The system
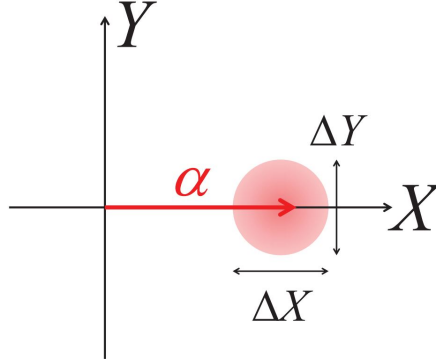
FIGURE 2.5: Coherent state $|\alpha\rangle$ with vacuum fluctuations in the conjugate variables $\langle X \rangle$ and $\langle Y \rangle$. Figure adopted from [36].

dynamics are then fully governed by the following simple looking Hamiltonian

$$H = \hbar \sum_q \left(\omega_q \hat{a}_q^\dagger \hat{a}_q + \frac{1}{2} \right) \tag{2.9}$$

where the total number of photons inside a mode is described by the number operator $\hat{n} = \hat{a}^\dagger \hat{a}$ and usually $\hbar$ is taken to be 1 for convenience. Even though we have now described the dynamics of the system operators we still need to give the states on which these operators act. The most common choice of basis are the *Fock states* $|n_0, n_1, ...\rangle$ representing the amount of photons in each mode.

The resonator indicated in Fig. 2.1b is a half-wave coplanar waveguide resonator, which basically is a long superconducting strip capacitively coupled to ground via a gap around it. Half-wave means that the length of the resonator is half the wavelength of the fundamental mode. The spacing between the other modes is much larger than the energy range of interest, therefore in modeling we retain only a single mode and we can drop the mode index k and arrive at the more simple Hamiltonian

$$H = \hbar \left(\omega_c \hat{a}^\dagger \hat{a} + \frac{1}{2} \right) \tag{2.10}$$

where ω_c is the fundamental mode frequency of the resonator and we can describe a resonator state by $|n\rangle$ where n denotes the amount of photons in this mode.

2.3.1 Coherent states

It is worthwhile to mention one more choice of basis: the coherent states, because they arise if one drives a cavity with a coherent - meaning stable and definite phase - microwave tone or in the optical case from the field generated from a highly stable laser above threshold. The coherent state is an infinite superposition of Fock states and represents a state of more definite phase.

$$|\alpha\rangle = e^{-|\alpha|^2/2} \sum_n \frac{\alpha^n}{(n!)^{1/2}} |n\rangle \tag{2.11}$$

Coherent states are the displaced vacuum state $D(\alpha)\left|0\right\rangle$, with the unitary

$$D(\alpha) = e^{\alpha\hat{a} - \alpha^*\hat{a}^\dagger} \tag{2.12}$$

and α a complex number representing the average amount of photons in that state, e.g $|\alpha|^2 = \langle\hat{n}\rangle$. This also happens to be the eigenstate of the annihilation operator $\hat{a}$. In experiments, we measure the classical real and imaginary parts of α, I and Q called quadratures since they correspond to the in and out of quadrature signals of typical heterodyne electric field measurements. In any quantum optical textbook their quantum mechanical analog is described by hermitian operators $\hat{X}, \hat{Y}$ [36]

$$\hat{X} = \frac{1}{2}\left(\hat{a} + \hat{a}^\dagger\right), \qquad \hat{Y} = -\frac{i}{2}\left(\hat{a} - \hat{a}^\dagger\right) \tag{2.13}$$

These obey the canonical commutation relation $\left[\hat{X}, \hat{Y}\right] = \frac{i}{2}$ showing that they cannot be measured simultaneously with arbitrary precision. The uncertainty principle then gives $\Delta\hat{X}\Delta\hat{Y} \leq 1$ and coherent states are precisely the minimum uncertainty states for which $\Delta\hat{X} = \Delta\hat{Y} = 1$. A nice illustration of coherent states and the vacuum fluctuations induced by the above uncertainties is given by Figure 2.5

2.4 Resonator qubit coupling

A widely used model for both the atom-cavity dynamics from Figure 2.1a and the superconducting Transmon qubit coupled to a readout resonator of Fig. 2.1b is given by the first order dipole coupling *Rabi Hamiltonian*

$$H = \hbar\left(\omega_c + \frac{1}{2}\right)a^\dagger a + \frac{1}{2}\hbar\omega_q\sigma_z + g(\sigma_+ + \sigma_-)(a^\dagger + a) \tag{2.14}$$

where the first two terms are just the uncoupled Hamiltonians of the two level system from Eq. 2.3 and the single mode oscillator of Eq. 2.9. The last term effectively represents swapping of excitations between the qubit and resonator via the interaction of the EM field with the dipole of the transmon due to tunneling of the cooper pairs across the island and σ_- and σ_- represent the lowering and raising operators of the qubit. Here g is the coupling strength depending on calculating the first order matrix elements between the charge operator $\hat{n}$ and the transmon eigenstates with a prefactor given by the device geometry [50]. It is customary to throw away terms corresponding to excitations in both the qubit *and* the resonator, e.g the $a^\dagger\sigma^+$ and $a\sigma^-$ terms. This is called the Rotating wave approximation (RWA) since it can also be seen as the averaging out of fast rotating terms in the frame rotating at the frequency of the resonator. The resulting Hamiltonian is called the *Jaynes Cummings Hamiltonian* [45].

Now if we denote the detuning of a qubit with the resonator by $\Delta = \omega_q - \omega_c$ and if this detuning is large compared to the coupling g, we can approximate H_{JC} by doing a unitary transformation [50] and expanding it in the small parameters $\lambda = g^2/\Delta_i << 1$. This is called the dispersive approximation and gives the resulting Hamiltonian

$$H = \frac{\omega_q'}{2}\sigma_z + \left(\omega_c' + \chi\sigma_z\right)a^\dagger a \tag{2.15}$$

where if we take the higher transmon levels into account before the approximation we get the renormalized frequencies $w'_q = w_q + \chi_{01}$, $w'_c = w_c - \frac{\chi_{12}}{2}$, $\chi = \chi_{01} - \frac{\chi_{12}}{2}$,$\chi_{ij} = \frac{g_{ij}^2}{\omega_{q_{ij}} - \omega_c}$ and $\omega_{q_{ij}}$ are the transition frequencies from state i to state j given by diagonalizing Eq. 2.2 and the perturbative dipole coupling strength $g_{j,j+1}$ is given by $\langle j | \hat{n} | j+1 \rangle$ where $\hat{n}$ is the charge number operator.
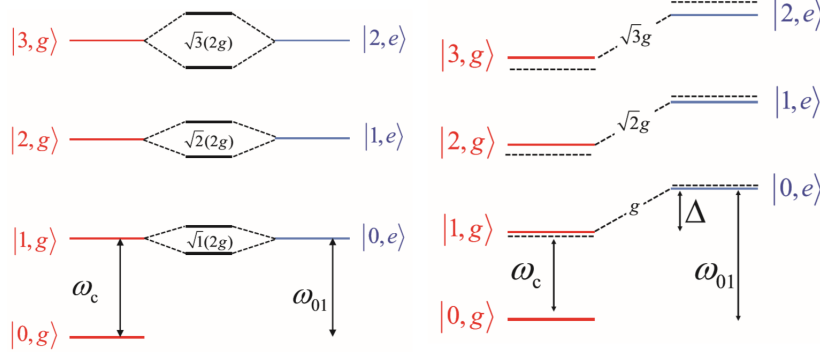
FIGURE 2.6: Energy level diagram showing the effect of coupling the qubit and resonator via the Jaynes Cummings model. The left diagram shows a hybridization of qubit and resonator in case of equal frequencies. The right diagram shows the renormalization of the qubit and resonator frequencies if they are far detuned from each other. Numbers indicate photon occupations and g, e the ground and excited state of the qubit respectively. Figure adopted from [36].

In our experiment we have two qubits coupled to a resonator, but this equation can be interpreted for each qubit separately given they are not close to each other or the resonator in frequency. For a single qubit this equation says that the resonator and qubit push each other away from their bare frequencies due to the coupling. This is given by the χ_{ij} and is called the Lamb shift. In the experiment we use precisely this effect for tuning the resonator by changing the qubit frequency. The other effect we can see from this is the AC Stark shift χ which depends on the qubit and resonator states. For each excitation(photon) in the resonator the qubit frequency is shifted by χ. This also holds the other way around: if the qubit is in the excited state, the resonator is shifted by 2χ. Therefore this can be used to readout the qubit state by probing the resonator with a fixed frequency and looking at the resulting change in phase or amplitude of the output due to the change in resonance frequency.

Introducing a microwave drive

The system can be driven with a microwave field at frequency ω_d through a feed line that is capacitively coupled to the resonator. This introduces a driving term

$$H_d = \hbar\epsilon(t) \left(\hat{a}^\dagger e^{-i\omega_d t} + \hat{a} e^{i\omega_d t} \right) \tag{2.16}$$

where $\epsilon(t)$ is a measure of the drive amplitude [9]. The total system Hamiltonian then becomes $H_{JC} + H_D$ and if the frequency of the driving tone is in resonance with the qubit we can perform logical gates on the qubits [10], while if the driving tone is far detuned from the qubit and close to the resonator frequency we can perform continuous weak QND measurements via monitoring the qubit state dependent output field. This is an integral part of this thesis and will be discussed more thoroughly in the next section.

2.5 Qubit readout

2.5.1 Input output theory

In the previous section we have introduced a *external* driving term in the Hamiltonian, but the modeling of physical systems via Hamiltonians can only describe closed systems. The classical thermodynamics picture of a system A interacting with and dissipation to a heat bath B can therefore only be described by a full Hamiltonian of A, B and their interaction. This section will answer the question of how to model the drive via the input line to our chip in a classical way, introducing causality via an input and a system output depending on the input following. This is beautifully derived in [35] and explained in [73, 79]. We will present a short version below, because the result is widely used throughout this thesis.

2.5.2 Coupling to continuous systems

A key assumption in any quantum mechanical dissipation is the continuity of the bath. Take a transmission line for example, we can quantize the electric field in the same way as we did in Eq. 2.9. But now - as opposed to the resonator where only a single mode was important - the length of the line is assumed to be infinite. Therefore the mode spacing goes to zero, which allows us to write the transmission line Hamiltonian H_B as

$$H_B = \hbar \int_{-\infty}^{\infty} \omega \hat{b}^{\dagger}(\omega)\,\hat{b}(\omega) \tag{2.17}$$

where again the bosonic creation and annihilation operators satisfy $\left[b(\omega), b^{\dagger}(\omega)\right] = \delta(\omega)$. If we then couple this bath to a single mode cavity assuming linear system bath interaction we obtain a similar interaction term as in Eq.2.14

$$H_{int} = i\hbar \int_{-\infty}^{\infty} \kappa(\omega) \left(\hat{b}^{\dagger}(\omega)\,\hat{a} - \hat{a}^{\dagger}\hat{b}(\omega)\right) \tag{2.18}$$

where a is the cavity annihilation operator, $\kappa(\omega)$ the frequency dependent coupling strength and where the integral should range from $(0, \omega)$, but usually we are in a rotating frame and $\kappa(\omega)$ is assumed to be zero for all ω except a small bandwidth around the rotating frame - called the *Markov approximation* - so we can safely extend the limits of the integral to ∞.

We can now calculate the Heisenberg equations of motion for an arbitrary system with a cavity coupled as above

$$\dot{c}(t) = -\frac{i}{\hbar} \left([c(t), H_{sys}] + [c(t), H_B] + [c(t), H_{int}]\right) \tag{2.19}$$

for any operator c including $b(\omega)$. We can immediately solve the resulting differential equation for $b(\omega)$ giving $b(\omega, t)$ (now changing in time) as a function of $c(t)$.

$$b(\omega) = e^{-i\omega(t-t_0)}b_0(\omega) + \kappa(\omega) \int_{t_0}^{t} e^{-i\omega\left(t-t'\right)}c(t')\,dt' \tag{2.20}$$

where the initial value $b_0(\omega)$ is $b(\omega)$ at $t = 0$. This can be substituted in Eq. 2.18 together with the assumption that $\kappa(\omega) = \sqrt{\frac{\kappa}{2\pi}}$ resulting in the final *Quantum Langevin equation*

for any system operator c

$$\dot{c} = -\frac{i}{\hbar}[c, H_{sys}] + \left([c, a^\dagger]\left(\frac{\kappa}{2}a + \sqrt{\kappa}a_{in}(t)\right) - \left(\frac{\kappa}{2}a + \sqrt{\kappa}a_{in}(t)\right)[c^\dagger, a]\right) \qquad (2.21)$$

where the input field $a_{in}(t)$ is defined as

$$a_{in}(t) = \sqrt{\frac{1}{2\pi}}\int d\omega e^{-i\omega(t-t_0)}b_0(\omega) \qquad (2.22)$$

which can be seen as a white noise input since the commutation relation $\left[a_{in}(t), a_{in}^\dagger(t')\right] = \delta(t - t')$ giving a flat spectrum. We now have the equation of motion for any system operator c, but we need to do one more step in order to get the output of the system as a relation of the input. This involves solving Eq. 2.19 for $b(\omega)$ not just for previous times t_0, but for a future time $t_1 > t$. If we then perform the same steps as above, we get the *Time reversed Langevin equation* similar to Eq. 2.21 back but with a_{in} replaced by an output field defined as

$$a_{out}(t) = \sqrt{\frac{1}{2\pi}}\int d\omega e^{-i\omega(t-t_0)}b_1(\omega) \qquad (2.23)$$

Now since both Langevin equations describe the time evolution of the same operator, we can equate them to obtain the famous *input output relation*

$$a_{out}(t) + a_{in}(t) = \sqrt{\kappa}a(t) \qquad (2.24)$$

this equation thus gives meaning to causality in quantum systems and allows us to easily calculate the system output given an arbitrary input!
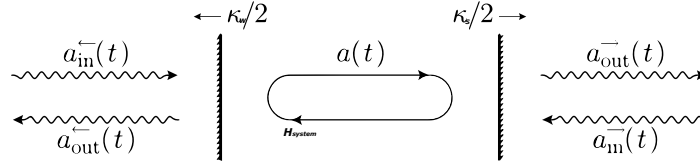
FIGURE 2.7: Illustration of a single cavity with a qubit described by H_{sys} with cavity annihilation operator $a(t)$ in the Heisenberg picture coupled to an infinitely long transmission line through a weak coupling κ_w on one side and a strong coupling κ_s on the other, adapted figure from [73]

2.5.3 Dispersive readout of a single cavity

We can illustrate the use of the formalism above by describing the measurement of a qubit via driving a transmission line coupled to a readout resonator - or asymmetric Fabri-Perot cavity - with strong coupling κ_s, see Figure 2.7. There is a transmission line coupled to other side of the resonator with a weak coupling κ_w allowing us to choose between readout in reflection or transmission. The system Hamiltonian is taken to be that of Eq. 2.15, together with the added driving term of Eq. 2.16. Solving Eq. 2.21 for the cavity field operator a in a frame rotating at the drive frequency ω_d gives

$$\frac{\partial a}{\partial t} = -\left(i\left(\Delta + \chi \sigma_z \right) + \frac{\kappa_w + \kappa_s}{2} \right) a + \sqrt{\kappa_s}\left(a_{in}^s + \epsilon^s\left(t \right) \right) \tag{2.25}$$

where $\Delta = \omega_c - \omega_d$, $\epsilon^s\left(t \right)$ the time dependent coherent drive (if we take ϵ from Eq. 2.16 we renormalize with $\epsilon^s = \frac{-i\epsilon}{\sqrt{\kappa_s}}$) at the strong input port and χ the dispersive shift. We have assumed no drive in the weak port and neglected the bath noise from the bath, which is valid if $\kappa_w << \kappa_s$. The correspondence with the classical Langevin equation is now clear if we see a_{in} as a white noise term. Note that we could replace $a_{in}\left(t \right) \rightarrow a_{in}\left(t \right) + \epsilon^s\left(t \right)$ since the drive can be seen as a coherent state with white noise from the boson bath superposed on it.

Taking the expectation value of Eq. 2.25 on both sides and taking the qubit state as classical up or down then gives the qubit state dependent classical equation of motion for the complex field amplitude α in the rotating frame of the drive.

$$\dot{\alpha}^{\pm} = -\left(i\left(\Delta \pm \chi \right) + \frac{\kappa_w + \kappa_s}{2} \right) \alpha + \sqrt{\kappa_s}\epsilon^s\left(t \right) \tag{2.26}$$

where $|\alpha|^2 = \langle n \rangle$ the average photon number inside the cavity at a time and ϵ^s can be seen as the coherent driving field such that $|\epsilon^s|^2$ has units of power going in the cavity. The different normalization comes from the fact that the cavity is defined in a bounded region, while the input field is defined in an unbounded region. We can solve Eq. 2.26 in steady state by setting the left hand side to zero and assuming a constant driving field ϵ_{ss}^s

$$\alpha_{ss} = \frac{\sqrt{\kappa_s}}{i\left(\Delta \pm \chi \right) + \frac{\kappa_w + \kappa_s}{2}}\epsilon_{ss}^s \tag{2.27}$$

The classical output field in reflection, denoted by $z\left(t \right)$, is then given via Eq. 2.24

$$z^{\pm}\left(t \right) = \sqrt{\kappa_s}\alpha^{\pm}\left(t \right) - \epsilon^s\left(t \right) \tag{2.28}$$

Thus in steady state we get $z_{ss} = r^{\pm}\epsilon_{ss}^s$, with $r^{\pm} = \frac{-\left(\kappa_s + \kappa_w \right) + 2i\left(\Delta \pm \chi \right)}{\left(\kappa_s + \kappa_w \right) + 2i\left(\Delta \pm \chi \right)}$, so we can see this as a qubit state dependent phase shift.

We can solve Eq. 2.26 easily by going to the Fourier domain obtaining for the cavity and output field

$$\alpha\left(\omega \right) = H_a^{\pm}\left(\omega \right)\epsilon^s\left(\omega \right), \qquad z\left(\omega \right) = H_{a^R}^{\pm}\left(\omega \right)\epsilon^s\left(\omega \right) \tag{2.29}$$

where we can see H_a as a transfer function of the qubit cavity system and H_{a^R} is the transfer function for the reflected output field, the precise form is given in Eq. 5.4. We could also look into the transmitted output field which is simply $\sqrt{\kappa_w}H_a$ since there is no input assumed from the weak port. We can now finally understand a dispersive measurement illustrated in Figure 2.7. Information about the qubit state entangles with the cavity photons and we can thus project the qubits by measuring the outgoing photons!

The master equation

Another approach to system bath coupling is the master equation for the combined system density matrix. We can basically eliminate the bath degrees of freedom by tracing out the bath and assuming the bath is not affected by our system. For our system with a single qubit and cavity this then gives a Lindblad type master equation of the form [31,
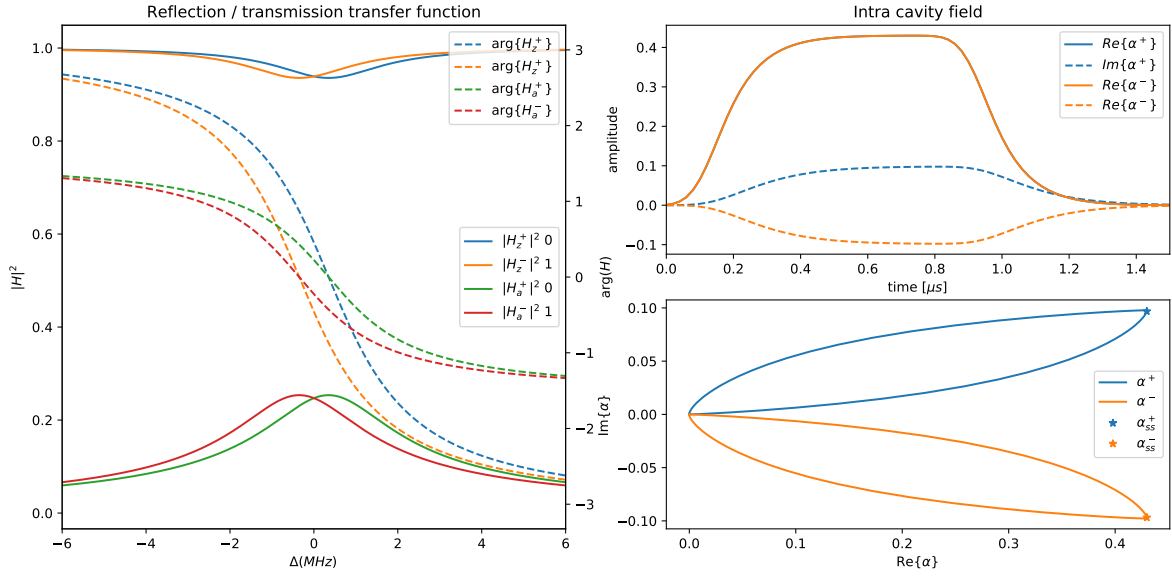
FIGURE 2.8: Dispersive readout scheme. (A) Transfer function for a measurement in reflection and for a measurement in transmission. At $\Delta = 0$ all information is carried in the phase difference of the output signal. Note that in the case of a transmission measurement the phase difference is half of the difference in case of reflection for the same amplitude. Giving a higher measurement efficiency for reflection. (B) Example cavity transients showing a qubit state dependent phase and convergence to the steady state after $\frac{2\pi}{\kappa} \approx 300$ns (C) Example phase space trajectory, with the steady state given by a star. All simulations were done with $\frac{\chi}{2\pi} = 0.33$MHz, $\frac{\kappa_s}{2\pi} = 3.01$MHz and the drive was a smoothed square pulse of $1\mu s$.

32]

$$\frac{\partial \rho}{\partial t} = \frac{i}{\hbar} \left[H_{JC}, \rho \right] + \kappa D\left[a\right]\rho + \gamma D\left[\sigma_-\right] + \gamma_\phi D\left[\sigma_z\right] \tag{2.30}$$

which is basically the von Neumann equation for the (dispersive) Jaynes Cummings Hamiltonian of Eq. 2.15 together with Lindblad operators [80] $D\left[A\right] = A\rho A^\dagger - \frac{1}{2}\left(A^\dagger A\rho + \rho A^\dagger A\right)$ representing non-unitary evolution, which is in this case is decay where κ is the rate of decay of the cavity into the environment(or transmission line in this case) and γ, γ_ϕ represent energy loss and pure dephasing of the qubit to the environment respectively.

Measurement induced dephasing and the polaron transformation

To obtain insight into how photons in the cavity affect the qubit state, we can make use of the fact that the cavity, if initially in a coherent state and driven by a coherent state, will always remain in a coherent state. Note that we can simulate the evolution of the coherent state average from Eq. 2.26. We can make use of this knowledge by hybridizing the qubit and cavity degree of freedom via $\rho^P = U^\dagger \rho U$ with $U = P_0 \mathcal{D}\left(\alpha_+\right) + P_1 \mathcal{D}\left(\alpha_-\right)$ where $\mathcal{D}$ is the cavity displacement operator as defined in Eq. 2.12. As opposed to the normal frame of reference(lab frame), in the polaron frame the cavity is always in the vacuum state. This removes the entanglement between the "qubit" and resonator and thus all terms involving a will become zero. This greatly simplifies the master equation, keeping only the qubit terms and then transforming back to the lab frame as derived in

Appendix A of [31] we end up with

$$\dot{\rho}(t) = \frac{i}{\hbar} \left[H_q'(t), \rho(t) \right] + \gamma D \left[\sigma_- \right] \rho(t) + \frac{1}{2} \left[\gamma_\phi + \Gamma_d(t) \right] D \left[\sigma_z \right] \rho(t) \qquad (2.31)$$

where we took the trace over the resonator $\rho(t) = \text{Tr}_{cav}(\rho)$ and ended up with a qubit-only Hamiltonian. The qubit now has a cavity state dependent frequency due to the AC Stark shift from the interaction with the cavity

$$H_q'(t) = \frac{1}{2} \left(\omega_q + \chi + 2\chi \text{Re} \left\{ \alpha^+(t) \alpha^{*-}(t) \right\} \right) \sigma_z \qquad (2.32)$$

and an extra cavity state dependent dephasing term given by

$$\Gamma_d(t) = 2\chi \text{Im} \left\{ \alpha^+(t) \alpha^{*-}(t) \right\} \qquad (2.33)$$

which is called the *measurement induced dephasing*, because this dephasing comes purely from photons in the cavity entangling with the qubit and leaking out afterwards. This can be seen as a quantitative expression for the projection speed of the measurement if we monitor the output field and we can thus truly speak of a continuous weak measurement of σ_z! Note that if the output fields for both qubit states were the same, the measurement cannot distinguish the two states and therefore we would not project the qubit. We make use of this in 5.2.1 when we start cascading systems and want to make only the odd-parity subspace indistinguishable.

3 Setup and methods

This chapter will describe our setup and then continue with the various calibration procedures. Finally it will give our estimated parameters.
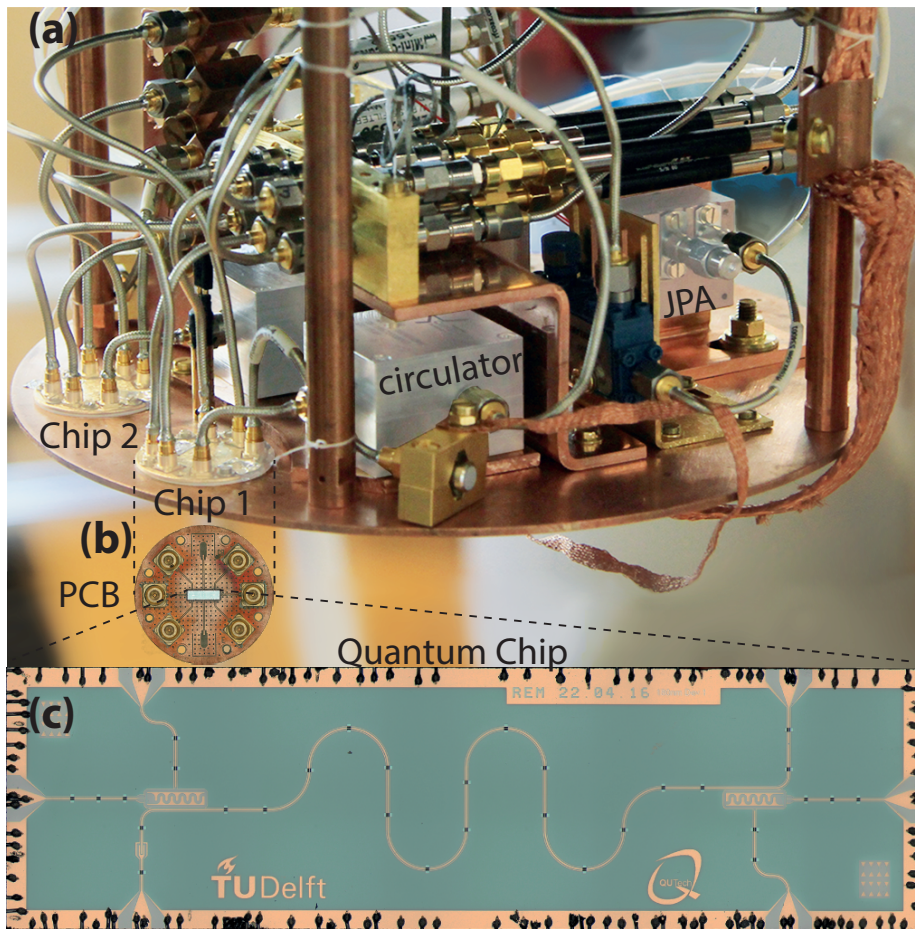
FIGURE 3.1: Picture of the experimental setup. (A) The bottom of the dilution-refrigerator containing the two chips. This stage is attached via thick copper rods to the mixing chamber of the fridge, cooling it to 30mK. Indicated are the microwave circulators and the Josephson Parametric Amplifier(JPA). (B) Top-down view of the chip Printed Circuit Board(PCB). Note that the six SMP connectors take up most of the space. (C) Zoom in of the quantum chip containing 2 qubits coupled to a resonator.

The experiment was performed with two nearly identical chips. They were cooled down to milliKelvin temperatures in a Leiden-Cryogenics CF-650 dilution refrigerator. A photograph of the cold finger of this dilution refrigerator is shown in Fig. 3.1. Each chip contains two qubits coupled to a single resonator and another two used solely to tune the resonator frequencies to optimize entanglement generation. A detailed wiring diagram of the setup is shown in Fig. 3.2
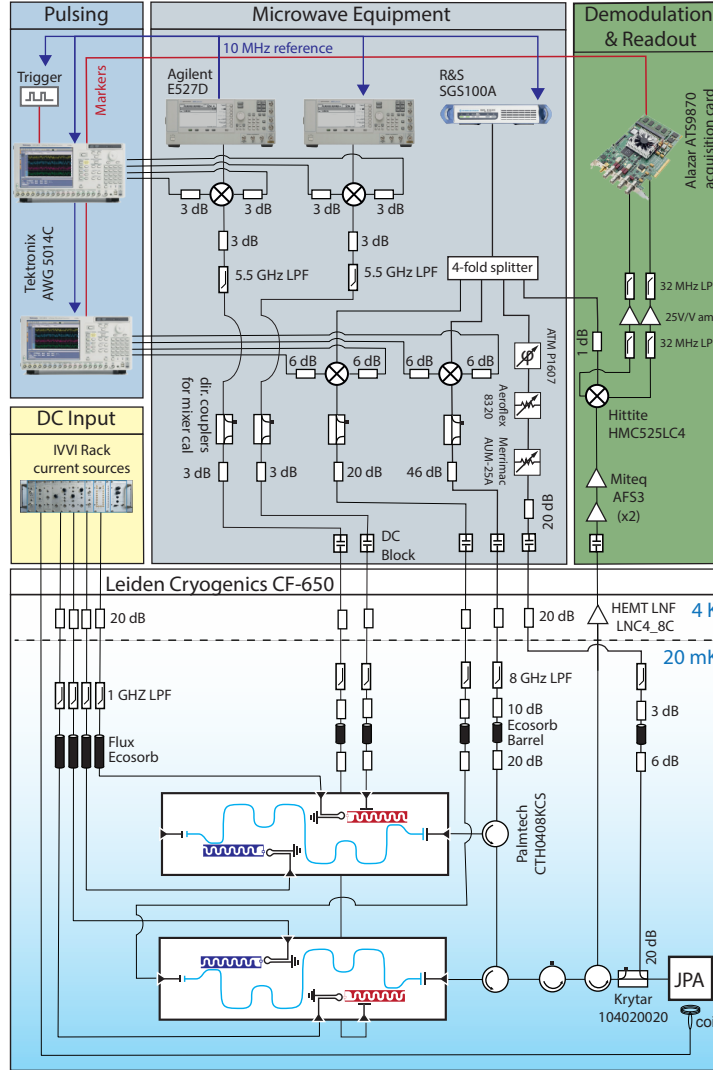
FIGURE 3.2: Detailed wiring diagram of the experiment.

3.1 Tune up and parameter estimation

For generating the half-parity measurement is it very important that we know and are able to manipulate our experimental parameters. In this section we will discuss the various measurements needed to find the qubit and resonator parameters.

3.1.1 Finding the resonator frequency

The first thing to do is a power sweep to find the resonator bare frequency ω_c. Which in the start of an experiment is also the first sign of live of a newly fabricated qubit. In this measurement we do a 2D sweep the power of the continuous microwave source versus driving frequency ω_d. We did a measurement from the weakly coupled back-port so if $\omega_d = \omega_c$ we will see a peak in the output amplitude since we are measuring in transmission. In our case there are 2 qubits coupled to the resonators on each chip, so the bare cavity frequency is shifted via the lamb shifts induced by both qubits at low powers. At intermediate powers the cavity response becomes non-linear due to hybridization with the qubits and at very high powers the cavity becomes effectively insensitive to the qubits and we can measure the bare cavity frequency ω_c [66]. The

results are shown Fig. 3.3. Note that the we used the tuning qubits to tune the second resonator away when measuring the first so it wouldn't show up in the scan.
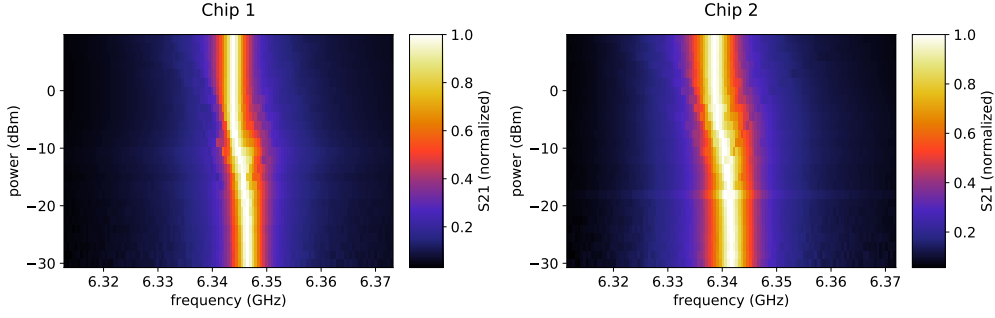
FIGURE 3.3: Resonator power-sweeps on both chips showing the presence of the qubits and the bare resonator frequency. This resulted in an estimate for the bare resonator frequencies $f_{resA} = 6.339$ GHz and $f_{resB} = 6.344$ GHz. From this we can also obtain the resonator line-widths $\frac{\kappa_a^s}{2\pi} = 3.01$ MHz and $\frac{\kappa_b^s}{2\pi} = 4.54$ MHz, but more data was taken on them during the sweep of Fig. 3.6.

3.1.2 Tuning qubit frequencies via Flux bias line
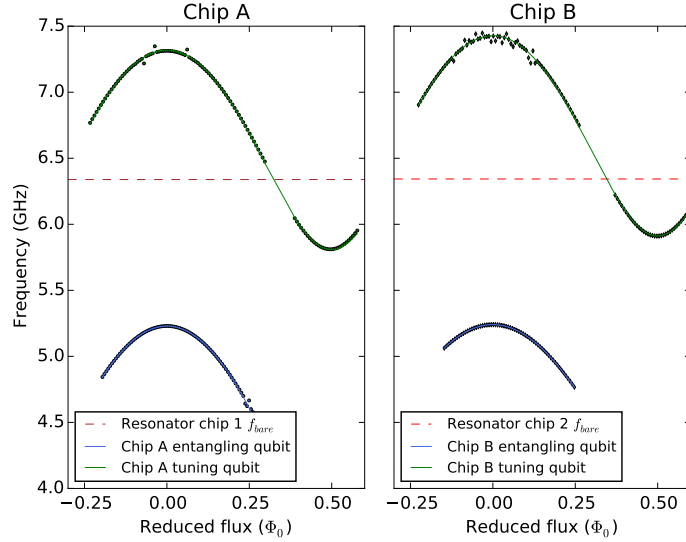
FIGURE 3.4: Entangling(tuning) qubit DAC arches in green(blue) for both chips plotting qubit resonance frequency versus applied flux in units of the flux-quantum. Diamonds represent chip 2 and circles chip 1. Dashed lines represent the resonator bare frequencies. Tuning qubits were fabricated to have a lower and an upper sweet spot within the available DAC range. Entanglement qubits are located below the resonator. The entanglement qubits have sweet-spots - the first-order flux insensitive maxima - at 5.23 and 5.24 GHz. The tuning qubit on chip 1(2) has its top sweet-spot at X(Y) GHz and its lower sweet-spot at X(Y), such that they could be used to compensate the resonator in both directions if necessary.

After the resonators are found, finding the qubits is a logical next step. All of our qubits had a flux bias line, so we could tune each of them by applying a DC current to their respective line. This current generates a magnetic flux which according to Eq. 2.5 alters E_j while keeping E_c constant. This then changes the qubit frequency. In order to measure the qubit frequency at a certain current value, we performed two-tone

spectroscopy. The first tone was send in resonant with the resonator. We then apply a second tone the qubit drive line. If this tone is resonant with the qubit frequency, it will induce a Rabi-oscillation. This will on average increase the excited population of the qubit depending on the detuning of the drive with the resonance frequency saturated at 0.5. The excited population induces a phase and amplitude response in the qubit state dependent resonator transfer function, see Fig. 2.8. Monitoring the transmission versus driving frequency thus shows a change in amplitude or phase depending on the detuning between the resonator and the measurement tone, which indicates being resonant with the qubit. Note that the linewidth of the qubit is normally defined by the qubit dephasing rate $2\pi\gamma_\phi$, so that as the qubit quality increases the ability to accurately measure its frequency would decrease. This effect can be countered by driving the qubit stronger (power broadening), increasing the chance for the qubit to be in the excited state at a given detuning, effectively increasing the line-width. In Fig. 3.4 we show the flux tuneability range of the four qubits used in this experiment.

One problem in tuning up these flux lines is cross-coupling between the lines. If you bias one of the lines you can see that the second qubit frequency is affected. We had a vector $\vec{\phi}$ of five fluxes(4 qubits on 2 chips and the JPA, although the JPA was quite far away in the fridge so shouldn't be affected too much). Now if we denote the effective flux on the qubits and JPA by Φ we can see that

$$\vec{\Phi} = M\vec{\phi} - \vec{\phi}_0 \tag{3.1}$$

where $\vec{\phi}$ is the flux set by the currents, M should be proportional to the identity in the ideal decoupled case. $M_{ij} = \frac{df_{\Phi_j}}{d\phi_i}$ for each qubit. We can correct for this coupling by defining a new flux vector $\vec{\phi}_c = M^{-1}\left(\vec{\phi} - \vec{\phi}_0\right)$ such that we are now able to change the effective flux on each qubit independently given we know the offset $\vec{\phi}_0$. This method was applied reducing an original maximal coupling of 10^{-2} to 10^{-3}. This is an important step, because we should be able to change the tuning qubit without moving the entangling qubits out of their sweet spot, otherwise we are more sensitive to dephasing.

3.1.3 Get anharmonicity from two tone spectroscopy

Estimating the qubits anharmonicity α is an important factor in qubit characterization. With this we can estimate χ from the coupling g and Δ or the other way around. We can also find E_c and together with its frequency E_j. α is found by exploiting a two photon transition from 0->2. Even though the transmon doesn't allow a single photon 0->2 transition due to the selection rules, a two photon transition is allowed at high powers and at frequency $\omega_{02}/2$. Another way to find α is by saturating the 0->1 transition with one tone, while using a another to drive the 1->2 transition. Now if these tones add up to the 0->2 transition you will also see a response of the resonator frequency - monitored with a third tone - since you also get a stronger dispersive shift from the second level of the qubit. In Fig. 3.5 you can see example measurements of both methods on the two entangling qubits. This resulted in an estimate of $\alpha = -0.34$MHz. We can then use a numerical version of the transmon Hamiltonian to estimate E_c and E_j given the qubit frequency and α. This resulted in $\frac{E_c}{2\pi} = 293$MHz for both entangling qubits.
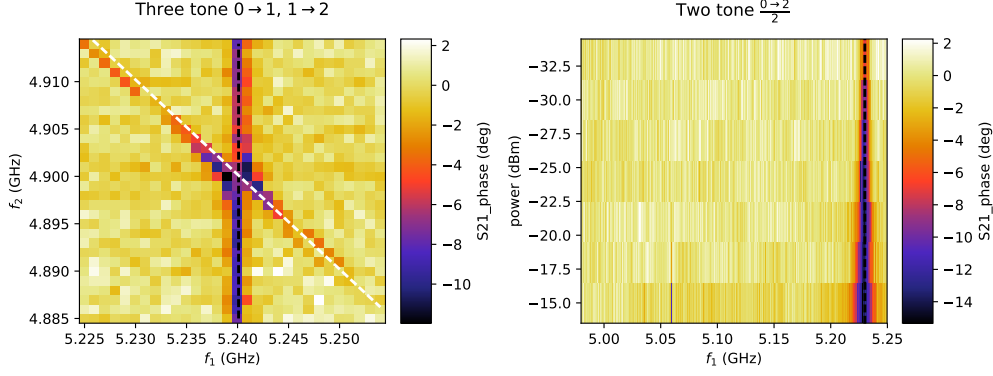
FIGURE 3.5: Three and two tone spectroscopy both giving the anharmonicity. (Left) Three tone spectroscopy using the $0 \to 1$ and $1 \to 2$ transition performed on the entanglement qubit of chip A. Resulted in an anharmonicity of $\alpha = -340$MHz. (Right) Two tone spectroscopy where power was swept versus driving frequency. At higher powers a clear phase shift of the resonator response S_{21} is noticed indicating the $\frac{0 \to 2}{2}$ frequency. From this $\alpha = -340$MHz so both entangling qubits had the same anharmonicity.

3.1.4   Tuning the resonator via the qubits

An important trait of our setup is the fact that we can use the tuning qubits to change the resonator frequency. This allows us to change the relative frequency difference Δ_A, B of the cavities to the readout tone, which are important parameters in making the classical equations of motion 5.3. Now with a compensation pulse from Eq. 5.6 a Δ should not matter for dephasing since the solution compensates for it, but we *do* see a change in readout fidelity due to finite bandwidth of the used JPA and the fact that Δ causes the information to switch between quadratures over time reducing homodyne detection efficiency by a maximum of 50%. In Fig. 3.6 we show how we can tune the frequency of the resonators on both chips by changing the tuning qubits. We placed one tuning qubit above the resonator and one below so we could make their Lamb-shifted frequencies equal. Using the dac-arches we can extract the tuning qubit frequency from bias currents. This allowed us to directly get the resonator frequency as a function of tuning qubit frequency. We then used a numerical simulation of a three level Tavis Cummings hamiltonian with qubit-qubit coupling to fit the data so we obtained the couplings g. The form of it is given in Appendix A. During the sweep of the tuning qubit we also did a pulsed spectroscopy on the entangling qubit of each chip to make sure that the dispersive shift χ didn't change unpredictably as a function of resonator frequency, since χ is also an important parameter modeling the compensation pulse. We found an average $\chi = 335$KHz for both chips and as shown, from the fit we don't expect it to change much.

3.1.5   Estimating Line losses

An important parameter in the final scheme is the loss in the transmission between the cavities $1 - \eta_l$ because each lost photon can be seen as being measured by the environment without us knowing the outcome. The main cause of loss is given by the Palmtech CTH0408KCS circulators. In our scheme photons that are reflected off the first cavity pass two circulators each having 0.09 dB loss. This totals to 0.18 dB or $\eta_l = 0.96$. The
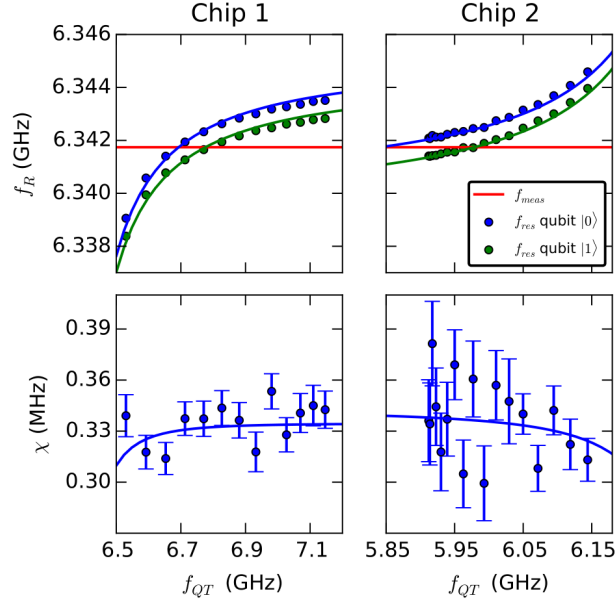
FIGURE 3.6: Resonator frequency f_r (top) and χ (bottom) versus tuning qubit frequency f_{QT} for both chips, showing that we can tune the resonator by a few MHz by applying a flux to the tuning qubits. Lines indicate fits from a three level Tavis Cummings Hamiltonian, modeling the resonator together with the two qubits and their coupling as described in appendix A. Couplings found were $\frac{g_a^E}{2\pi} = 40$MHz, $\frac{g_a^T}{2\pi} = 35$MHz, $\frac{g_b^E}{2\pi} = 40MHz$, $\frac{g_b^T}{2\pi} = 30$MHz. The average dispersive shift is $\frac{\chi}{2\pi} = 335$KHz for both qubits, but the uncertainty varies between the chips as indicated in the figure. Anharmonicity was taken to be -340MHz for all qubits and the entangling qubit frequencies were set at their sweet-spots.

insertion loss from two Rosenberg connectors from chip to transmission line are specified to bounded by $\leq 0.05\sqrt{f(\text{GHz})}$dB so this would at most give 0.13 dB per connector in our frequency range. Other connectors are those of the transmission line itself which we can assume Taking these into account would give $\eta_l = 0.9$. Now there can also be losses due to the wire-bonding of the chip to the PCB further decreasing η_l.

Another parameter of importance in this experiment is the *measurement efficiency* η_m, since this affects the rate of separation of the measurement outcome histograms and thus the minimum amount of measurement time we need. In our setup η_m should equal 1 in a perfectly reflecting measurement [20], but is reduced due to losses after exciting cavity B. Now we of course get some losses due to photons transmitting through the weak port depending on the ratio $\frac{\kappa^w}{\kappa_s}$ but they are already incorporated in the model. The output of cavity B passes through 3 circulators and a Krytar directional coupler giving at most 0.33dB, 0.6dB loss respectively before being amplified by the JPA. The extra circulator was added in to be sure that no JPA pump power leaks back into the system since it was at the same frequency as the measurement tone. Again there was a Rosenberg connector giving a total of 1.04 dB corresponding to $\eta_m \leq 0.78$. Now finite squeezing, the classical amplification chain after the JPA and the fact that in the transient case there is always some information in the other quadrature than the one amplified by the JPA can result in a lower η_m.

TABLE 3.1: Summary of system parameters. How the parameters were obtained is described in the previous sections. κ^w was estimated to be zero, since it was designed to be at least of factor of 300 smaller than κ^s. κ^I was obtained from resonator internal quality factor measurements, where the average $Q_I \approx 500000$.

Parameter	Chip 1 $Q_E(Q_T)$	Chip 2 $Q_E(Q_T)$
$f_{res,bare}$	6.344 GHz	6.339 GHz
$\frac{\kappa^s}{2\pi}$	3.01 ± 0.05MHz	4.54 ± 0.05 MHz
$f_{q,max}$	5.230 (5.81) GHz	5.238 (5.81) GHz
$f_{q,min}$	... (7.32) GHz	... (7.43) GHz
α	-340 MHz	-340 MHz
$\frac{\chi}{2\pi}$	0.335MHz	0.335 MHz
g	40(30) MHz	40(35) MHz
$\frac{\kappa^w}{2\pi}$	≈ 0	≈ 0
$\frac{\kappa^I}{2\pi}$	0.0125 MHz	0.0125 MHz
η_l	...	0.88

3.2 Calibration and monitoring routines

3.2.1 Dephasing and coherence measurements

A large factor in performance of the experiment are the qubits relaxation and dephasing times due to interaction with the unmonitored environment. The effect of this noise the qubits can be described phenomenologically by exponential decay curves of the form $e^{-\frac{\tau}{T_i}}$. We can thus measure the decay of the height of the density matrix elements affected by the noise via standard T_1, Ramsey and Echo measurements. We noticed that sometimes we had big fluctuations in T_1, so we made it standard practice to monitor these times interleaved with all measurements. The results are shown in Fig. 3.7. Here you can see that the entangling qubit on chip 1 had on average a $T_1 = 18\mu s$, the entangling qubit on chip 2 was worse with $T_1 = 9.3\mu s$. This can be explained partially by an enhanced spontaneous emission rate due to the presence of the cavity called the Purcell effect, in the dispersive regime this is given by $T_1^{Purcell} = \kappa \frac{g^2}{\Delta^2}$ [50]. Using typical experimental parameters we obtain for chip A $T_1^{Purcell} = 40.6\mu s$ and for chip B $T_1^{Purcell} = 26.8\mu s$. Another effect that contributes is the dielectric loss of the field going through the silicon substrate of the chip, which increases with frequency [50]. Ramsey times on both entangling qubits were fluctuating anywhere between T_2^{echo} and 0 indicating it being limited by slowly fluctuating charged quasi-particles affecting n_g of the transmon Hamiltonian and causing a change in frequency. T_2^{echo} times were for chip A(B) 15.1μs (27.3μs). The tuning qubits on chip A(B) had much lower T_1 3.8μs (4.1μs), T_2^* 1μs (2 μs) and T_2^{echo} 1.5μs(4μs)

3.2.2 Calibration routines

High gate fidelity is a key element in being able to do reliable experiments. We therefore calibrated our pulses using a technique called DRAG pulsing, where the pulse is improved by superposing it with a second shape that is proportional to the derivative of the first [55, 18]. This minimizes leakage to higher qubit levels due to the pulse, which is necessary due to the relatively small anharmonicity of the Transmons. In order to calibrate the single pulse amplitudes we used Rabi-oscillations of the qubits followed by
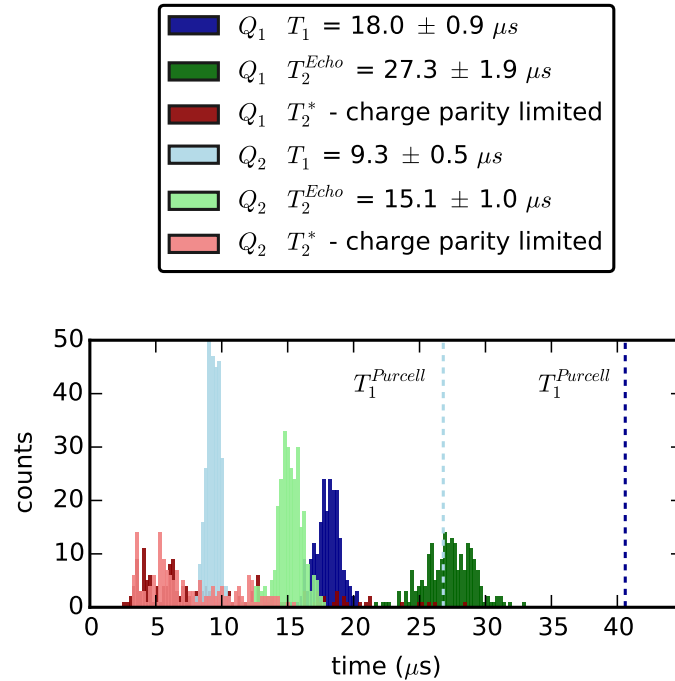
FIGURE 3.7: Histograms of coherence times of the entangling qubits measured inter-leaved with the experiment. T_1 was measured doing a X pulse and waiting for varying times before measuring the qubits. T_{2^*} was measured using a Ramsey sequence con-sisting of a $Y_{\frac{\pi}{2}}$ and $Y_{\frac{-\pi}{2}}$ pulses separated by a varying waiting time τ. In the ideal case we would end up with $|0\rangle$ again, but if ω_{01} fluctuates due to noise we can end up with a different state based on the amount of noise. Averaging all of these random states results in mixture. T_2^{echo} was measured adding in an echo pulse half-way between the Ramsey sequence. This factors out slow noise, since if there is noise that is constant over a single experimental run, the echo will cancel the phase gain during the waiting time τ.

Ramsey measurements to find the detuning of the drive and correct for this. A repeated set of n X pulses was used to calibrate the drive amplitude further since this ampli-fies any over or under-driving by a factor of n. An important calibration measurement was an ALL-XY sequence [66] this is an ordered set of two qubit rotations consisting of $\left\{I, X, Y, Y_{\frac{\pi}{2}}, X_{\frac{\pi}{2}}\right\}$ and shows errors due to detuning, incorrect DRAG parameters, in-correct amplitudes and several more. This made it useful in determining the waiting time of our final measurement after we had done an entangling measurement, since if there are photons left in the resonator the qubit gets a frequency shift χ and this will show up as a detuning error in the ALLXY sequence.

3.3   Entanglement by measurement scheme

3.3.1   Time domain

Measurements pulses were generated on an AWG to activate a constant frequency mi-crowave tone ($\approx$6.34 GHz) where the frequency was chosen for optimal readout condi-tions via simple amplitude based mixing. The readout resonators where measured in reflection. Single Qubit pulses were generated using a second AWG with a sideband modulation frequency of 100MHz and were then mixed with another microwave tone

generator at (100MHz above) the qubit frequency ($\approx$5.4 GHz) to obtain a pulse resonant with the entanglement qubits. This is to avoid driving the qubits when there is no pulse being sent. All microwave tones that were send into the fridge had $\pm$ 60dB of attenuation at various stages in and outside the fridge to minimize noise from thermal radiation. The first AWG also triggered the acquisition card to acquire via a simple trigger pulse before the first measurement. The readout signal was usually amplified by a phase sensitive Josephson parametric amplifier [15] and afterwards by a HEMT(High electron mobility transistor) amplifier at 4K and additional RT amplifiers as to maximize readout fidelity. The acquisition card had a sampling rate of 1GHz so the signal was demodulated to DC after returning from the fridge by mixing it with split signal from the same source. Then for readout the in and out of phase quadratures were recorded in a standard heterodyne scheme. We then integrated a time window corresponding to the measurement, where we implemented an integration weight function and then saved the integrated single shot results. A more detailed wiring diagram is shown in Fig. 3.2.

3.3.2 Pulse scheme

The main goal of this experiment was creating entanglement by measurement. The used pulse scheme can be seen in Figure 3.8. We start the measurement with an initialization measurement to fight thermal excitations of the qubits on which we later post-select. We then are ready to apply $Y_{\frac{\pi}{2}}$ pulses on both qubits as to create the maximum superposition state $|+\rangle |+\rangle$. We then perform a smoothed entangling measurement of t_{ent} ns through the strongly coupled ports at a frequency ω_d near the cavity frequency At this same frequency we also apply a compensation drive to the weakly coupled back port of the second cavity in order to minimize the output transient difference. After this we apply tomographic rotation pulses on both qubits. This is repeated 36 times where the tomographic pulses are varied over the overcomplete set of $\{I, X, X_{\frac{\pi}{2}}, X_{-\frac{\pi}{2}}, Y_{\frac{\pi}{2}}, Y_{-\frac{\pi}{2}}\}$, see Chapter. 4.
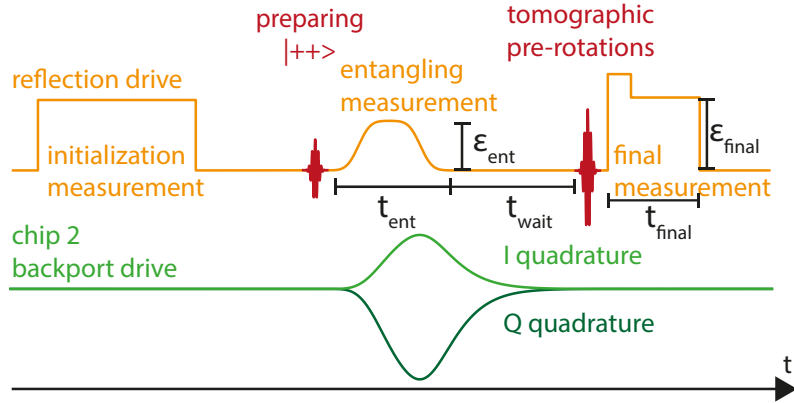
FIGURE 3.8: Pulse scheme of the entanglement-by-measurement scheme. We start with an initialization measurement of $1\mu s$ followed by a 1 μs wait time to empty the cavity, post-selecting on that result corresponding to zero we prepare the $|++\rangle$ state by doing 40 ns $Y_{\frac{\pi}{2}}$ pulses on each qubit. We then immediately send in the entanglement projection pulse for a time $t_{ent} = 300$ ns with amplitude ϵ_{ent}. Before we can do tomography to find out what state we have produced we need to wait a time $t_{wait} = 740$ ns until the cavities are empty. Tomography is performed by doing one of a set of 36 tomographic prerotations each run followed by a final measurement of length $t_{final} = 1 \mu s$ and strength $\epsilon_{final}\epsilon_{ent}$ to be able to dinstinguish all four states.

TABLE 3.2: The 60 pulse sequence. This is repeated for each data point thus giving each independent run of the experiment its own calibration. The overcomplete set of 36 tomographic rotations is denoted by multiplying the set $\{I, X, X_{\frac{\pi}{2}}, X_{-\frac{\pi}{2}}, Y_{\frac{\pi}{2}}, Y_{-\frac{\pi}{2}}\}$ with itself.

#**Pulse**	Q_1^E	Q_2^E	Q_1^F **Final rotations**	Q_2^F **Final rotations**
1	-	-	-	-
2	X	-	-	-
3	-	X	-	-
4	X	X	-	-
5-40	$Y_{\frac{\pi}{2}}$	$Y_{\frac{\pi}{2}}$	$\{I, X, X_{\frac{\pi}{2}}, X_{-\frac{\pi}{2}}, Y_{\frac{\pi}{2}}, Y_{-\frac{\pi}{2}}\}$	$\{I, X, X_{\frac{\pi}{2}}, X_{-\frac{\pi}{2}}, Y_{\frac{\pi}{2}}, Y_{-\frac{\pi}{2}}\}$
40-45	-	-	-	-
45-50	-	-	X	-
50-55	-	-	-	X
55-60	-	-	X	X

We also perform 4×5 repeated calibration measurements for the final Measurement needed to calibrate the measurement operator, where we instead of $Y_{\frac{\pi}{2}}$ pulses create the four computational basis states. We turn off the entanglement pulses during these steps. We then do four more calibration pulses with the entanglement pulse turned on. These calibration points are needed in order to determine the correct threshold region. This thus results in a total of 60 traces per ATS buffer. We then repeat this in the buffer direction for N_{points} times. The complete pulse sequence per data point is also shown in table 3.2 and Figure 3.8. The pulse timing varied between different runs but the ones used in the results shown in Chapter 6 are $t_{ent} = 300$ns, $t_{wait} = 740$ ns. Initial and final measurement pulses were 1 μs and we waited for 1 μs after the initial measurement. t_{wait} Was determined by optimizing on an ALLXY sequence after the entanglement measurement while varying t_{wait} since residual photons in the cavity give detuning which shows up as mismatch to the ideal ALLXY.

3.3.3 Measured data preprocessing

Measurements were acquired in a heterodyne scheme, we therefore had data of both the I and Q quadratures. For single shot measurements we took the integrals of this data over preset time-windows, corresponding to expectation values of Eq. 2.13 but with some constant (over the time of an experiment) phase between them. When doing single shots we had the Josephson parametric amplifier in phase preserving mode to boost readout fidelity'up to 99.9% (corrected for thermal excitation). This effectively made our readout become a homodyne measurement of a single quadrature of the output, so nearly all information in the orthogonal quadrature was lost. This did however allow us to rotate the data after acquisition and process only a single quadrature in the analysis. A typical measurement of the $|++\rangle$ state is given in Figure 3.9. In this figure you can see the blobs corresponding to the four equal populations in the superposition states, where the 01 and 10 overlap a lot due to the nature of our half-parity measurement.

Due to the single-quadrature amplification of the JPA we rotated the data and took the projection of it on a single axis according to

$$\begin{pmatrix} I \\ Q \end{pmatrix} = \begin{pmatrix} \cos\theta & -\sin\theta \\ \sin\theta & \cos\theta \end{pmatrix} \begin{pmatrix} I' \\ Q' \end{pmatrix} \tag{3.2}$$
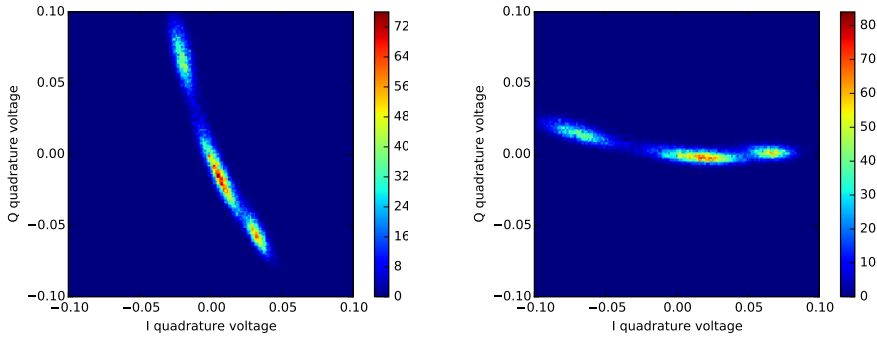
FIGURE 3.9: (A) 2D Histogram of final measurement counts(color) versus I and Q quadrature voltages of a $|++\rangle$ state squeezed by the phase sensitive JPA. One can distinguish the three blobs corresponding to the 00, 01, 10, 11 populations where the 01 and 10 are less distinguishable so form one blob in the middle, (B) Rotated version of A. Nearly all information is now projected onto the I quadrature so that we can switch to looking at the data in a single dimension.

where I', Q' stand for the measured quadratures and θ the rotation angle with an optimal angle determined differently per measurement.

The initial measurement had no calibration points, therefore the best rotation was just one that maximizes the spread in the data in a single quadrature. The other measurements had calibration points and therefore the optimum rotation angle could simple be calculated if we denote the difference in means by $d(\mu_{00}, \mu_{01}) = (d_x, d_y)$, by $\theta_{opt} = \arctan(\frac{d_x}{d_y})$. Note that once an optimal rotation angle has been found, all data points are rotated with the same angle.

3.3.4 Thresholding on the entanglement measurement

Since our protocol only generates entanglement 50% of the time, we need to postselect and discard measurement outcomes that correspond to $|00\rangle$ or $|11\rangle$. We implemented four extra calibration points corresponding to the four basis states for this so we could fit four Gaussians around the expected values of each computational basis state. We can then simply put the middle of our postselection region in the middle between the 01 and 10 fit. If we then set a certain threshold radius we can balance between keeping more overall data and keeping more of the $01,10$ subspace. We can furthermore estimate the remaining population inside our postselected region by integrating the Gaussians inside the post-selected interval. This is evaluated analytically using the error function in the python code, keeping in mind possible orientation switches.

2-Dimensional thresholding

We noticed that driving the JPA in a highly non-linear regime caused "banana-like" shapes in the I-Q plane as can be seen in Fig. 3.9. Projection a non-straight into 1D thus meant we lost information. For the final measurement this was not much of an issue, but in the entanglement measurement, signal to noise ratio is of crucial importance to obtaining good concurrence. We therefore started using Scikit-learn [70] a standard multidimensional classification package for python and implemented a neural network based classifier. This allowed us to threshold in 2D thus not losing information due to
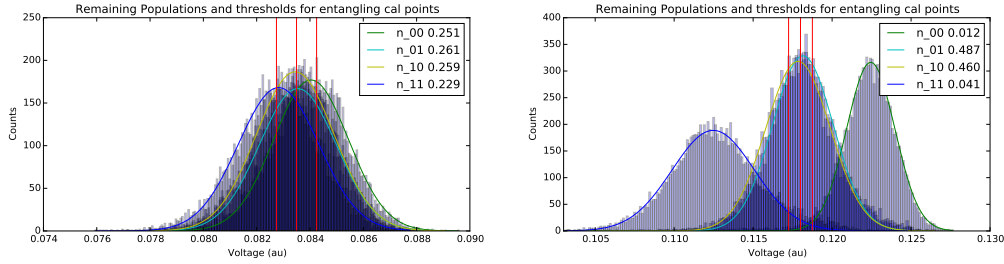
FIGURE 3.10: Entanglement measurement calibration point distinguishability for two different measurement powers. Both measurements contained without selection 12800 points. (A) At weak power $P = 4 \times 10^{-4} mW$ we see all histograms overlapping. The postselection region is given by the red vertical lines where the middle denotes the center. Expected remaining populations after postselection are given in the legend. After selection only (B) At strong power $P = 2.4 \times 10^{-2} mW$ we see that calibration points corresponding to $|00\rangle$ and $|11\rangle$ inputs become distinguishable, but the $|01\rangle$ and $|10\rangle$ do not.

projection on a single axis. We noticed stabler concurrence and an overall improvement over the datasets. An example threshold outcome is shown in Fig. 6.2.d.

3.3.5 Minimizing the transient difference

As shown in sec. 6.1 there is an important relation between transient difference and dephasing due to the measurement. Performing a half-parity measurement means minimizing the dephasing of the 01-10 subspace while maximizing that of the others. Dephasing is directly related to distinguishability which comes from the transient difference. We therefore measured the transients for different detunings set by the tuning qubits to determine the optimal operation point and finally optimized on the following cost function

$$T = d_{01,10} * \sqrt{\left(\sum_{i,j} \frac{1}{d_{ij}^2} \right)} \tag{3.3}$$

where the integrated transient difference is denoted by $d_{i,j} = \sqrt{\int |Y_i(t) - Y_j(t)|^2}$. This basically penalizes $d_{01,10}$ being large, but also penalizes for the other states becoming non-distinguishable in a symmetric way. A comparison of theoretical transient difference landscape and a measured one is given in Fig. 3.3.5. Theory showed that going to higher detunings actually improved the transient difference. This was confirmed by the data, but due to the JPA's finite bandwidth and the fact that measuring at a Δ causes mixing of the output fields in the different quadratures degraded single-shot readout-fidelity, so the optimum concurrence was reached around $\Delta_A = \Delta_B \approx 0$.

3.3.6 Optimizing the compensation pulse

Even though in principle the compensation pulse solution of Eq. 5.6 was for any driving, this did require full knowledge of the system parameters and no distortions of the pulse when arriving at the chip. During the experiment we therefore employed a more experimental approach where we started with the predicted compensation pulse parameters(see table. 3.1) and then optimized on each of them either with Nelder-Mead [60] multi-variable optimization on a combined scan or with simple line scans by hand to
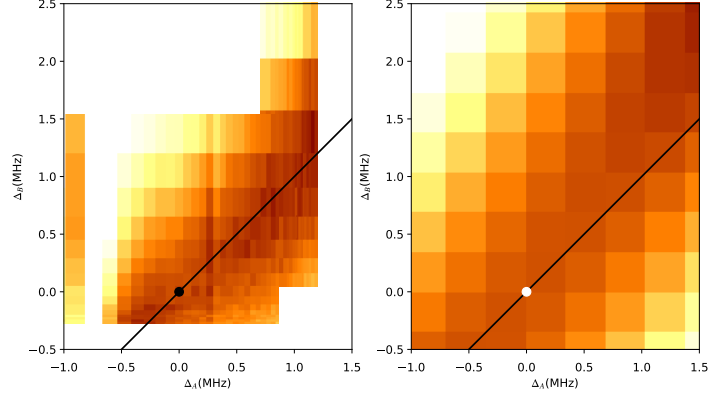
FIGURE 3.11: Qualitative comparison of the transient difference versus detuning. On the left, experimental data using the cost function of Eq. 3.3. On the right theory using the classical equations of motion derived in Chapter 5. Theory showed that going to higher symmetric detunings actually gives a better transient difference value. Line indicates $\Delta_A = \Delta_B$, dot indicates $\Delta_A = \Delta_B = 0$.

confirm we were in an optimal parameter regime. We also included an extra drive scaling factor and phase to account for the cable going in.

3.3.7 Optimizing readout fidelity

Next to minimizing the transient difference, optimizing readout fidelity of the entangling measurement using the JPA was equally important to obtain good concurrence. Tuning the JPA corresponded to varying the JPA pump power, the flux bias line changing its frequency and the phase of the readout tone with respect to the pump. We needed to be able to threshold out the 01-10 subspace from 00 and 11. This required us to simultaneously maximize separability between the histogram corresponding to the 00 outcome and $01, 10$ and the 11 and $01, 10$. A symmetric histogram distribution proved to be the best setting because that corresponds to minimal $00, 11$ subspace population after thresholding. Since certain settings of the JPA could cause squeezing, we could not simply measure use the difference between the means of each calibration point. In order to fully capture the shape we used a way of comparing the full histograms by computing the Bhattacharyya distance [1], which can be seen as the log of the fidelity between two probability distribution

$$D_B\left(p\left(x\right), q\left(x\right)\right) = -\ln\left(BC\left(p\left(x\right), q\left(x\right)\right)\right), \quad BC\left(p\left(x\right), q\left(x\right)\right) = \sum_{x \in X} \sqrt{p\left(x\right) q\left(x\right)} dx$$

$$(3.4)$$
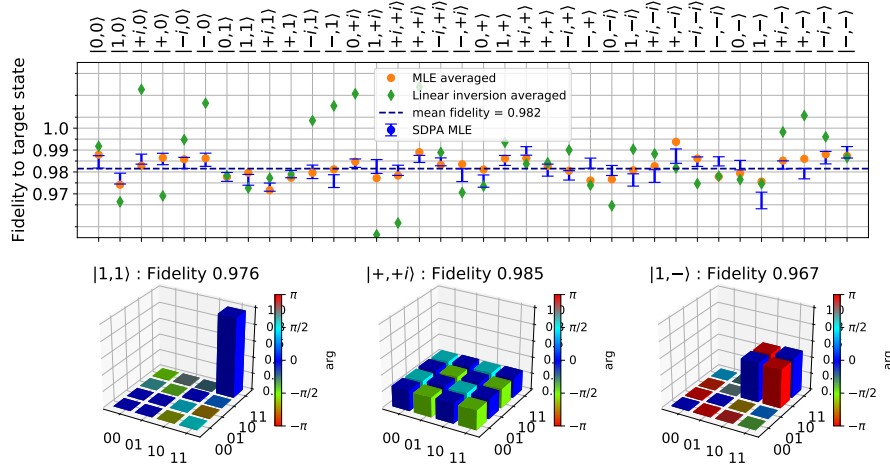
FIGURE 3.12: Tomography performed on the 36 cardinal states with different methods using the same data. Green diamonds indicate Linear inversion tomography results based on averaged data, which can break physicality giving back fidelities higher than 1. Orange(blue) indicate Maximum likelihood estimation with averaged(thresholded) data. Error-bars on the blue points are estimated using the Monte-Carlo simulation from the obtained counts described in sec. 4.3.2.

where $p(x), q(x)$ denote counts of the two histograms we are comparing, x was integrated voltage. We can then maximize the following function

$$F_{ssro} = \sqrt{D_{B_{00,01}}^2 + D_{B_{00,10}}^2 + D_{B_{01,11}}^2 + D_{B_{10,11}}^2} \qquad (3.5)$$

Where $D_{B_{i,j}}^2$ indicates the Bhattacharyya distance between the histogram of calibration point i, j. This forced symmetric output histograms and solved a lot of issues we had with optimizing the JPA settings(flux, power, pump phase).

3.3.8 Tomography

The final step in this experiment is reconstructing the measured state. In chapter 4 we will show two different methods Linear inversion and Maximum likelihood estimation. These can be done based on thresholded data or averaged data but the results are similar. A good test if our tomography performs as expected is a measurement of the 36 cardinal states as shown in Fig. 3.3.8. We obtained an average fidelity of 0.982% showing good general gate performance.

4 Quantum state Tomography

Quantum state tomography is the art of reconstructing unknown quantum states. The term "tomography", meaning reconstruction from slices, comes from the fact that quantum measurements on a state give less information than needed to reconstruct the full state. In order to fully reconstruct an unknown density matrix one needs to measure a state many times with different operators, which can mathematically be seen as estimating the basis coefficients of your density matrix in Hilbert space. Although tomography can be used to reconstruct a state in any dimensional Hilbert space, this Chapter will focus on finite dimensional Hilbert spaces corresponding to qubit states. We will start by explaining the general strategy and how to go from physical measurements to estimations of the measurement operator for two ways of data processing, dividing the measured voltage range in bins and estimate counts of measurements falling in those bins or simply by averaging the integrated voltage outcome in section 4.1. We continue with the different methods of reconstruction in 4.2 and end with estimations of the different types of errors in state tomography and present possible corrections to them in 4.3.

4.1 General Strategy

Say we have n qubits living a complex space of dimension $d = 2^n$, we want to estimate the unknown density matrix $\rho \in \mathcal{H} = \mathcal{C}^{d^2}$. We can define any orthonormal basis $E = \left\{ \vec{e}_i, i = 1...d^2 \right\}$ for ρ and write[1]

$$[\rho]_E = \sum_{i=1}^{d^2} \rho_i \vec{e}_i \tag{4.1}$$

Quantum state tomography then is nothing more than estimating the $d^2 - 1$ independent basis coefficients $[\rho_i]_E = \langle \vec{e}_i \rangle$ of ρ in E, where we have to estimate one less due to the $\text{Tr}(\rho) = 1$ constraint. An example of this basis is the set of Pauli basis vectors $\mathcal{P}^n = \{I, X, Y, Z\}^{\otimes n}$, often chosen since all eigenvalues in this basis are real. The Pauli matrices are given in the computational basis by

$$I, \qquad X = \sigma_x = \begin{pmatrix} 0 & 1 \\ 1 & 0 \end{pmatrix} \qquad Y = \sigma_y = \begin{pmatrix} 0 & -i \\ i & 0 \end{pmatrix} \qquad Z = \sigma_z = \begin{pmatrix} 1 & 0 \\ 0 & -1 \end{pmatrix} \tag{4.2}$$

Where I is the identity matrix. For a single qubit, knowing the the three expectation values $\langle \sigma_z \rangle, \langle \sigma_x \rangle, \langle \sigma_y \rangle$ thus fully determines the (possibly mixed) state of the qubit and have been known in light polarization experiments as the famous Stokes parameters

---

[1]Note that the word *vector* here essentially means *matrix*, since we are talking about a basis for a density *matrix*. The beauty of linear algebra is that we can still write a decomposition in these matrices as a vector of with d^2 components!

for over a hundred years [74] . If we would be able to measure these parameters sequentially we would start out with a 3D sphere, then each measurement takes away one degree of freedom for ρ, thus after a single measurement ρ is constricted to a plane(in our measurement basis), after two measurements this becomes a line and finally we can fully constrain ρ to a point after three measurements.

Now from the projective measurement formalism described in section 1.2.4 we can get an idea of how to get the basis coefficients. We just have to construct a set of s measurements corresponding to known *measurement operators* $\left\{ \hat{M}_i, i = 1...s \right\}$ where each $\hat{M}_i = \sum_{k=1}^{d^2} m_i^k \vec{e_k}$. If these $\hat{M}_i$ span the space, we can reconstruct ρ in any basis B by simply transforming the $\hat{M}_i$ to B and solving a system of equations to obtain the coefficients $[\rho]_B$

4.1.1   Measurement operator for joint dispersive readout

In our system the measurement operator depends on the setup geometry and therefore on the type of coupling between the qubits and readout field. With two qubits the Pauli basis vectors are given by the set $\mathcal{P}^2 = \{II, IX, IY, ..., ZY, ZZ\}$, where we have omitted the tensor product for brevity. For a joint dispersive readout the general projective measurement operator associated with it can be written as a superposition of four of these vectors [30]

$$\hat{M}_0 = \beta_0 II + \beta_1 IZ + \beta_2 ZI + \beta_3 ZZ \tag{4.3}$$

Note that this measurement operator has the computational basis projectors as eigenstates and therefore commutes with the two qubit Hamiltonian. This allows for continuous measurements, because the qubit populations are not affected by the measurement. With a single measurement operator we can only estimate the diagonal components of the density matrix in the basis of the measurement, so we would like to change M_0 as to get estimates for all $d^2 - 1$ coefficients. Instead of changing the setup, which is hard, we can do a trick to change the measurement operator $\hat{M}_0$. We can obtain the $s \geq d^2 - 1$ independent measurements via a basis change performed by unitary rotations R on the qubits before measurement. This follows from the cyclic property of the trace: $Tr\left(R\hat{M}R^\dagger \rho \right) = Tr\left(\hat{M}R^\dagger \rho R \right)$. If we do s two qubit rotations we get the desired collection of s measurement operators

$$\hat{M}_i = R_i^\dagger M_0 R_i, \qquad i \in \{1...s\} \tag{4.4}$$

4.1.2   From physical data to estimates of expectation values

Before the actual methods of tomography are explained, it is more illustrative to show how to get from physical data like Voltages or counts in bins to expectation values. Historically tomography started in the field of quantum optics, where one gets counts corresponding to a photon being detected with a certain polarization or not. With dispersive measurements on superconducting qubits, one measures a set of integrated voltages instead. In this section will be shown that both datasets can be treated in the *same* way and that the expectation values derived from them can be reduced to normal distributed variables with different expressions for the variance and mean.

Averaged Voltage measurements

In an experimental tomography run N_i versions of the same state are prepared for each measurement setting i corresponding to measurement operator $\hat{M}_i$ and the output voltage of one of the field quadratures is integrated as a function of time giving the voltage value m_k^i. We can then estimate the expectation value of the projective measurement operator $\hat{M}_i$ on the input state ρ via the estimator of the mean output voltage

$$\overline{M}_i = \frac{1}{N_i} \sum_{k=0}^{N_i} m_k^i \approx \langle \hat{M}_i \rangle \tag{4.5}$$

Repeating this for different measurement settings i then gives the data required to reconstruct ρ, given that we know the coefficients of $\hat{M}_0$. From a statistics point of view, we can view each integrated voltage m_i^k as a random variable with the distribution governed by a multinomial distribution of the measurement outcome superposed with state independent amplifier noise and the vacuum fluctuations in the voltage signal quadrature. Now if $N_i \gg 1$ we can view the estimator of the mean $\overline{M}_i$, which we will use later in tomography, as a normally distributed variable with mean $\overline{M}_i$ and estimated variance

$$\mathrm{Var}\left(\overline{M}_i\right) = \frac{\mathrm{Var}\left(m_i^k\right)}{N_i} \approx \frac{1}{N_i^2} \sum_{k=0}^{N_i} \left(m_k^i - \overline{M}_i\right)^2 \tag{4.6}$$

due to the central limit theorem holding for a sum of many i.i.d variables. An example set of histograms of measurement outcomes m_i^k for the the input states $|00\rangle, |01\rangle, |10\rangle, |11\rangle$ is given in Figure 4.1. From this you can see that the joint dispersive measurement operator can distinguish the computational basis states within reasonable accuracy. The average voltage values $\overline{M}_i$ can be found by taking the center of the different histograms. The non-Gaussian form of the histograms comes from the parametric amplification and relaxation during the measurement.

Thresholded Voltage measurements

Another way to parse the raw integrated voltages m_i^k is to turn them into binary values via binning the Voltage range. For example, looking at Figure 4.1 again, we can see that if we have enough distinguishability between the means of the Voltages of the four input states, we can assign a newly measured value to one of the four bins corresponding, before corrections from calibration, to one of the four input states. Now say we divide our voltage range into n_b bins, we then get per measurement setting i, consisting of N_i total measurements, $\overline{n}_i^j$ counts in each bin j. From doing calibration measurements (see section 4.1.3) we can obtain a measurement operator corresponding to each bin of the form $\hat{M}_i^j = \sum_{k=0}^{2^n} a_k^j R_i^\dagger \Pi_k R_i$ where the Π_k are the projectors on the eigenbasis of the original measurement operator satisfying $\sum_k \Pi_k = I$ and n is the amount of qubits measured. In the case of the joint dispersive measurement Π_k are just the projectors of the computational basis states. If we normalize the bin operators such that $\sum_j \hat{M}_i^j = I$ or equivalently $\sum_{j=0}^{n_b} a_k^j = 1$ we can see that the average measured number of counts in bin j divided by the total number of measurements for that setting i corresponds to the
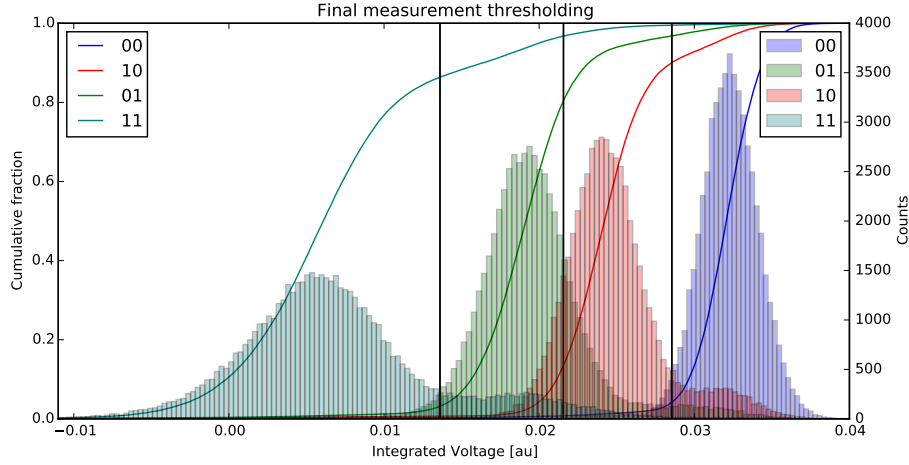
FIGURE 4.1: Measurement of the calibration points of typical experimental data. Histograms(bars) and Cumulative histograms(lines) are plotted vs measured integrated voltages for the $|00\rangle, |01\rangle, |10\rangle, |11\rangle$ states. In total for each calibration point 11300 data points were taken. The thresholds are placed at positions that maximize the difference between consecutive cumulative histograms and denote the different bins. The averages of the voltages can be seen as estimators for the computational basis coefficients a_k of $\hat{M}_0$ in case of averaging, while the counts of calibration point j in bin k can be seen as the coefficient a_k^j in front of P_k for bin j

expectation value of the bin operator

$$\langle \hat{M}_i^j \rangle \approx \overline{M}_i^j = \frac{\overline{n}_i^j}{N_i} \tag{4.7}$$

In order to get an estimate for the variance of these counts we have to look at all bins together. We can restate the above to see that measurement of a single integrated voltage on the input state ρ and assigning that to a bin simply corresponds to drawing from a multinomial distribution where the chance of ending up in a bin j is given by

$$P(j|\rho) = \text{Tr}\left(\hat{M}_i^j \rho\right) \approx \overline{M}_i^j \tag{4.8}$$

Thus measurement either ends up in the bin j with probability $p_j = P(j)$ or not with probability $1 - p_j$. If we then look at the expected number of counts in such a bin we get a Poissonian distribution of counts with mean $\lambda = Np$ which becomes a Gaussian distribution as $\lambda > 10$. So we can estimate the noise on the expectation values of the measurement operator $\overline{M}_i^j$ as Gaussian, which holds again only if $N_i >> 1$. An estimator for the variance for the thresholded case is given by

$$\text{Var}\left(\overline{M}_i^j\right) \approx \overline{n}_i^j / N_i^2 = \frac{\overline{M}_i^j}{N_i} \tag{4.9}$$

This is a convenient normalization, because we can now identify the estimated expectation values of the operators $\overline{M}_j$ from averaged Voltages with the estimated expectation value from the bin operator $\overline{M}_i^j$ and treat tomography algorithms using either method in the same formalism!

4.1.3 Calibrating the measurement operator

A first step in doing any sort of tomography is finding out what measurement operator one is measuring with. In order to find the coefficients β_j to determine $\hat{M}_0$ one needs to input known states. So throughout state tomography one of the key assumptions is that the input states for calibration are perfectly initialized, which immediately gives rise to *state preparation* errors. These errors can be due to imperfect qubit gates or thermal excitation. For the latter we can correct given that the exact thermal excitation percentages on each qubit are known, this is described in section 4.3.1.

Calibration for averaged Voltages

In order to get a complete picture of the system measurement operator $\hat{M}_0$ one needs to measure the eigenvalues corresponding to its eigenstates. In our system the measurement operator can also be expressed in the computational basis via

$$\hat{M}_0 = \sum_{j=1}^{d} a_k \left|k\right\rangle \left\langle k\right|. \tag{4.10}$$

Where $\left|k\right\rangle$ is an eigenstate of $\hat{M}_0$. The a_k can directly be obtained by preparing the eigenstates of $\hat{M}_0$ and measuring the average integrated voltage. In the case of $\hat{M}_0$ being of the form of Eq. 4.3 the $\left|k\right\rangle$ are just the computational basis states. Now if we know M_0 in the computational basis C but are interested in getting $\hat{M}_0$ in any other basis B, like the Pauli basis, we can do a basis transformation $\underset{B \leftarrow C}{\mathcal{F}}$ and obtain the coefficients $\vec{\beta}$ of $\hat{M}_0$ in that basis

$$\vec{\beta} = \underset{B \leftarrow C}{\mathcal{F}} \hat{M}_0 \tag{4.11}$$

where $\underset{B \leftarrow C}{\mathcal{F}}$ is given by the basis vectors of C expressed in B

Calibration for thresholded Voltages

The measurement operators corresponding to bin j in the initial measurement setting can be expressed as $\hat{M}_0^j = \sum_{k=0}^{d} a_k^j \left|k\right\rangle \left\langle k\right|$. We can thus find the coefficients a_k^j again directly by measuring the eigenstates of M_0. So given a set of bins over the voltage range, we need to prepare the d states $\left|k\right\rangle$ and measure the counts n_k^j ending up in bin j for state $\left|k\right\rangle$. We then immediately get the coefficient matrix $a_k^j = \frac{n_k^j}{N_k}$. Where $N_k = \sum_j n_k^j$ the total amount of counts for each input state Π_k.

4.2 Methods of reconstruction

4.2.1 Linear inversion

Say one has a vector of n expectation values of different measurement operators $\langle \vec{M} \rangle$ and from the calibration points the exact form each of these $\hat{M}_i$ are known. To estimate an unknown ρ, we can decompose this in any orthonormal matrix basis $\vec{v}$ and denote $\vec{\rho}$ as a vector length d^2 of projection coefficients on these elements. If we then use the calibration to decompose the measurement operators in this same basis, the following holds

$$\langle \vec{M} \rangle = A \langle \vec{\rho} \rangle \tag{4.12}$$

For some matrix A of dimension $n \times d^2$. The precise form of A depends on the choice of basis and measurement operators. Given that A is (pseudo) invertible, we can obtain the Linear inversion estimate ρ^{LI} of rho by inverting Eq. 4.12. This then gives an estimate for the d^2 coefficients in the matrix basis of ρ

$$\langle \vec{\rho}^{LI} \rangle = A^{-1} \langle \vec{M} \rangle \tag{4.13}$$

From these we can simply reconstruct $\hat{\rho}^{LI} = \vec{\rho}^{LI} \cdot \vec{v}$. Note that although we can enforce constraints like Hermicity and trace one, the method doesn't guarantee the estimated ρ^{LI} to have non negative eigenvalues and we can therefore arrive at non-physical density matrices.

Linear inversion based on cardinal state rotations

The set of rotations used to arrive at a complete set of measurement operators is arbitrary, in the experiments performed in this thesis we chose an overcomplete set of rotations $\{R_i, i \in [1,36]\}$ mapping a Pauli basis vector ν to another Pauli basis vector ν', which are also called cardinal state rotations since the Pauli basis vectors correspond to the cardinal states on the Bloch sphere. Using the measurement operator from Eq. 4.10 consisting of a sum of only k Pauli basis vectors the coefficient matrix A is of dimension $s \times d^2 - 1$ and contains only $k - 1$ nonzero entries in each row

$$A_{ij} = \begin{cases} \beta_{q_l} & \text{if} \quad \exists\, q_l \in q : R_i \nu_{q_l} R_i^\dagger = \nu_j \\ -\beta_{q_l} & \text{if} \quad \exists\, q_l \in q : R_i \nu_{q_l} R_i^\dagger = -\nu_j \\ 0 & \text{otherwise} \end{cases} \tag{4.14}$$

Where the column corresponding to $v_{q_0} = II$ can be left out since the coefficients are simply one and we can save computational power by not including that in the inversion.

4.2.2   Physicality constraints: Maximum likelihood estimation

In order to force physicality of the estimated density matrix ρ, we need to find the closest ρ matching our data, but satisfying the following constraints for it to represent an ensemble of physical states.

1. The law of total probability should hold, $\text{Tr}\,(\rho) = 1$

2. ρ should be Hermitian in order for its eigenvalues to be real, $\rho = \rho^\dagger$

3. ρ should be positive, $\langle \psi | \rho | \psi \rangle \geq 0 \qquad \forall\, |\psi\rangle \in \mathcal{H}$ because negative eigenvalues would correspond to negative probabilities of obtaining the corresponding eigenstate.

These constraints can be enforced by optimizing a parameterization $\rho\,(\vec{t})$ of ρ such that it follows these constraints. We can then simply optimize the parameters t_i to find a $\rho\,(\vec{t})$ that matches the data best.

Minimization function

Let's define $\overline{M}_i$ the measurement outcomes corresponding to a measurement of measurement operator $\hat{M}_i$. These can thus either be the averaged measured integrated voltages or probability to end up in one of the bins. We can assume that each measurement outcome is independent of the other and in the previous section we have derived that they follow a Normal distribution, therefore the probability density function of obtaining a set of outcomes $\overline{M}_i$ given some system state ρ is given by

$$p\left(\overline{M}_0, ..., \overline{M}_s | \rho\right) = \prod_{i=0}^{s} \frac{1}{\sqrt{2\pi\sigma_i}} e^{-\frac{(\overline{M}_j - \langle \hat{M}_j \rangle)^2}{2\sigma_j^2}} \tag{4.15}$$

where $\langle \hat{M}_j \rangle = \text{Tr}\left(\hat{M}_j \rho\right)$ and the variances σ_j^2 are given by Eq. 4.6, 4.9 for the averaged or thresholded case respectively. If we now fix the $\overline{M}_i$ from the data and then vary ρ instead we can see the above equation as the likelihood function $\mathcal{L} = p\left(\rho | \overline{M}_0, ..., \overline{M}_s\right)$ having ρ as a system state given the measured data. Regardless of our parametrization of ρ we can use some algorithm to maximize this likelihood so we obtain the maximum likelihood estimate ρ^{MLE} via maximizing

$$\log\left(\mathcal{L}\right) = \sum_{i=0}^{s} -\frac{1}{2}\log\left(2\pi\sigma_i\right) - \frac{1}{2\sigma_i^2}\left(\overline{M}_i - \langle \hat{M}_i \rangle\right)^2 \tag{4.16}$$

where the first term on the left can be neglected in the optimization since as $N_i \gg 1$ the variance per point will depend mostly on the data and not on the estimated ρ. We can thus see this as a weighed least square optimization of finding the ρ^{MLE} that minimizes the function

$$f^{MLE}(\rho) = \sum_{i=0}^{s} w_i \left(\overline{M}_i - \text{Tr}\left(\hat{M}_i \rho\right)\right)^2 \tag{4.17}$$

where the weights $w_i = \frac{1}{\sigma_i^2}$ depend on the total number of data points N_i used to calculate the estimator $\overline{M}_i$ and the type of measurement used, e.g thresholding or averaging. Note that this formula only holds if the noise in the estimators can be assumed to be that of a Normal distribution.

Parametrization of the density matrix

In the above we have not explicitly defined any parametrization t of ρ. We now do this by defining a parameterized lower triangular matrix $T(t_1, ...t_{d^2})$ which for $d = 4$ looks like

$$T(\vec{t}) = \begin{pmatrix} t_1 & 0 & 0 & 0 \\ t_5 + it_6 & t_2 & 0 & 0 \\ t_{11} + it_{12} & t_7 + it_8 & t_3 & 0 \\ t_{15} + it_{16} & t_{13} + it_{14} & t_9 + it_{10} & t_4 \end{pmatrix} \tag{4.18}$$

we can easily prove [2] that with

$$\rho^{MLE}(\vec{t}) = \frac{T^\dagger T}{Tr\left(T^\dagger T\right)} \tag{4.19}$$

Trace one, positivity and Hermicity are guaranteed. The optimum parameter vector $\vec{t}$ is then given by minimizing Eq. 4.17. In order to minimize this any standard minimization algorithm can be used. This method was implemented in python and can be found in Github.

Convex optimization

Instead of running some standard minimization algorithm to minimize the quadratic function Eq. 4.17 with a parametrization of ρ from Eq. 4.18 one can also use the approach described in [25]. This was investigated in order to increase the speed of the optimization, because a two qubit density matrix already gives a 15 dimensional minimization problem and calculating rho from the triangular matrix back and forth is an expensive operation.

The physicality constraints can also directly be included in a constrained minimization problem [25]. The idea is to convert the quadratic expression 4.17 into a linear convex optimization problem by first transferring the non linear optimization problem to it's dual with a linear objective function and non-linear constraints. Then you can make use of a trick involving Shur's complement as to reduce the non-linear constraint to a linear one. This then makes the problem solvable by a semidefinite program in about under 50ms compared to about 0.3-1s for the triangular matrix decomposition.

4.3 Errors in state tomography

As stated in section 4.1.3, quantum state tomography relies on the assumption that the calibration points are perfectly initialized, which is not always the case. There are also other possible errors and we can categorize errors in three categories [3]:

- Errors in the measurement operator(or measurement basis)

- Errors from the counting statistics and amplification errors.

- Errors due to drift in the setup during a tomography run.

The first type of error can be due to finite gate infidelities, thermal excitation afflicting your calibration points or a even microwave phase instability during demodulation of the measurement signal. We can in principle find these errors using *gate set tomography* [39] and correct for them, but this will require many operations to fully characterize all errors. The second kind of error is simply due to counting statistics and the fact that we have a finite amount of measurements or counts used to estimate the $\langle \hat{M}_i \rangle$. This error can in principle be quantified directly by error propagation in quantities like concurrence or state fidelities, but in practice with the current state of computer power it is easier to do Monte-Carlo simulations combined with repeated tomography to obtain estimates of the error, see section 4.3.2. The effect of finite amplification can in the averaged voltage case be seen as an increasing in the variance of the Gaussian estimator in the mean. In the thresholded case this effect corresponds to the bins becoming less orthogonal, therefore reducing the total amount of information per measurement. The third kind of error due to drift in the measurement setup is already reduced in our

experimental protocol as described in table 3.2 since we take all 36 rotations and the calibration points in each single shot buffer of the acquisition card. But it can be reduced by increasing experimental repetition rates relative to the drift rate of system parameters.

4.3.1   Effect of Thermal excitation

With increasing gate fidelities, thermal excitations are the biggest source of error in superconducting qubits, but can be reduced via smart state initialization. Initialization is usually done by waiting for relaxation to the ground state by setting the experimental repetition rate longer than any coherence time of the qubits, by actively measuring and then resetting the qubits [13] or by conditioning the experiment on postselected results and simply throwing away the states that where not started in the ground state[CITATION?]. In the presence of remaining thermal excitation after one of these methods have been performed, the calibration points will become mixed states and skew the tomography results. If the amount of thermal excitation is known per qubit, we can simply write the mixture of the ground state projector in the 2 qubit case by

$$P'_{00} = (1 - p_{e_{01}}) (1 - p_{e_{10}}) P_{00} + p_{e_{01}} (1 - p_{e_{10}}) P_{01} + p_{e_{10}} (1 - p_{e_{01}}) P_{10} + p_{e_{01}} p_{e_{10}} P_{11} \tag{4.20}$$

where $p_{e_{01}}$ is the excitation fraction in qubit 2, $p_{e_{10}}$ the excitation fraction of qubit 1, and P_{ij} the projector onto state $|ij\rangle$.

In Figure 4.2 the effect of thermal excitation is shown via a simulation of tomography data on a partially mixed and entangled state $pI + (1 - p) + \frac{1}{2}(|01\rangle + |10\rangle)(\langle01| + \langle10|)$. The simulation is performed by skewing the P_{00} via Eq. 4.20 and applying X rotations to obtain the other calibration points, while still assuming in the tomography that they are pure states. The effect is basically an increase in purity in the estimated state, due to the fact that the calibration points(which we take as pure states) have a finite amount of mixture in them. The resulting increase in purity can give an increase in concurrence if the state is a combination of I and some entangled pure state.

Now given we know the exact amounts of thermal excitation per qubit, we can correct for this skewing in tomography by simply assuming the calibration points to be mixed states in the measurement operator calibration sequences. For the joint dispersive $\hat{M}_0$, the eigenstates are the computational basis states and thus putting the corrections of Eq. 4.20 in Eq. 4.10 allows us to obtain a more realistic estimate of $\hat{M}_0$

4.3.2   Monte-Carlo Error Estimation

The advantage of being able to do fast tomography with knowledge of the underlying probability distributions of our data is that we can now apply a simple Monte Carlo to estimate the errors. When thresholding, the measured bin counts directly can be used to sample from a multinomial distribution with these mean counts. If we then repeat this procedure multiple times and re-perform the tomography we can get an estimate of the spread in our concurrences and other non-trivial parameters, by simply averaging them over the generated larger data set of density matrices.
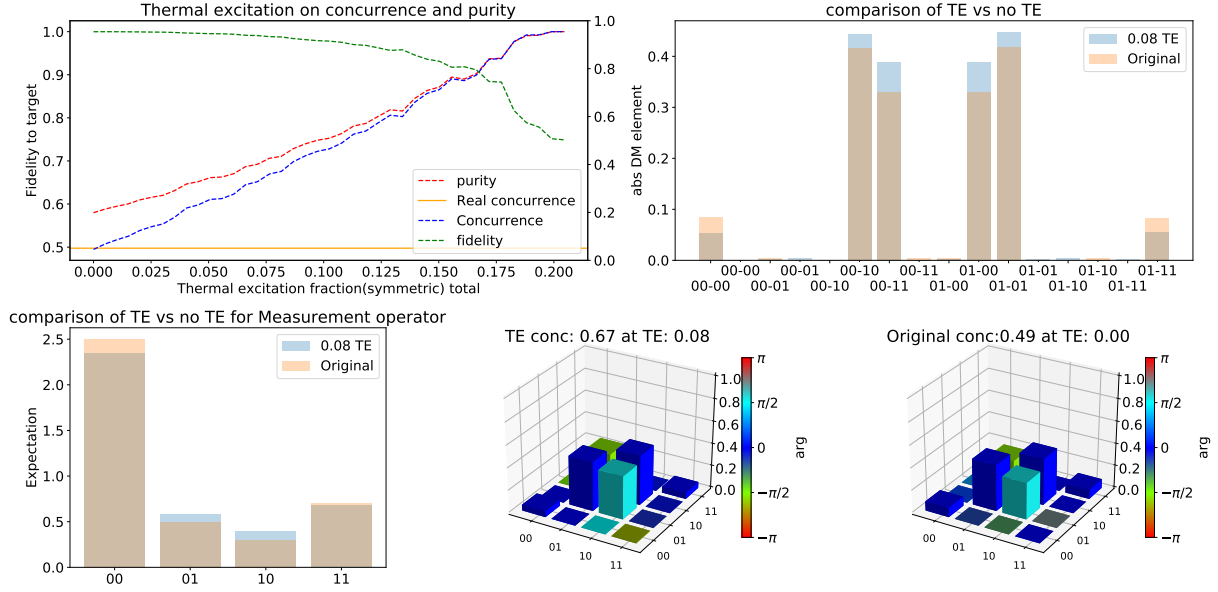
FIGURE 4.2: Effect of thermal excitation in calibration points on the estimated final state concurrence of a typical experimental state. (Bottom right) Test state with 0.50 concurrence and 0.58 purity. (Top left) Purity and concurrence of the test state versus symmetric thermal excitation percentage in both qubits. (Top right) Comparison of the absolute value of different computational basis state elements with 0 or 8% thermal excitation showing an increase of the coherent elements. (Center bottom) 3D density matrix plot of the state with 8% thermal excitation. (Bottom left) Measurement operator with and without 8% thermal excitation in the calibration points. As the thermal excitation grows, the measurement operator comes closer to the identity due to the mixture of the calibration points.

4.3.3   Chi Squared goodness of fit

From the above sections we have learned that noise in tomography does not only come from statistical noise in the estimators $\overline{M}_i$, but also from other sources. Via the chi-squared goodness of fit we can check if the noise on our data agrees with the noise that we expect from purely the projective measurement statistics on a finite amount of data points [51]. The (reduced) chi-squared value is given by

$$\overline{\chi}^2\left(\rho\right) = \frac{1}{s-c} \sum_{i=0}^{s} \frac{\left(\overline{M}_i - \mathrm{Tr}\left(\hat{M}_i\rho\right)\right)^2}{\sigma_i^2} \tag{4.21}$$

where s are the total amount of measurements, $\overline{\rho}$ is the reconstructed rho and c denotes the degrees of freedom of $\overline{\rho}$, $c = d^2 - 1$ for fully mixed states and $c = d^2 - d$ for pure states. For partially mixed states we can approximate c by looking at the eigenvalues of the estimated rho [51]. For a dataset coming from purely statistical noise $\overline{\chi}^2 \approx 1$. The variance of this value, given that the residuals are Gaussian variables is $\sigma_\chi^2 = \frac{2}{s-c}$, thus for 2-qubit tomography we get $0.25 \leq \sigma_\chi \leq 0.28$.

5 Modeling and simulation of the Cascaded 2 chip system

This Chapter will describe the modeling of our full experimental setup. This is done by viewing the two systems as separate systems coupled via a boson field like we described in section 2.5.1. We will start with an introduction to the full system in section 5.1, then move to explaining the classical equations of motion that result by coherently driving the system in section 5.2 and use those equations to derive an expression for a compensation drive into the second chip that can improve the desired half-parity measurement in section 5.2.1. Modeling the full system is computationally very expensive so we show a qubit-only master equation using the polaron transformation in section 5.2. We then introduce an extra term to the model describing the stochastic measurement process in section 5.4 and finally comment on how to solve them in section 5.5

Introduction

Seven years after the formulation of input-output theory, Gardiner [34] and Carmichael [14] simultaneously improved on it by describing how to model cascaded quantum systems. This was an unorthodox point of view, since usually a larger quantum system cannot just be taken apart and we have to describe the dynamics by the Hamiltonian of the system as a whole. They show that whenever you can assume a large Markovian boson bath like in Eq. 2.17 to lie between the two systems, you can model the systems separately, only coupling the output of one system to the input of the other. This description of modular components coupled by boson fields laid the foundation for the later derived SLH formalism [37, 38]. SLH describes a large set of automated rules with which you can get a input-output relation for a large system composed multiple modular components. The set of rules allows for a classical VHDL like circuit automation language describing complex quantum circuits including those using feedback.

5.1 System description

In this section we will model the cascaded setup as it is used for a half parity measurement in the actual experiment. It consists of two chips(A and B) coupled together with a transmission line and each containing a qubit coupled to a cavity. A schematic version is given in Fig. 5.1. Both A and B satisfy the dispersive JC Hamiltonian described in Eq. 2.15 denoted by H_A and H_B respectively. Both cavities are asymmetrically capacitively coupled with strengths κ_i^s, κ_i^w for strong, weak port of cavity i respectively as described for each single cavity in Fig. 2.7 and the strong output of cavity A is coupled via a transmission line to the strongly coupled input of cavity B. We drive the system in
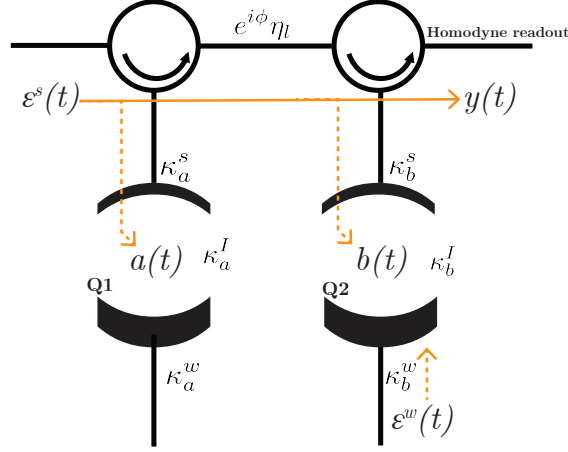
FIGURE 5.1: Schematic of a 2 chip setup with a single qubit coupled to each resonator split by a long(many λ) transmission line. The input field is denoted by ϵ^s and has units $\sqrt{\frac{photon}{s}}$, decay constants of resonator i are given for the strong κ_i^s and weak port κ_i^w and an extra internal loss channel denoted by κ_i^I. Each cavity contains a qubit, the readout signal reflects first of cavity A, then bounces to cavity B where a back-port drive ϵ^w is send in through the weak port of cavity B.

reflection via the strong input of cavity A coherently with $\epsilon^s(t)$ and the weak input port of cavity B with $\epsilon^w(t)$ allowing for compensation.

5.1.1 Full system master equation

Using SLH or just cascaded system theory one can derive the master equation describing the full two qubit system. This was done in ref [56] giving

$$\frac{d\rho}{dt} = -i\left[H', \rho\right] + \mathcal{L}_c\rho + \mathcal{L}_q\rho$$

$$\mathcal{L}_c\rho = D\left[\sqrt{\kappa_a^s(1-\eta_l)}a\right]\rho + \left(\kappa_a^w + \kappa_a^I\right)D\left[a\right]\rho + \left(\kappa_b^w + \kappa_a^I\right)D\left[b\right]\rho + D\left[-\sqrt{\kappa_a^s\eta_l}a + \sqrt{\kappa_b^s}b\right]\rho$$

$$\mathcal{L}_q\rho = \sum_{i=1}^{2}\gamma_\phi^i D\left[\sigma_z^i\right] + \gamma^i D\left[\sigma_-\right]$$

$$\tag{5.1}$$

where ρ is the combined state of the two qubits and cavities, the dissipation superoperators in $\mathcal{L}_q$ resemble the dephasing and relaxation of qubit i with rates γ_ϕ^i, γ^i respectively, the cavity decay superoperators $\mathcal{L}_c$ are described term by term. $\kappa_a^w D\left[a\right] + \kappa_b^w D\left[b\right]$ represent leakage out of the weak ports of cavity A and B. $D\left[\sqrt{\kappa_a^s(1-\eta_l)}a\right]$ represents the part $(1-\eta_l)$ of the output of cavity a that is dissipated due to the lossy transmission line and $D\left[-\sqrt{\kappa_a^s\eta_l}a + \sqrt{\kappa_b^s}b\right]$ represents the coherent field leaking out of cavity B after reflection and interaction with both qubit cavity systems. This term thus represents the monitored field in the experiment, which has to be described by a combined dissipation operator of cavity A and B. This represents the fact that after reflection off of both cavities we cannot distinguish from which cavity the photons decayed. H' is the complete

system Hamiltonian given by

$$H' = H_A + H_B + H'_c + H'_d$$

$$H'_c = -i\frac{\sqrt{\eta_l \kappa_a^s \kappa_b^s}}{2}\left(a^\dagger b - b^\dagger a\right)$$

$$H'_d = i\sqrt{\kappa_a^s}\left(\epsilon^s(t)a^\dagger - \epsilon^{*s}(t)a\right) - i\sqrt{\kappa_b^s \eta_l}\left(\epsilon^s(t)b^\dagger - \epsilon^{*s}(t)b\right) + i\sqrt{\kappa_b^w}\left(\epsilon^w(t)b^\dagger - \epsilon^{*w}(t)b\right)$$

$$(5.2)$$

where H_A, H_B are the isolated dispersive Hamiltonians, H'_c is the emergent coupling between the cavities due to the transmission line. This coupling seems symmetric even though there are microwave circulators forcing one-way coupling, but irreversibility is preserved nevertheless due to the dissipation operators in $\mathcal{L}_c$ [14, 56]. H'_d represents the effect of driving the system through the strong port of cavity A and weak port of cavity B.

5.2 Solutions to the classical equations of motion of the cavities

Just like we did in section 2.5.3, we can derive the Heisenberg equation of motion for the cascaded system. Taking the expectation value immediately we end up with the following set of coupled linear differential equations

$$\dot{\alpha}^\pm(t) = \left(-i(\Delta_a \pm \chi_a) - \frac{1}{2}\overline{\kappa}_a\right) + \sqrt{\kappa_a^s}\epsilon^s(t)$$

$$z^\pm(t) = \sqrt{\kappa_a^s}\alpha^\pm(t) - \epsilon^s(t)$$

$$\dot{\beta}^{\pm\pm}(t) = \left(-i(\Delta_b \pm \chi_b) - \frac{1}{2}\overline{\kappa}_b\right) + \sqrt{\kappa_b^s \eta_l}e^{i\phi}z^\pm(t) + \sqrt{\kappa_b^w}(t)$$

$$y^{\pm\pm}(t) = -\sqrt{\kappa_b^s \eta_l}e^{i\phi}z^\pm(t) + \sqrt{\kappa_b^s}\beta^{\pm\pm}(t)$$

$$(5.3)$$

where the qubit 0(1) state is denoted by $+(-)$, $\alpha^\pm, \beta^{\pm\pm}$ denote the two qubit state dependent coherent states inside cavity A and B respectively, $z(t)$ denotes the reflected output field of cavity A, $y(t)$ denotes the monitored output field after reflection off both cavities and $\overline{\kappa}_i = \kappa_i^s + \kappa_i^I + \kappa_i^w$ is the total decay of cavity i. Note that these equations fully describe the evolution of the coherent cavity fields and output fields in the dispersive approximation given a qubit state without energy decay.

The above set of equations can be seen as an Linear time invariant system(LTI), so it can be readily solved in the Fourier domain. In Fig. 5.2 this is illustrated as each cavity gives a qubit state dependent response to an input field at the strong or weak port. The solutions are given in the Fourier domain by

$$\alpha^\pm(\omega) = H_a^\pm(\omega)\epsilon^s(\omega)$$

$$z^\pm(\omega) = H_{a^R}^\pm(\omega)\epsilon^s(\omega)$$

$$\beta^{\pm\pm}(\omega) = \sqrt{\eta_l}e^{i\phi}H_b^\pm(\omega)H_{a^R}^\pm(\omega)\epsilon^s(\omega) + \sqrt{\frac{\kappa_b^w}{\kappa_b^s}}H_b^\pm\epsilon^w(\omega)$$

$$y^{\pm\pm}(\omega) = \sqrt{\eta_l}e^{i\phi}H_{a^R}^\pm(\omega)H_{b^R}^\pm\epsilon^s(\omega) + \sqrt{\kappa_b^w}H_b^\pm(\omega)\epsilon^w(\omega)$$

$$(5.4)$$

where $H_j^\pm = \frac{\sqrt{\kappa_j^s}}{i\omega + i(\Delta_j \pm \chi_j) + \frac{1}{2}\kappa_j}$, $j \in \{a, b\}$ are the transfer functions into cavity A and B and $H_{jR}^\pm = \sqrt{\kappa_j^s} H_j^\pm - 1$ is the transfer function after reflection from them. This approach shows clearly that cascading systems entails a simple multiplication of their transfer functions.
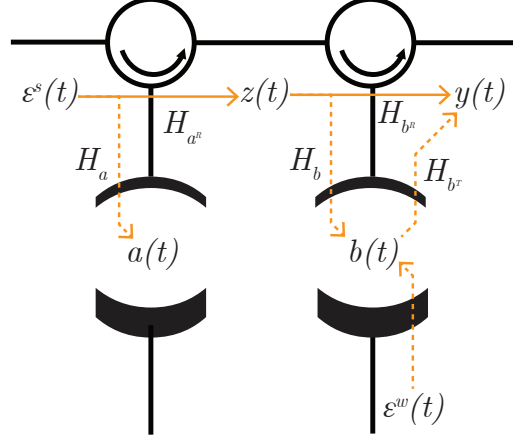
FIGURE 5.2: Transfer function scheme of the 2 chip setup showing we can view the cascaded system as an LTI with qubit state dependent transfer functions representing cavity response due to arbitrary inputs ϵ^s and ϵ^w.

5.2.1 Compensating transient difference

Since we monitor the output field of the cavities and from Eq. 2.33 we know that if the output fields for two qubit states are equal and there is no inter-cavity loss we don't dephase a superposition of those states by the measurement. Is is therefore informative to look at the difference in output fields. We can either tune the transfer function such that the desired outputs are equal, but that requires changing system parameters, which is usually only available through fabrication. A novel approach is therefore the use of a compensation pulse which we have derived for this experiment from the solutions in the Fourier domain. By sending a drive through the weak input port we make nearly any pair of the four classical output states equal by solving

$$y^{kl} = y^{mn} \tag{5.5}$$

where y is the qubit state dependent output field of Eq. 5.4, k, m denote the state of the first qubit and l, n of the second qubit. Solving this, we can obtain an expression for the compensation field ϵ^w as a function of ϵ^s

$$\epsilon_{y^{k,l}=y^{m,n}}^w(\omega) = \frac{\sqrt{\eta_l}e^{i\phi}\left(H_{a^R}^k(\omega)H_{b^R}^l(\omega) - H_{a^R}^m(\omega)H_{b^R}^n(\omega)\right)}{\sqrt{\kappa_b^w}\left(H_b^n(\omega) - H_b^l(\omega)\right)}\epsilon^s(\omega) \tag{5.6}$$

This is an important result, since it allows us to prevent dephasing of the two qubit density matrix element $\rho_{kl,mn}$ and therefore create an odd ($y^{01} = y^{10}$) or even ($y^{00} = y^{11}$) parity state regardless of fabrication imperfections! Note that we have the condition $n \neq l$ due to the denominator, so we cannot make any of the outputs equal that only affect cavity A, e.g $y^{00} = y^{10}$ or $y^{11} = y^{01}$. Note that a similar compensation has already

been presented in [56] but we have solved it differently allowing for an easy general solution and implementation in the actual measurement routine.

5.3 Simulating in other frames

This section will discuss simulating Eq. 5.1, which describes the average evolution of the density matrix. We will then move on to simulating single trajectories.

5.3.1 Simplifying the master equation

We can see Eq. 5.1 as a system of differential equations of dimension $d^2 = \left(4n_{Fock}^2\right)^2$ where n_{Fock} is the amount of Fock states taken into account in the simulation. The number of Fock states depends on the driving amplitude and should be large enough such that the higher Fock states occupation numbers remain sufficiently close to zero.

$$\dot{\rho} = \mathcal{L}\rho \tag{5.7}$$

where the superoperator $\mathcal{L}$ can be written as a single $d^2 \times d^2$ dimensional matrix acting on the d^2 components of ρ or as a d^2 dimensional matrix with more separate terms given by the master equation if memory is an issue at the cost of computation power. The dimensions of this system thus rapidly increases with n_{Fock}. If we would take into account up to 20 photons per cavity, which is needed to resemble experimentally used amplitudes we already have a system of $(4 * 400)^2 = 2.56$ million equations. Since this is a very sparse system optimization routines are available. A good easy to use package for this is Qutip [46] which was also used initially in this thesis, but memory and computation time became a real issue(we took solving the full master equation as benchmark and this took 8 hours to simulate a single data point at a relevant amplitude).

As described in the single cavity case, we can make use of the Polaron transform $\rho^P = U^\dagger \rho U$ to displace the cavity fields to the vacuum using the solution to Eq. 5.3. For our cascaded system this transformation becomes [56]

$$\rho^P = \text{Tr}_{a,b}\left\{U^\dagger \rho U\right\}, \qquad U = \sum_{i,j} P_{ij} D_a\left[\alpha^i\left(t\right)\right] D_b\left[\beta^{ij}\left(t\right)\right] \tag{5.8}$$

where $P_{ij} = |i\rangle_a \langle i| \otimes |j\rangle_b \langle j|$ are the two qubit state projectors of the qubits in cavity A and B, $D_a(D_b)$ is the displacement operator for cavity A(B), the classical cavity field solutions $\alpha^i\left(t\right), \beta^{ij}\left(t\right)$ are given by taking the inverse Fourier transform of Eq. 5.4 and $\text{Tr}_{a,b}$ denotes trace over the cavities, which is trivial since they will remain in the vacuum state in this frame. Applying this transformation to Eq. 5.1 and dropping all terms involving the cavity mode operators a, b - since in this frame the cavities remain in the vacuum state and therefore do not participate in the dynamics - gives a master equation for the qubit degrees of freedom alone [56]

$$\dot{\rho}^P = -\left[H_q, \rho^P\right] + \mathcal{L}_q \rho^P + \mathcal{L}'_q \rho^P$$
$$H_q = i\left(\epsilon^s\left(\sqrt{\kappa_a^s}\Pi_a^\dagger - \sqrt{\kappa_b^s}\Pi_b^\dagger\right) - \epsilon^{*s}\left(\sqrt{\kappa_a^s}\Pi_a - \sqrt{\kappa_b^s}\Pi_b\right) + \sqrt{\kappa_b^w}\left(\epsilon^w\Pi_b^\dagger - \epsilon^{*w}\Pi_b\right)\right)$$
$$\mathcal{L}'_q = \left(\kappa_b^w + \kappa_b^I\right)D\left[\Pi_b\right] + \left(\kappa_a^s\left(1 - \eta_l\right) + \kappa_a^w + \kappa_a^I\right)D\left[\Pi_a\right] + D\left[-\sqrt{\kappa_a^s\eta_l}\Pi_a + \sqrt{\kappa_b^s}\Pi_b\right]$$
$$\tag{5.9}$$

where $\Pi_a(t) = \sum_{i,j} P_{ij} \alpha^{ij}(t)$, $\Pi_b(t) = \sum_{i,j} P_{ij} \beta^{ij}(t)$ are defined as cavity state time-dependent qubit projectors for ease of notation. $\mathcal{L}'_q$ represent information on the qubit states leaking out of the cavities and therefore dephasing the qubits.

Simulating Eq. 5.9 now only requires solving for the Hilbert space of the two qubits alone giving a system $d^2 = 16$ equations! We do need to transform ρ^P back to the lab frame at the end of the simulation. This can be done by re-adding the vacuum cavities and tracing them out after applying the inverse polaron transform to obtain the qubit only density matrix ρ_q in the lab frame

$$\rho_q(t) = \text{Tr}_{a,b} \left\{ U(t) |0_a, 0_b\rangle \langle 0_a, 0_b| \otimes \rho^P(t) U^\dagger(t) \right\} \tag{5.10}$$

If the cavities in the lab frame are in the vacuum, which happens if we do not drive the system or wait for a long time after having driven the system, $\rho_q = \rho^P$. Note that this whole procedure is exact in the dispersive regime and in the absence of T_1 processes of the qubits.

A final simplification we could take is to perform the transformation of Eq. 5.10 analytically and simulate the master equation for the qubits only directly in the lab frame instead of transforming back afterwards. This is derived in [56] and the resulting master equation is

$$\dot{\rho}_q = \sum_{ijkl} a_{ijkl}(t) P_{ij} \rho_q(t) P_{kl} + \mathcal{L}_q \rho_q(t)$$
$$a_{ijkl}(t) = 2i\chi_a (1 - \delta_{ik}) \left((-1)^i \alpha^k \alpha^{*i} \right) + 2i\chi_b (1 - \delta_{jl}) \left((-1)^i \beta^{kl} \beta^{*ij} \right) \tag{5.11}$$

where Pij is again the qubit projector onto state $|ij\rangle$, δ_{ij} is the discrete Dirac delta function, $\mathcal{L}_q$ are the qubit only dissipation superoperators defined in Eq. 5.1. Adding the qubit relaxation operators makes this equation no longer exact but is still reasonably valid in the limit $\kappa_a^s, \kappa_b^s \gg \chi_a, \chi_b$ [56]. Note that this equation is not strictly in Lindblad form because the matrix defined by a_{ijkl} is not always positive. This non-Markovian behavior is due to the fact that we only look at the qubits, giving possible revival of coherence because the qubit state looks mixed as long as there are entangled photons still in the cavities.

5.4 Quantum trajectories: Adding measurement back-action

In a real setup one monitors the output field. Due to the fact that information gain causes stochastic back-action to the system and projects it into one of the measurement-operators eigenstates we need to add an extra probabilistic term to the master equation of Eq. 5.1. When the experiment includes a phase-sensitive amplifier, we are effectively monitoring only a single quadrature of the output field. Doing a homodyne measurement with angle θ and measurement efficiency η_m then gives a *stochastic differential equation* in so called Ito form [33] by adding another superoperator L_m representing the stochastic measurement dynamics to the master equation

$$\mathcal{L}_m \rho = \sqrt{\eta_m} \xi(t) \left[M\rho + \rho M^\dagger - \text{Tr}\left(M\rho + \rho M^\dagger\right) \rho \right] \tag{5.12}$$

where $M = e^{i\theta}\left(-\sqrt{\kappa_a^s \eta_l}a + \sqrt{\kappa_b^s}b\right)$ for the full master equation(Eq. 5.1) and in the polaron and reduced master equations (Eq. 5.9 , Eq. 5.11) $M = e^{i\theta}\left(-\sqrt{\kappa_a^s \eta_l}\Pi_a + \sqrt{\kappa_b^s}\Pi_b\right)$, $\xi(t) dt = dW$ is a white noise process satisfying $E[dW] = 0$ and $E[dW(t) dW(s)] = \delta(t-s) dt$. dW is called the *Wiener increment* since its distribution resembles that of a random walk where the variance of the walkers position grows linearly with time. This equation allows for projection of the density operator by the measurement and we can thus obtain single trajectories instead of only the average dynamics at the cost of having to solve this equation many many times for each trajectory. The measured output voltage corresponding to such a trajectory is given by [56]

$$V(t) = \sqrt{\eta_m}\mathrm{Re}\{\langle M \rangle\} + \xi(t) \tag{5.13}$$
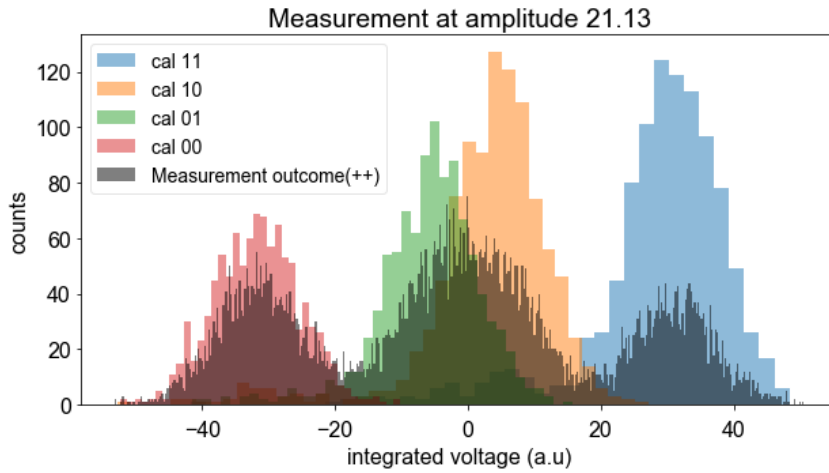
FIGURE 5.3: Example histogram of SME outcomes at high measurement amplitude and typical experimental parameters without the compensation pulse showing the entangling measurement voltage outcomes together with the calibration points. The entangling measurement consisted of 10000 points and the calibration points each of 1000 runs.

5.5   Numerical implementation

The master equation in the polaron or reduced frame (Eq. 5.9,Eq. 5.11) require us to solve a system of 16 coupled linear variable coefficient differential equations. This can be done with any dynamic ODE solving suite in python. A wrapper for solving a general master equation of this type using a variable sized stepper was built and the code can be found on Github.

When solving a non-constant coefficient stochastic differential equation we can no longer use a variable sized stepper, since we need to simulate discrete white noise, the form of which depends on the step-size itself. Solving a stochastic differential equation - Eq. 5.11 with $\mathcal{L}_m$ of Eq. 5.12 added - numerically boils down to generating N_{SME} noise traces for a given time step and then solving Eq. 5.7 N_{SME} times. The average of the trajectories equals the solution to Eq. 5.11 without $\mathcal{L}_m$, but each single trajectory now represents the projection of the measurement.

To speed things up we can use the analytical solution to Eq. 5.7.

$$\rho(t) = \mathcal{T}\left\{ e^{\int_0^t \mathcal{L}(t')dt'} \right\} \rho(0) \approx \prod_{k=0}^{N} e^{\mathcal{L}(t_k)\Delta t} \rho(0) \tag{5.14}$$

where $\mathcal{T}$ denotes the time ordered product and the product on the right represents ordered stepping in time. In the presence of T_1 processes this is necessary since then $\mathcal{L}$ does not commute with itself at different times, but as the time step $\Delta t = \frac{t}{N}$ becomes small enough we can approximate this by dropping the time-ordering operator. In this approach we spend most time in exponentiating L, but the advantage of this approach is that we can now split the stochastic $\mathcal{L}_{SME}$ and the deterministic part $\mathcal{L}_{ME}$ and exponentiate $\mathcal{L}_{ME}$ only once for all time-steps. Then each time-step consists of multiplying ρ with the pre-calculated stepping operator $e^{\mathcal{L}_{me}\delta t}$ and then doing Euler forward for the stochastic part, reducing computation time for the stochastic traces.

6 Results

This chapter will describe the main experimental results in the first three sections. In sec. 6.1 we will show the relation between measurement induced dephasing and distinguishability of the output transients. We will then move to conditioned dynamics giving concurrence data in sec. 6.2. The last main result is the display of driving for an even-parity state given in sec. 6.3. In sec. 6.4 we will discuss the effect of thermal excitation and we will finish with an explanation about how we matched the full two qubit two cavity cascaded model of Chapter 5 to the data in sec. 6.5.3.

6.1 Unconditioned dynamics

The essence of this experiment lies in the relation between measurement induced dephasing and output field distinguishability. To illustrate this relation better, in Fig. 6.1.a, b and 6.1.c we show that as the transient difference goes down between two output fields Y_{ij}, Y_{kl}, so does the dephasing of coherence element ρ_{ijkl}. Doing a perfect half-parity measurement would correspond to zero distinguishability between 01 and 10.

If we do not use the compensation pulse derived in sec. 5.2.1 the distinguishability between Y_{01} and Y_{10} remains non-zero (purple line in Fig. 6.1.a). The distinguishability for states corresponding to dephasing of the qubit on the first chip - e.g. 00-10 and 01-11 - are equal but higher than that on the second chip. This is due to the difference in κ^s between the cavities. In Fig. 6.1.b we show the output transient difference when the compensation pulse is turned on. There is now no distinguishability left between 01 and 10 and the curves for all others except 00-11 overlap, showing we have effectively removed the residual distinguishability in κ^s due to fabrication imperfections. The dephasing corresponding to these transients were also measured by performing state tomography versus the entanglement pulse power in Fig 6.1.c. There we show that indeed as distinguishability goes down between two states, so does the measurement induced dephasing on the coherence between those states. A measure of performance is downward slope of the 01-10 element versus amplitude, this should be minimized while the slope of all others should be as high as possible. Note that the populations were unaffected by the measurement(See appendix B for the complete fitting results) and according to the model dephasing should scale linear with power as long as the critical photon number is not reached inside the cavities.

Using a compensation pulse the dephasing of the 01-10 subspace is reduced but nevertheless still present even though the transient difference is 0. This is due to unavoidable losses in going from one chip to another described by η_l, which is fitted to be 0.88 and losses due to the coherent field leaking out on the transmission port via κ^w or simply being lost via κ^I. It is therefore of crucial importance to have highly asymmetric cavities with a high internal quality factor and minimal photon losses in the line
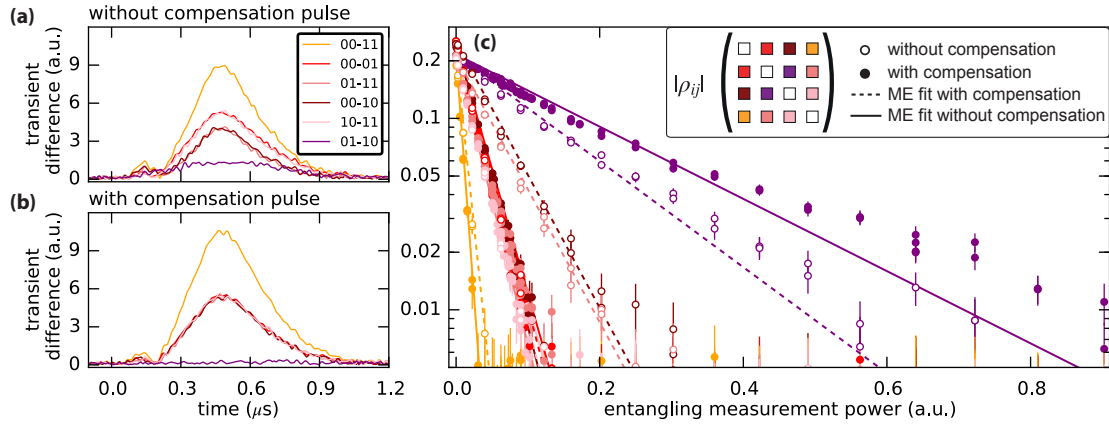
FIGURE 6.1: Transient difference minimization and measurement induced dephasing. (A, B) The 6 transient differences $Y_{ij} - Y_{kl}$ as a function of time of the measured output fields of calibration points for qubits in state 0 or 1 measured with and without the compensation pulse with the JPA turned off. These show a measure of distinguishability between qubit states. (C) Absolute value of the off-diagonal coherence elements in the computational basis versus entanglement measurement strength. The y-scale is logarithmic to indicate the linear increase of measurement induced dephasing. Fits are done on both the amplitude and phase of the 6 off-diagonal elements for all measurement amplitudes simultaneously by the master equation of Eq. 5.1 on just 2 parameters: η_l and an amplitude scaling factor since we had no precise of estimate the power arriving at our chip after attenuation. The many other 14 model parameters were estimated using parameters of independent measurements described in section 3.1. Minimum fidelity of fitted states to measured over the amplitude range was 0.994 not using compensation and 0.992 using compensation.

between the cavities. Losses before reaching the cavities can easily be fixed by ramping up the amplitude, while losses after leaving cavity B before being amplified do not affect the dephasing, but rather the signal to noise ratio (SNR). A lower SNR in turn requires a higher measurement amplitude to be able to select the odd-subspace resulting in an increase in dephasing after all. To create the data of Fig. 6.1.a we tuned up the measurement described in section 3.3.7 to an optimal setting for use without compensation pulse first. Used parameters were $\frac{\Delta_a}{2\pi} \approx 0$MHz (0.2 for no compensation and 0.1 for compensation), $\frac{\Delta_b}{2\pi} = 0$MHz with $f_{meas} = 6.342$GHz since we found an optimal transient difference there. Transients were measured and optimized with the JPA pump turned off. Tomography was performed with the JPA pump turned on using the methods described in sec. 3.3 using maximum likelihood estimation with physicality constraints described in sec. 4.2.2 and corrected for thermal excitations.

6.2 Conditioned dynamics

Being able to perform a near perfect half-parity measurement as described in sec. 1.3.1 is not the whole story. An equally important requirement to obtain a Bell state is the ability to select out measurement outcomes belonging to 00 and 11. In Fig. 6.2.a, you can see that as we increase the measurement strength, while optimizing selection thresholds such that we keep always 25% of the data, we succeed in selecting out the 00, 11 states, while keeping only the 01-10 subspace at an amplitude greater than 0.3mV. Finite remaining 00 population is probably due to relaxation after the 300ns measurement pulse but before the final measurement coming from finite qubit lifetimes during the 700 ns
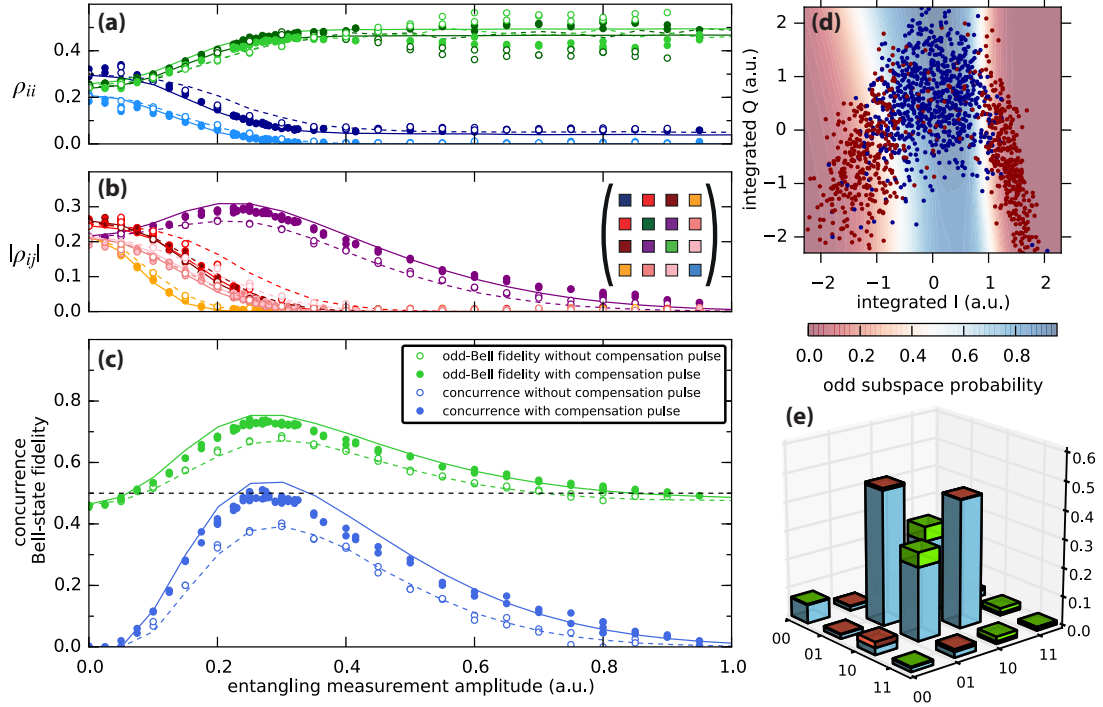
FIGURE 6.2: Same dataset of Fig. 6.2 but now selected on the measurement outcome of the entanglement measurement. Open(closed) dots represent measurement without(with) compensation keeping 25% of the data. (A) Two-qubit state populations versus entanglement amplitude showing an increase in SNR results in better selection. (B) Absolute off-diagonal density matrix elements versus entanglement amplitude showing the selection boosts the 01-10 element while all others go down. (C) Concurrence and odd Bell-fidelity versus amplitude showing three regimes. At first the SNR is too low to select out the 00, 11 outcomes, then we reach a maximal concurrence of $0.40 \pm 0.02(0.51 \pm 0.01)$ for no compensation(compensation) and Bell fidelity of 0.70(0.75) before being dephasing limited due to losses. The inset shows how concurrence scales with the percentage of data kept at the amplitude corresponding to a maximal concurrence. (D) An example set of calibration measurement outcomes in I,Q space used to select the data using a neural network based classification package [70]. Blue points correspond to the odd-parity subspace while the red points are assigned to even parity. (E) Effect of compensation pulse on final density matrix at highest concurrence from (C). Green(red) shows an increase(decrease) of the density matrix using a compensation pulse. Fit were done by doing the stochastic master equation described in Chapter 5.

wait time. The absolute value of the off-diagonal 01-10 element is increased by selection as shown in Fig. 6.2.b but is ultimately limited by the residual dephasing caused by the measurement. This results in an optimal measurement amplitude just after we have selected out the 00 and 11 outcomes corresponding to a maximum in concurrence and odd Bell-fidelity shown in Fig. 6.2.c of 0.40 ± 0.02, 0.70 respectively without using a compensation pulse. Now with the compensation pulse we can increase these numbers since it reduces the dephasing at a similar value of distinguishability. This results in 0.51 ± 0.01 concurrence and 0.75 odd Bell-fidelity, and the effect on the density matrix compared to not using a compensation pulse is shown in Fig.6.2.d.

This data corresponds to the unconditioned data of Fig. 6.1. The JPA was tuned up to maximize readout fidelity separately for the compensated and non-compensated case. This was done because we noticed that the optimum readout parameters change due to the compensation pulse, we have also taken a completely interleaved data set,
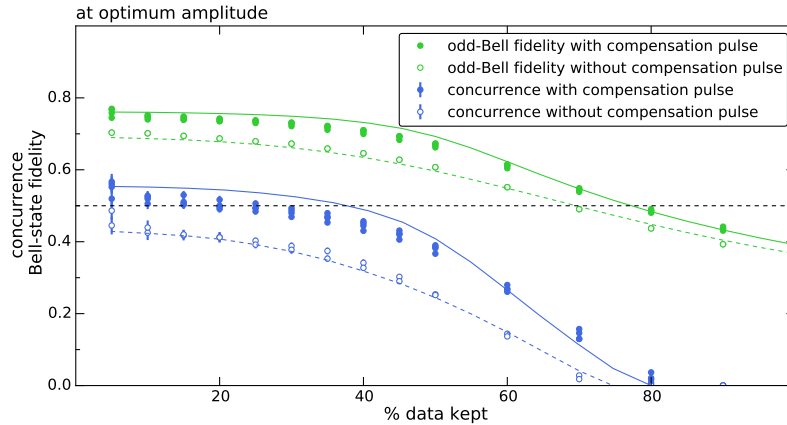
FIGURE 6.3: Concurrence and odd Bell-state fidelity as a function of data kept with(open, dashed) and without compensation pulse(closed, full line). Where the line indicates the stochastic master equation fit. From this we can see the trade-off between the entanglement generation rate and the quality of entangled states. Dashed black line indicates 0.5 as a guide to the eye.

but always found the compensated case to perform better. In order to see the trade-off between the entanglement generation rate and concurrence of the final states we vary the thresholding such that we can keep an arbitrary amount of data, the result is shown in Fig. 6.3. From this you can see that even at 50% data-kept (which is the maximum percentage that is useful due to the half-parity measurement) we have 0.40 concurrence remaining using a compensation pulse and 0.28 not using it. This could be useful in entanglement distillation protocols since the final state concurrence then depends also on the success rate of entanglement generation.

6.3 Driving to an even parity state

Instead of using the compensation pulse to correct the half-parity measurement for fabrication imperfections, we can also change the parity of the entangled state just by changing the shape of the microwave pulse into the weak port of cavity B. This corresponds to the solution of Eq. 5.6 setting $Y_{00} = Y_{11}$. We applied this pulse and changed the JPA tuneup to now maximize readout fidelity between the output fields corresponding to the qubits in 01 and 10. This causes the transient difference to "flip" now making the outputs corresponding to 00 and 11 indistinguishable as shown in Fig. 6.4.c. This then also changes the dephasing as shown in Fig. 6.4.b such that coherence between 00 and 11 remains. In theory this curve should also be linear, but since the even parity measurement is not the natural system measurement, the compensation pulse requires more power than in the odd case. In Fig. 6.4.b concurrence is shown as a function of measurement amplitude showing a concurrence maximum of 0.49 and even Bell-fidelity of 0.72, which is similar to concurrences of odd-parity case.

6.4 Filtering out and correcting for thermal excitation

As described in sec. 4.3.1 thermal excitation can artificially boost the purity of the estimated states from state tomography by skewing your calibration points. On the other
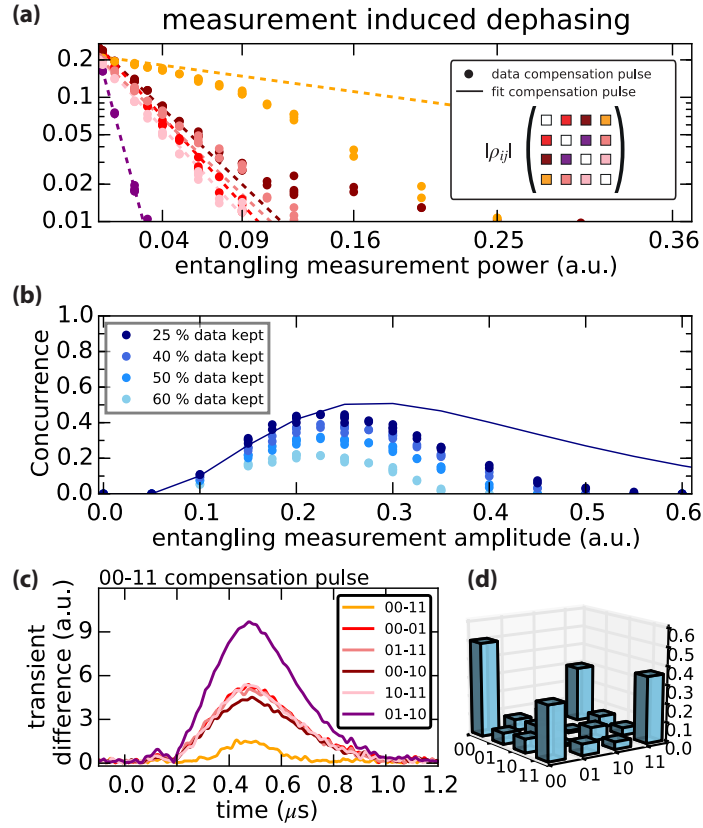
FIGURE 6.4: Even-parity entanglement generation by changing only the shape of the back-port pulse and no other parameters. (A) Off diagonal density matrix elements as a function of measurement amplitude. (B) Concurrence as a function of measurement amplitude for different amount of data kept. Solid line is stochastic master equation result for 25% data kept showing a mismatch due to an imperfect compensation pulse at higher amplitudes. (C) Transient difference versus time. (D) Density matrix histogram of the final state at 25% data kept and at the point of maximum concurrence 0.45 ± 0.01.

hand, if a qubit is thermally excited after our initialization, doing a $Y_{\frac{\pi}{2}}$ rotations causes the qubit to rotate to the $|-\rangle$ state, resulting in an orthogonal Bell state after our experimental protocol, which reduces the concurrence by roughly twice the thermal excitation percentage. Post-selecting on our initial measurement allowed to reduce the upper bound on residual total thermal excitation from 8% to 3% as shown in Fig. 6.5. We however noticed that there seemed to be a flat background in every measurement, which we attributed to the tuning qubits. We therefore implemented a more sophisticated fitting measure that sequentially fits Gaussians to the known means of the 00, 01, 10 and 11 state. In this way we could obtain more precise estimates of the residual thermal excitation fraction in each qubit separately. This was useful in using the correction of sec. 4.3.1 - e.g doing tomography with assumed mixed calibration points instead of pure - since that requires the fractions of each individual qubit. The beneficial effect of post-selecting on the initial measurement on final state concurrence is shown in Fig. B.4. Here we see that comparing the concurrence of selected versus non-selected data always gives an increase in final state concurrence of 8% using the same set of calibration points. We can also see that using the more mixed calibration points results in a skewing of tomography resulting in an overestimate of concurrence by 10% at the maximum, thus at first sight
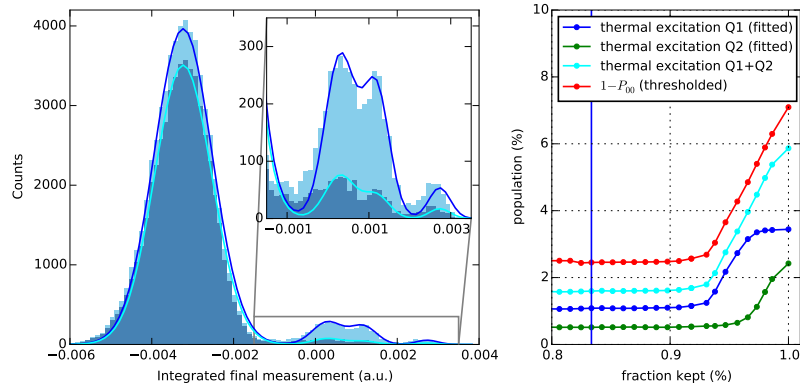
FIGURE 6.5: Thermal excitations present in the qubits in a typical experimental run. On the left a histogram of unselected(selected on the initial measurement, see Fig. 3.8) integrated measurement outcomes of the final measurement of a supposed $|00\rangle$ state is shown in light(dark) blue. Fits are 4 Gaussians fitted to known means and standard deviations of the other calibration points. On the right we show the effect of selection from the pre-measurement on the residual thermally excited qubit populations in the final measurement both from fitting the Gaussians, (green and blue) for qubit one and two, and from an upper bound(red) by just counting everything on the right of a threshold at the tail of the 00 Gaussian. Blue line corresponds to the amount of data kept in the figure on the left.
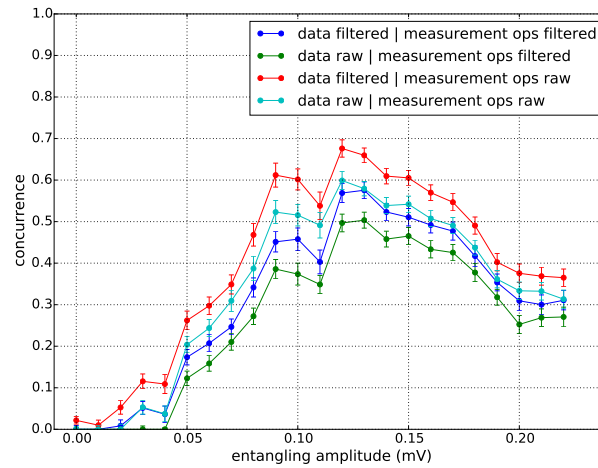
FIGURE 6.6: Cross comparison of concurrence vs entanglement amplitude for data and calibration points filtered by postselecting on the initial measurement. Uncertainties obtained from Monte Carlo simulations. This shows the duality of thermal excitation. On the one hand, filtering your data increases purity and therefore concurrence. On the other hand, having thermally excited calibration points causes the estimated purity to artificially increase.

it would seem like pre-selection actually reduces concurrence by 2%, but that is actually due to the errors in state tomography. This effect is also illustrated on simulated data in Fig. 6.7, where we show that if there is thermal excitation in both the calibration points and the initial state of the protocol, tomography results in giving back a state that looks as if it were unaffected by thermal excitation. But if we use the correction assuming mixed calibration points, we can actually make tomography honest again.

To correct the main results for thermal excitation we estimated the re-excitation rate via a simple rate equation per qubit $\frac{1}{T_{therm}} = \frac{1}{T_1} \frac{E_{ss}}{1-E_{ss}}$ where E_{ss} denotes the excited fraction in steady state(0.034 for qubit A and 0.024 for qubit B on average extracted from the Gaussian fits) resulting in $T_{therm}^a = 504 \ \mu s$, $T_{therm}^b = 374 \ \mu s$ corresponding with a time of 2 μs to 0.004 and 0.0053 expected populations for qubit A and B respectively in the final measurement. In reality this might be bigger due to relaxation during the measurement.
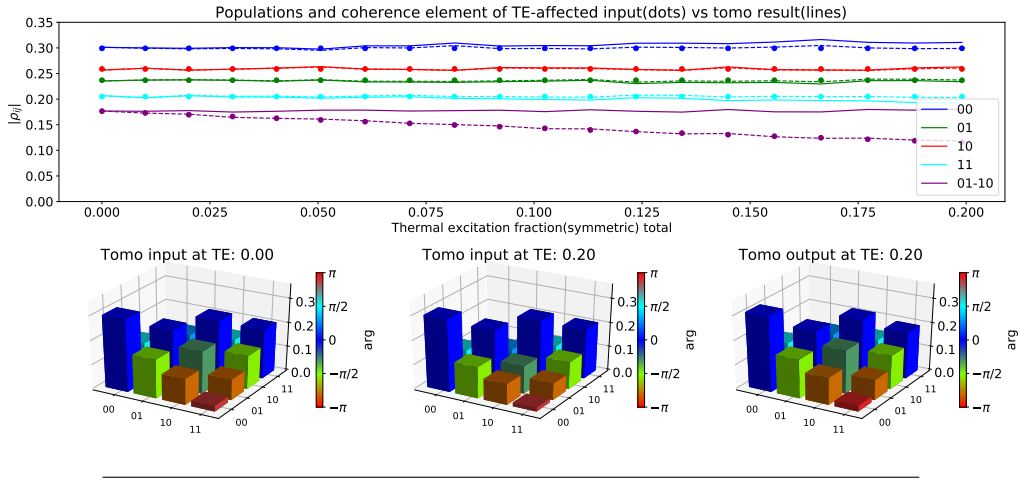
FIGURE 6.7: Simulated input affected by thermal excitation(dots) vs tomography using affected calibration points of those states(lines) and tomography using affected calibration points but *with* the corrected assumption of mixed input states instead of pure(dashed lines). This shows that in presence of thermal excitations the coherence element is much lower in reality than is estimated by tomography if you do not correct for this. The dashed line does follow the real input showing that the correction works given you know how mixed your inputs are. The input is simulated using two $Y_{\frac{\pi}{2}}$ pulses on the thermally excited P_{00} and subsequently evolved using the master equation to simulate our experimental protocol completely.

6.5 Fitting theory to data

6.5.1 Comparing output fields

The compensation pulse was shown to work in reducing the dephasing. A good sanity check is to note if the output field power is linear as a function of input power. We therefore plotted the integrated transients versus output power in Fig. 6.8. Using the amplitude scaling factor obtained from the master equation fit, essentially using the qubits as a photon meter, we plot the intra-cavity photon numbers. Now according to [69] there exists a critical photon number $n_{crit} = \frac{\Delta^2}{4g^2}$ beyond which the dispersive approximation breaks down due to the small term $\frac{g^2}{\Delta}$ in the Taylor expansion used for it no longer being small. For the entanglement qubits, the detuning is large enough so

we never reach n_{crit}, but for the tuning qubits we obtain $n_{crit}Q_{T1} = 50$ and $n_{crit}Q_{T2} = 37$ using the fitted couplings from Fig. 3.6. This could thus make the cavity response non-linear, which is not captured by the model at higher measurement strengths. To further illustrate the creation of distinguishability and confirm our model is working is by fitting the output transients, done in Fig. 6.5.1.
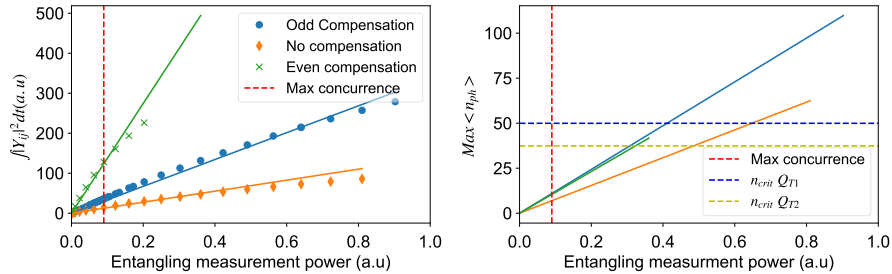
FIGURE 6.8: (Left) Integrated experimental(modeled) transients versus power indicated by dots(lines) for no compensation, odd compensation and even compensation, showing non-linear behavior at high measurement powers. The point of maximum concurrence is far in the linear regime. (Right) Intra-cavity photon number as estimated from the model using fitted amplitude scaling factor from the master equation. Dashed lines indicate relevant critical photon numbers of the tuning qubits, showing that at higher photon numbers the cavity non-linearity due to the tuning qubits can affect the fit quality. Fitted amplitude scaling factors were $1.09*10^{-3}$, $1.15*10^{-3}$, $1.00*10^{-3}$ for no compensation, odd compensation and even compensation respectively found from the transients at maximum concurrence

.

6.5.2   Fitting the master equation

Data shown in Figs. 6.1, 6.2 and 6.4 were taken over a weekend with nearly the same system settings. We therefore started with fitting the unconditioned density matrix evolution versus measurement strength by simulating Eq. 5.11. We used LMFIT to fit the least squared error between elements of the simulated density matrices and density matrices obtained from tomography over the whole amplitude range simultaneously. Fitting a dataset started with estimating T1, T2 by fitting the population elements. We then fit the off-diagonal complex elements using all of the parameters found by independent measurements from table 3.1 and fitting only an amplitude scaling factor for the input amplitude and the loss between the cavities η_l. We then proceeded to using these *same* parameters for fitting the compensation pulse case by turning on a flag in the simulation for doing an even parity or odd-parity compensation pulse. We did re-fit the qubit relaxation and dephasing times T_1, T_2 since they fluctuated between datasets.

In the fitting we found that increasing κ^w, κ^I gave a strong decrease of η_l, this can be explained by the fact that they both represent loss of the photons. The found estimate for the loss $\eta_l \approx 0.89$ should therefore be taken with a grain of salt, but does fall in the regime we would expect based on rough circulator and connector specifications.
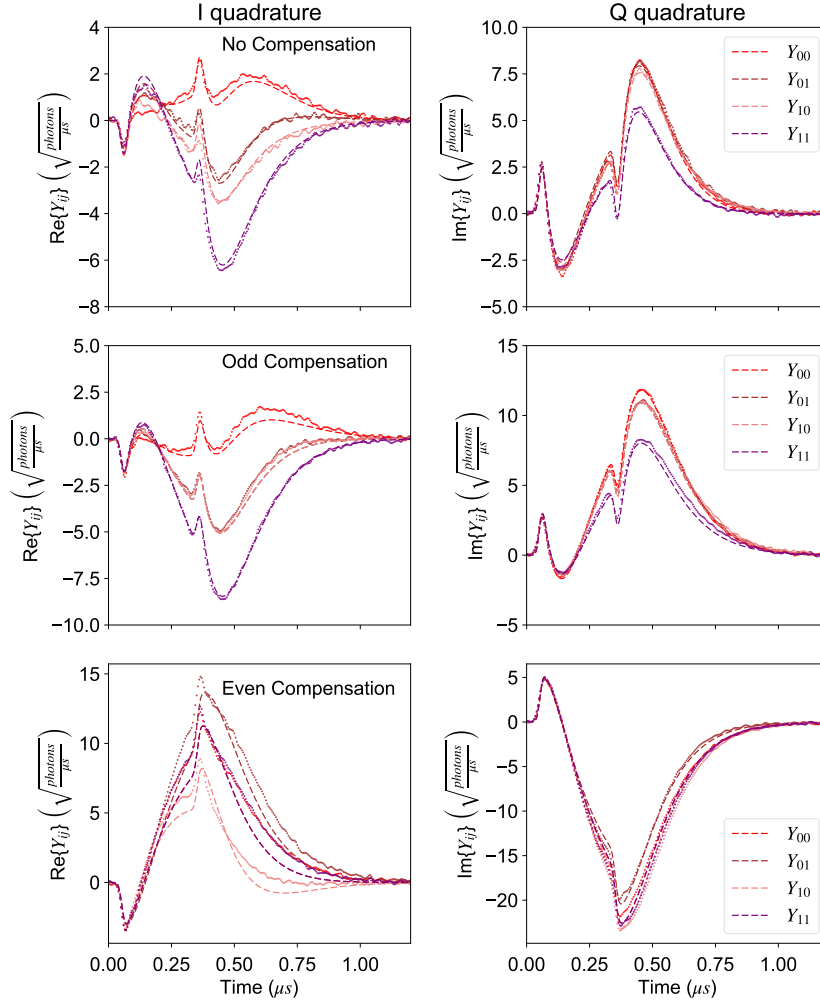
FIGURE 6.9: Output fields in both quadratures of the four calibration points. Dots indicate data plotted every 10ns. Dashed lines indicate predicted transient from the model using the parameters defined in table 3.1 and fitting a phase-offset, output amplitude scale factor and timing offset of 33ns. You can see that using the compensation pulse for the odd-bell state makes the output fields for input state $|01\rangle$ and $|10\rangle$ overlap. The even pulse has the same effect but then makes the $|00\rangle$ and $|11\rangle$ states indistinguishable. Fits of the 00-11 compensation pulse are worse, because the pulse was less wel tuned up as can be seen from the master equation evolution in Fig. 6.4.

6.5.3   Implementation of the stochastic master equation

For fitting the conditioned results, we simulated the stochastic master equation. This consisted for each amplitude of 10000 runs together with 4 times 1000 runs for the calibration points, so we could perform the same thresholding as we did on the experimental data. A homodyne angle of $\frac{\pi}{2}$ was chosen since at 0 Hz detuning most information is in that quadrature and in experiment we optimized the final angle and eventually used 2D thresholding. to the data using the same parameters as found in the master equation. The only remaining unknown was the measurement efficiency, which was determined by running the SME for multiple different efficiencies. A measurement efficiency of 45% agreed well with data not using any compensation pulse. We therefore used it also for the odd and even compensation to show the theoretical maximum concurrence we could have achieved with a perfect compensation pulse, even though the tune-up of the JPA was different, so the measurement efficiency might not have been exactly the same for those cases. Also the phase-sensitive amplification of the JPA is very sensitive to changes in amplitude by definition, so η_{meas} might not have been the same over the whole amplitude range.

7 Conclusion

We have succeeded in generating entanglement by a half-parity measurement on two remote 2D transmon qubits on different chips, by minimizing unwanted measurement induced dephasing in the odd-subspace while maximizing projection strength on the rest. This resulted in generating odd Bell states with $51\%(40\%) \pm 2\%$ concurrence while keeping around $25\%(50\%)$ of our data giving a $1(0.5)$KHz generation rate. This improves on numbers reported in recent literature on similar experiments and was done by tuning the two cavities to have similar output fields for the odd subspace. The tuning was performed by using two tuning qubits to alter the resonator frequency via their dispersive shift. Further matching of the output fields was performed by numerically optimizing a parameterized back port drive based on the solution to the classical equations of motions of the cascaded two-cavity setup. We derived a general compensation pulse solution, allowing us to choose which pair of states to make indistinguishable. This resulted in being able to also project the system in an even parity Bell state reaching similar concurrence.

Data was modeled using numerical simulation of the master equation governing the two qubit two cavity system. By exploiting the cascaded and linear nature of the system, this simulation was reduced to a two-qubit master equation in the polaron frame. This allowed for simultaneous fitting of the full density-matrix over the whole amplitude range. A stochastic master equation was used to model the process of measurement and thresholding. Agreement with theory of the unconditioned result was good in the linear regime with an overall state fidelity $\geq 99\%$. As measurement power increased the output became a slightly non-linear function of the input power and cavity photon numbers inside the cavity reached critical photon numbers making the dispersive approximation used in our models no longer valid, this or non-linearity in the input chain could explain residual mismatch between theory and data.

We also developed a general state tomography toolbox applicable to any system performing single or two qubit measurements. Residual thermal excitation in the qubits was shown to cause two effects. First and foremost, this caused a reduction of final state concurrence due to mixing in orthogonal states. Secondly it skewed the calibration points used in state tomography, causing an overestimate of state purity, which finally resulted in an increase in concurrence. Corrections for these thermal excitations can be done in two ways. At first one should try to do an initialization procedure that selects out the thermally excited states. This will reduce the mixing of orthogonal states after applying the experimental pulses. A second way, to keep the experiment honest if it is impossible to cancel out the residual thermal excitation, is to assume mixed calibration points based on the estimate of residual excitation. This will undo the overestimate of state purity in tomography.

7.1 Suggestions for further research

7.1.1 Improving on loss limits

Given the steady rate of improvements in qubit lifetimes, final state concurrence is fundamentally limited by losses between the cavities (The SME shows that without loss at $\eta_m = 0.45$ between the cavities we should be able to reach 0.82 concurrence, while with infinite qubit lifetimes only 0.65), so minimizing this would be a big improvement. We could for example in our setup remove a circulator between the two cavities and drive the first one in transmission instead of reflection. This would then increase the limit on η_l by circulator losses from 0.93 to 0.96. Another way that has been looked into is using single photons. This has the advantage that the final state concurrence is not limited by losses, but rather the rate of entanglement generation heralded by the measurement. Doing such a scheme for superconducting computer architectures requires single photon detectors at microwave frequencies which are currently not yet reliable enough due to the much lower energy of the photons that need to be detected, but has been attempted recently by Narla et al. [59], reaching a bell state fidelity of 57%.

7.1.2 Distillation and teleportation

We could also improve entanglement between the two distant nodes by adding a second ancilla qubit to perform entanglement distillation. We could then in principle repeat the protocol many times and distill the entanglement to the target bit, but the pure entanglement part of our protocol takes about $1\mu s$ and we have a success rate 25% we would quickly run out of time before the qubit has decayed due to T_1. This can however be optimized extending the use of CLEAR pulses [13] for a joint measurement to ensure a quick decay of the cavities. A more feasible use of the ancilla qubit would be to do teleportation [7] between two chips as fairly recently done in solid state qubits [64]. In this way it is possible to transfer states between two quantum processors, opening up more routes to modular architectures.

7.1.3 Deterministic entanglement

As shown theoretically in [57] it is also possible to generate steady state entanglement using the same chip as we have now. This would alleviate the need for a measurement, initialization and data collection and instead consist of engineering the correct qubit drives such that the steady-state becomes entangled. Direct feedback is another way of generating deterministic entanglement. Since our measurement operator consists of a half-parity measurement we cannot simply do feedback after the full measurement as performed in [67] for example unless we take a "rinse and repeat" approach. We can however make use of the QND continuous weak nature of the measurement to slowly measure the qubit and apply an optimal continuous feedback function based on the measured outcome as proposed in [52].

Acknowledgements

I'm happy to have been part of this group during my masters project. Having people from all over the world together in the Aquarium, yes that's what our lab is called, running around to build a quantum computer was a fun and educating experience. The hard work effort that people had combined with an open mind was nice to work with. I would mainly like to thank Christian, it was nice working together during the last nine months, thanks for your help and even more during the writing of my thesis. I've learned a lot from his inspirational long talks about various subjects - not per se related to our project - and he was always willing to take the time to explain things if asked (which I did a lot). His enthusiasm in making more and more people write for the blog and dedication to make his own articles has showed me that being able to inspire and talk to others about science is almost as important as doing science itself. I would also like to thank Nathan for his help with our project. Even though he wasn't with us for the whole project, his structured way of working and perseverance to make something work or read my report even if it was late at night was a source of inspiration. So I hope you get some sleep there in Australia! Thanks to Ben Kriger for discussions on the compensation pulse and Felix Motzoi for help with the simulation and interesting ideas for the experiment. Furthermore I would like to thank the rest of the lab our time together, thanks to Brian for his nice help and being the go-to guy for discussions about "theory stuff", I think the quality of our work improved when you joined. Oscar, Livio, Ramiro, Thijs and Florian it was a nice time in our side of the lab, although I hope to meet the Luthi-meister one day. Adriaan for our discussions about good coding practice and teaching me the value of a good coffee-walk and finally Leo for his keen eye to clarify and help us focus on the important parts of the research, rather than get lost in trivia.

Last but not least I would like to thank my family, friends and Royaal for their support en Ilse, ook al zat je ver weg, dagdromen over of een slaperige skype-sessie met jou was een welkome afwisseling van het project!

A Generalized hamiltonian

Generalized Jaynes-Cummings Hamiltonian

Even though Eq. 2.15 looks simple, the χ already includes corrections for higher level transmon states. These corrections start affecting χ as the anharmonicity decreases. Now for a single qubit we can write the Transmon Hamiltonian in terms of the bare transmon eigenstates $|j\rangle$ the first order coupling with RWA we arrive at the Generalized n level Jaynes-Cummings Hamiltonian [75]

$$H = \omega_c \hat{a}^\dagger \hat{a} + \sum_{j=0}^{n} \omega_j |j\rangle \langle j| + \sum_{j=0}^{n-1} g_{j,j+1} \left(|j\rangle \langle j+1| + |j+1\rangle \langle j| \right) \left(\hat{a} + \hat{a}^\dagger \right) \qquad \text{(A.1)}$$

where ω_c is the field mode frequency, ω_j is the transmon eigenenergy of level $|j\rangle$, the perturbative dipole coupling strength $g_{j,j+1}$ is given by $\langle j| \hat{n} |j+1\rangle$ where $\hat{n}$ is the charge number operator.

Adding the other qubit

In our 2 qubit two resonator system we can add the second qubit to the system with a similar term to obtain the generalized Tavis Cummings Hamiltonian [75] with a coupling term $J_{12} \left(\hat{\sigma}_-^{(1)} \hat{\sigma}_+^{(2)} + \hat{\sigma}_+^{(1)} \hat{\sigma}_-^{(2)} \right)$ where $J_{12} = \frac{g_1 g_2 (\Delta_1 + \Delta_2)}{2\Delta_1 \Delta_2}$ the qubit qubit coupling through virtual coupling via polarization of the resonator [77]. The qubit qubit term is usually negligible since both $\Delta_1, \Delta_2 >> 1$, but since we vary the tuning qubit in order to tune the resonator we should keep the effect of this hybridization in mind.

The final hamiltonian used for estimating the couplings is then

$$\begin{aligned}
H = {} & \omega_c \hat{a}^\dagger \hat{a} + \sum_{k=0}^{1} \sum_{j=0}^{n} \omega_j^k |j\rangle_k \langle j|_k \\
& + \sum_{k=0}^{1} \sum_{j=0}^{n-1} g_{j,j+1}^k \left(|j\rangle_k \langle j+1|_k + |j+1\rangle_k \langle j|_k \right) \left(\hat{a} + \hat{a}^\dagger \right) \\
& + J_{12} \left(\hat{\sigma}_-^{(1)} \hat{\sigma}_+^{(2)} + \hat{\sigma}_+^{(1)} \hat{\sigma}_-^{(2)} \right)
\end{aligned} \qquad \text{(A.2)}$$

where k denotes the qubit index and n was taken to be 3. This was used to fit the couplings of Fig. 3.6 by diagonalizing it given the measured E_c and α.

B Detailed fitting results

This appendix shows the detailed full-density matrix data used for Figs. 6.1, 6.2, 6.4 where you can see both the deterministic phase gain due to the measurement induced AC-Stark shift and the dephasing. Note that during the measurement the population remained constant. We did however found a small but re-occuring underestimate in the simulated T_1 versus measured T_1 during the data runs of about $2\sigma_{T_1}$, which remains unexplained.
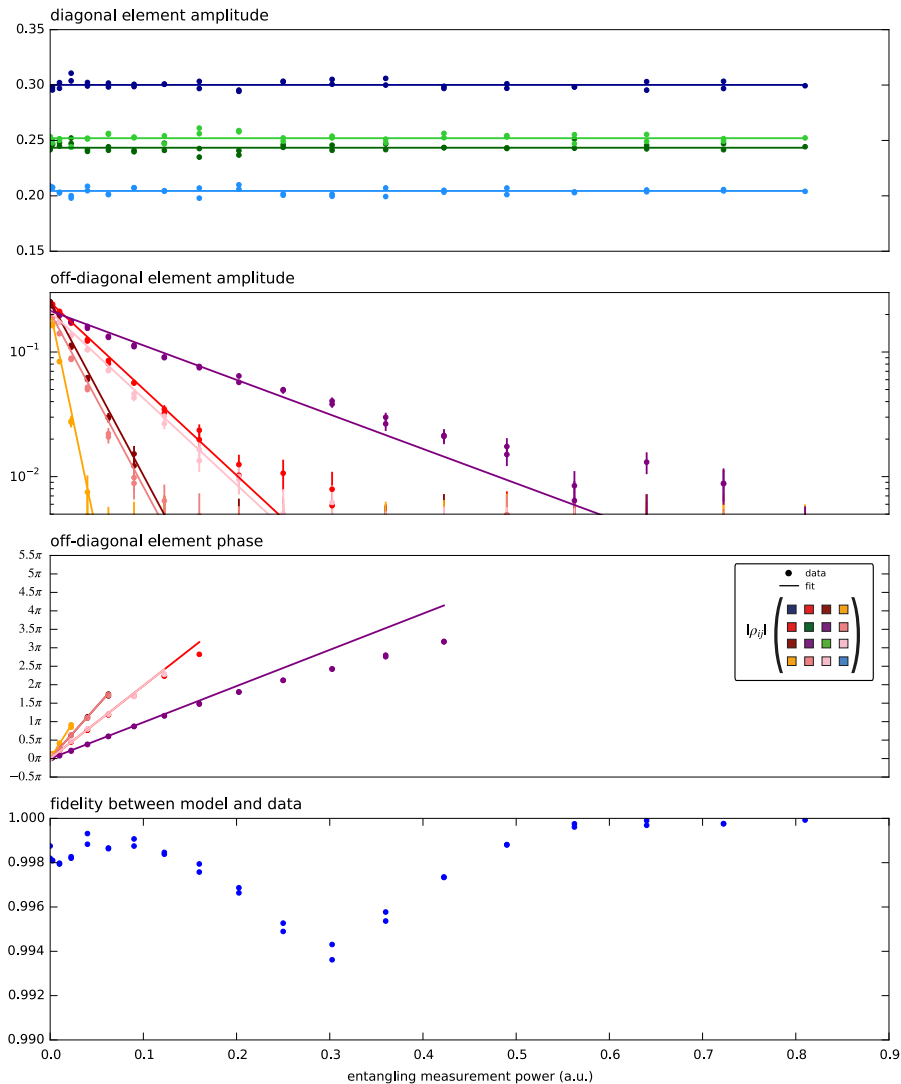
FIGURE B.1: Fit of data not using a compensation pulse. Minimum fit fidelity reported is 0.994 and average over the amplitude range is 0.998 ± 0.002. Error bars obtained from Monte-Carlo simulations on tomography result.
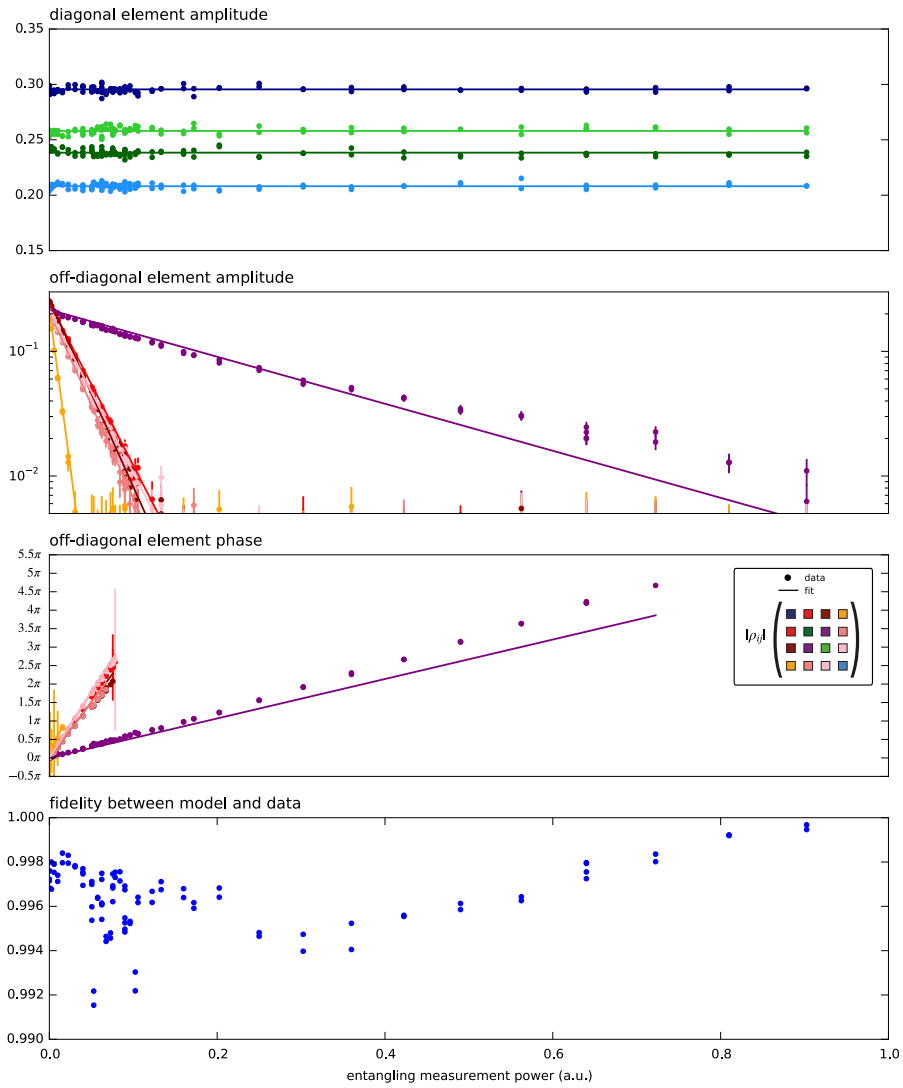
FIGURE B.2: Fitted density matrix data using the odd compensation pulse. Minimum fit fidelity reported is 0.992 and average over the amplitude range is 0.997 ± 0.001. Error bars obtained from Monte-Carlo simulations on tomography result
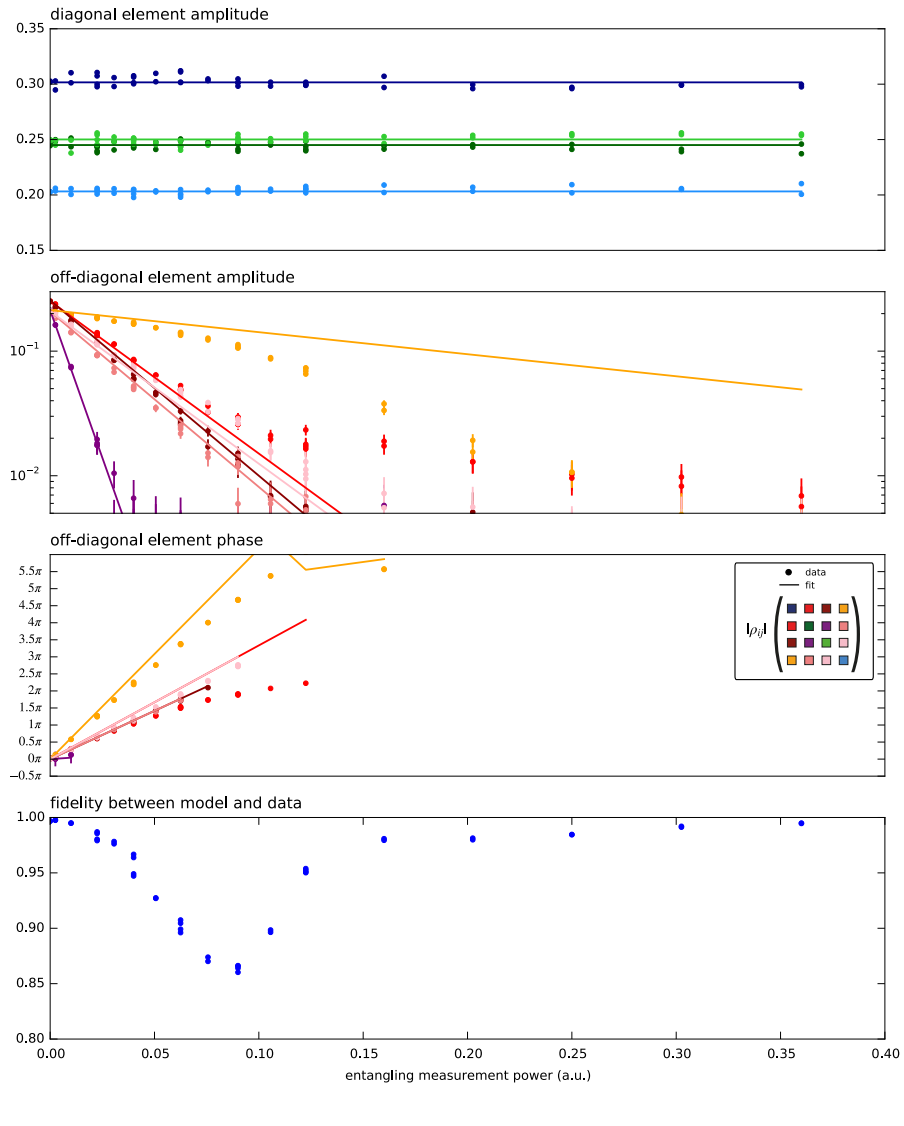
FIGURE B.3: Fitted density matrix data using the even compensation pulse. The model predicts higher coherence than the data, which is probably due to imperfect tuning up of the compensation or due to non-linearities in the input chain. Minimum fit fidelity reported is 0.86 and average over the amplitude range is 0.95±0.05. Error bars obtained from Monte-Carlo simulations on tomography result
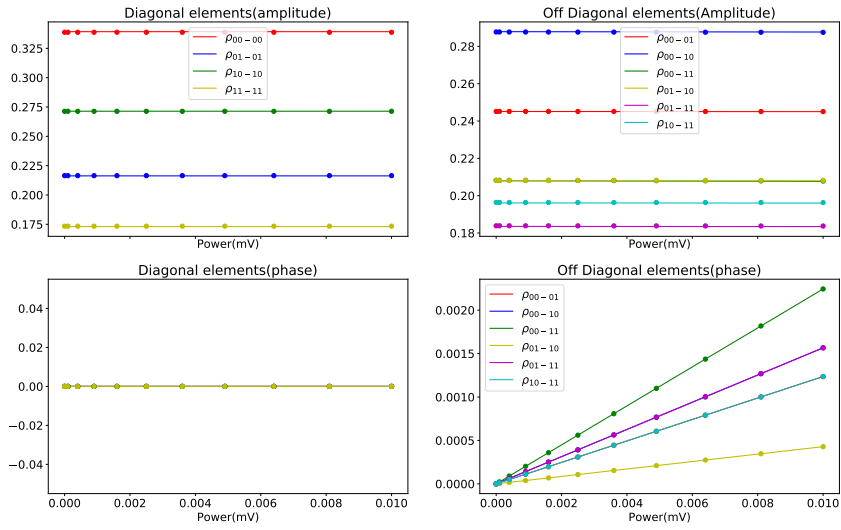
FIGURE B.4: Comparison simulation of the full master equation of Eq. 5.1 including the cavity Fock states with the reduced master equation for experimental settings including decay and decoherence at low measurement amplitudes so we were still able to simulate the full master equation. This was a sanity check to see if the faster reduced master equation produced the same results as the full master equation. Lines indicate the reduced obtained from the polaron transformation and dots indicate result from the full master equation. They agree very well.

Bibliography

[1] A. Bhattacharyya. "On a Measure of Divergence between Two Multinomial Populations". In: *Indian statistical Institute* 7.4 (1946), pp. 401–406.

[2] J. B. Altepeter, D. F. V. James, and P. G. Kwiat. "Qubit Quantum State Tomography". In: *Lect. Notes Phys.* 649 (2004), pp. 113–145.

[3] J. B. Altepeter, E. R. Jeffrey, and P. G. Kwiat. "Photonic State Tomography". In: *Advances in Atomic, Molecular and Optical Physics* 52 (2005), pp. 105–159. ISSN: 1049250X. DOI: 10.1016/S1049-250X(05)52003-2.

[4] J. Bardeen, L. N. Cooper, and J. R. Schrieffer. "Theory of superconductivity". In: *Physical Review* 108.5 (1957), pp. 1175–1204. ISSN: 0031899X. DOI: 10.1103/PhysRev.108.1175.

[5] J. S. Bell. "On the Einstein-Podolsky-Rosen paradox". In: *Physics* 1 (1964), pp. 195–200.

[6] Charles H. Bennett et al. "Mixed-state entanglement and quantum error correction". In: *Phys. Rev. A* 54 (5 1996), p. 3824. DOI: 10.1103/PhysRevA.54.3824.

[7] Charles H. Bennett et al. "Teleporting an unknown quantum state via dual classical and Einstein-Podolsky-Rosen channels". In: *Phys. Rev. Lett.* 70 (1993), pp. 1895–1899.

[8] L. S. Bishop. "Circuit Quantum Electrodynamics". PhD Dissertation. Yale University, 2010.

[9] Alexandre Blais et al. "Cavity quantum electrodynamics for superconducting electrical circuits: An architecture for quantum computation". In: *Physical Review A - Atomic, Molecular, and Optical Physics* 69.6 (2004), pp. 062320–1. ISSN: 10502947. DOI: 10.1103/PhysRevA.69.062320. arXiv: 0402216 [cond-mat].

[10] Alexandre Blais et al. "Quantum-information processing with circuit quantum electrodynamics". In: *Physical Review A - Atomic, Molecular, and Optical Physics* 75.3 (2007), pp. 1–21. ISSN: 10502947. DOI: 10.1103/PhysRevA.75.032329. arXiv: 0612038 [cond-mat].

[11] V Braginsky, Y Vorontsov, and K Thorne. "Quantum Nondemolition Measurements". In: *Science* 209.4456 (1980), pp. 547–557. URL: http://ukpmc.ac.uk/abstract/MED/17756820.

[12] V. B. Braginsky and F. Ya. Khalili. "Quantum nondemolition measurements: the route from toys to tools". In: *Rev. Mod. Phys.* 68.1 (Jan. 1996), pp. 1–11. ISSN: 0034-6861. URL: http://rmp.aps.org/abstract/RMP/v68/i1/p1_1.

[13] C. C. Bultink et al. "Active Resonator Reset in the Nonlinear Dispersive Regime of Circuit QED". In: *Phys. Rev. Appl.* 6 (2016), p. 034008.

[14] H. J. Carmichael. "Quantum trajectory theory for cascaded open systems". In: *Physical Review Letters* 70.15 (1993), pp. 2273–2276. ISSN: 00319007. DOI: `10.1103/PhysRevLett.70.2273`.

[15] M. A. Castellanos-Beltran et al. "Amplification and squeezing of quantum noise with a tunable Josephson metamaterial". In: *Nat. Phys.* 4.12 (Oct. 2008), p. 929. ISSN: 1745-2473. DOI: `10.1038/nphys1090`.

[16] Davide Castelvecchi. "IBM's quantum cloud computer goes commercial". In: *Nature* 543.7644 (2017), pp. 159–159. ISSN: 0028-0836. DOI: `10.1038/nature.2017.21585`. URL: `http://www.nature.com/doifinder/10.1038/nature.2017.21585`.

[17] Davide Castelvecchi. "Quantum computers ready to leap out of the lab in 2017". In: *Nature* 541.7635 (2017), pp. 9–10. ISSN: 0028-0836. DOI: `10.1038/541009a`. URL: `http://www.nature.com/doifinder/10.1038/541009a`.

[18] J. M. Chow et al. "Optimized driving of superconducting artificial atoms for improved single-qubit gates". In: *Phys. Rev. A* 82 (2010), p. 040305.

[19] John Clarke and F. K. Wilhelm. "Superconducting quantum bits". In: *Nature* 453 (2008), p. 1031.

[20] A. A. Clerk, Steven M. Girvin, and a. Stone. "Quantum-limited measurement and information in mesoscopic detectors". In: *Physical Review B* 67.16 (2003), p. 165324. ISSN: 0163-1829. DOI: `10.1103/PhysRevB.67.165324`. arXiv: `0211001 [cond-mat]`. URL: `http://link.aps.org/doi/10.1103/PhysRevB.67.165324`.

[21] D. Deutsch and R. Jozsa. "Rapid solution of problems by quantum computation". In: *Proc. R. Soc. Lond. A* 439 (1992), pp. 553–558.

[22] MH Devoret, A Wallraff, and JM Martinis. "Superconducting qubits: A short review". In: *arXiv:cond-mat/0411174* (). URL: `http://arxiv.org/abs/cond-mat/0411174`.

[23] David P. DiVincenzo. "The physical implementation of quantum computation". In: *Fortschritte der Physik* 48 (2000), p. 771. ISSN: 00158208. DOI: `10.1002/1521-3978(200009)48:9/11<771::AID-PROP771>3.0.CO;2-E`. URL: `http://doi.wiley.com/10.1002/1521-3978\%28200009\%2948\%3A9\%2F11\%3C771\%3A\%3AAID-PROP771\%3E3.0.CO\%3B2-E`.

[24] A. C. Doherty et al. "Trapping of single atoms with single photons in cavity QED". In: *Physical Review A - Atomic, Molecular, and Optical Physics* 63.1 (2001), pp. 1–24. ISSN: 10502947. DOI: `10.1103/PhysRevA.63.013401`. arXiv: `0006015 [quant-ph]`.

[25] Andrew C Doherty, Alexei Gilchrist, and Mark D De Burgh. "Quantum tomography using convex optimisation". In: *Quantum* 1 (2007), p. 11.

[26] J. P. Dowling and G. J. Milburn. "Quantum technology: the second quantum revolution". In: *Philosophical Transactions of the Royal Society A: Mathematical, Physical and Engineering Sciences* 361.1809 (2003), pp. 1655–1674. ISSN: 1364-503X. DOI: `10.1098/rsta.2003.1227`. arXiv: `0206091 [quant-ph]`. URL: `http://rsta.royalsocietypublishing.org/cgi/doi/10.1098/rsta.2003.1227`.

[27] A. Einstein, B. Podolsky, and N. Rosen. *Can Quantum-Mechanical Description of Reality Be Considered Complete?* 1935. DOI: `10.1103/PhysRev.48.696`. arXiv: `0701001 [quant-ph]`.

[28] Artur K. Ekert. "Quantum cryptography based on Bellâs theorem". In: *Physical Review Letters* 67.6 (1991), pp. 661–663. ISSN: 00319007. DOI: `10.1103/PhysRevLett.67.661`. arXiv: `0911.4171v2`.

[29] Richard P. Feynman. "Simulating physics with computers". In: *International Journal of Theoretical Physics* 21.6-7 (June 1982), pp. 467–488. ISSN: 0020-7748. URL: `http://link.springer.com/10.1007/BF02650179`.

[30] S. Filipp et al. "Two-qubit state tomography using a joint dispersive readout". In: *Physical Review Letters* 102.20 (2009), pp. 1–4. ISSN: 00319007. DOI: `10.1103/PhysRevLett.102.200402`. arXiv: `0812.2485`.

[31] Jay Gambetta et al. "Quantum trajectory approach to circuit QED: Quantum jumps and the Zeno effect". In: *Phys. Rev. A* 77.1 (Jan. 2008), p. 012112. ISSN: 1050-2947.

[32] Jay Gambetta et al. "Qubit-photon interactions in a cavity: Measurement-induced dephasing and number splitting". In: *Phys. Rev. A* 74 (4 2006), p. 042318. DOI: `10.1103/PhysRevA.74.042318`. URL: `http://link.aps.org/doi/10.1103/PhysRevA.74.042318`.

[33] C. Gardiner and P. Zoller. *Quantum Noise*. 3rd. Springer, Berlin, Germany, 2004.

[34] Cw Gardiner. "Driving a quanutm system with the output field from another driven quantum system". In: *Physical Review Letters* 70.15 (1993), pp. 2269–2272.

[35] Cw Gardiner and Mj Collett. "Input and output in damped quantum systems: Quantum stochastic differential equations and the master equation". In: *Physical Review A* 31.6 (1985), pp. 3761–3774. ISSN: 0556-2791. DOI: `10.1103/PhysRevA.31.3761`. URL: `http://pra.aps.org/abstract/PRA/v31/i6/p3761{\_}1{\%}5Cnhttp://link.aps.org/doi/10.1103/PhysRevA.31.3761`.

[36] S. M. Girvin. "Superconducting Qubits Coupled to Microwave Photons". In: *Les Houches 2011 Notes*. Oxford University Press, 2012.

[37] J. Gough and M. R. James. "Quantum feedback networks: Hamiltonian formulation". In: *Communications in Mathematical Physics* 287.3 (2009), pp. 1109–1132. ISSN: 00103616. DOI: `10.1007/s00220-008-0698-8`. arXiv: `0804.3442`.

[38] John E Gough. "Principles and applications of quantum control engineering". In: *Philosophical Transactions of the Royal Society A: Mathematical, Physical and Engineering Sciences* 370.1979 (2012), pp. 5241–5258. ISSN: 1364-503X. DOI: `10.1098/rsta.2012.0370`. URL: `http://www.pubmedcentral.nih.gov/articlerender.fcgi?artid=3479716{\&}tool=pmcentrez{\&}rendertype=abstract{\%}5Cnhttp://www.pubmedcentral.nih.gov/articlerender.fcgi?artid=3479717{\&}tool=pmcentrez{\&}rendertype=abstract{\%}5Cnhttp://rsta.royalsocietypublishing.org/cgi/doi/`.

[39] Daniel Greenbaum. "Introduction to Quantum Gate Set Tomography". In: *arXiv:1509.02921 [quant-ph]* (2015). arXiv: `1509.02921`. URL: `http://arxiv.org/abs/1509.02921{\%}5Cnhttp://www.arxiv.org/pdf/1509.02921.pdf`.

[40] Lov K. Grover. "Quantum Mechanics Helps in Searching for a Needle in a Haystack". In: *Phys. Rev. Lett.* 79 (1997), p. 325.

[41] B. Hensen et al. "Experimental loophole-free violation of a Bell inequality using entangled electron spins separated by 1.3 km". In: (2015). ISSN: 0028-0836. DOI: 10.1038/nature15759. arXiv: 1508.05949. URL: http://arxiv.org/abs/1508.05949{\%}0Ahttp://dx.doi.org/10.1038/nature15759.

[42] Scott Hill and William K. Wootters. "Entanglement of a Pair of Quantum Bits". In: *Phys. Rev. Lett.* 78.26 (1997), pp. 5022–5025.

[43] *Inside Microsoft's quest for a topological quantum computer*. https://www.nature.com/news/inside-microsoft-s-quest-for-a-topological-quantum-computer-1.20774.

[44] *Intel bets it can turn everyday silicon into quantum computing's wonder material*. https://www.technologyreview.com/s/603165/intel-bets-it-can-turn-everyday-silicon-into-quantum-computings-wonder-material.

[45] E. T. Jaynes and F. W. Cummings. "Comparison of Quantum and Semiclassical Radiation Theories with Application to the Beam Maser". In: *Proceedings of the IEEE* 51.1 (1963), pp. 89–109. ISSN: 15582256. DOI: 10.1109/PROC.1963.1664.

[46] J.R. Johansson, P.D. Nation, and Franco Nori. "QuTiP: An open-source Python framework for the dynamics of open quantum systems". In: *Computer Physics Communications* 183.8 (2012), pp. 1760 –1772.

[47] B.D. Josephson. "Possible new effects in superconductive tunnelling". In: *Physics Letters* 1.7 (1962), pp. 251–253. ISSN: 00319163. DOI: 10.1016/0031-9163(62)91369-0.

[48] H J Kimble. "The quantum internet." In: *Nature* 453.7198 (June 2008), pp. 1023–30. ISSN: 1476-4687. URL: http://dx.doi.org/10.1038/nature07127.

[49] A. Yu. Kitaev. "Fault-tolerant quantum computation by anyons". In: (1997), pp. 1–27. ISSN: 00034916. DOI: 10.1016/S0003-4916(02)00018-0. arXiv: 9707021 [quant-ph]. URL: http://arxiv.org/abs/quant-ph/9707021{\%}0Ahttp://dx.doi.org/10.1016/S0003-4916(02)00018-0.

[50] Jens Koch et al. "Charge-insensitive qubit design derived from the Cooper pair box". In: *Physical Review A - Atomic, Molecular, and Optical Physics* 76.4 (2007), pp. 1–19. ISSN: 10502947. DOI: 10.1103/PhysRevA.76.042319. arXiv: 0703002 [cond-mat].

[51] N. K. Langford. "Errors in quantum tomography: diagnosing systematic versus statistical errors". In: *New J. Phys.* 15.3 (2013), p. 035003. URL: http://iopscience.iop.org/article/10.1088/1367-2630/15/3/035003.

[52] Leigh Martin et al. "Deterministic generation of remote entanglement with active quantum feedback". In: *Physical Review A - Atomic, Molecular, and Optical Physics* 92.6 (2015), pp. 1–14. ISSN: 10941622. DOI: 10.1103/PhysRevA.92.062321. arXiv: 1506.07888.

[53] P. W. Milonni. "Why spontaneous emission?" In: *American Journal of Physics* 52.4 (1984), p. 340. ISSN: 00029505. DOI: 10.1119/1.13886. URL: http://link.aip.org/link/?AJP/52/340/1{\&}Agg=doi.

[54] C. Monroe et al. "Large Scale Modular Quantum Computer Architecture with Atomic Memory and Photonic Interconnects". In: (2012), pp. 1–16. DOI: `10.1103/PhysRevA.89.022317`. arXiv: `1208.0391`. URL: `http://arxiv.org/abs/1208.0391{\%}0Ahttp://dx.doi.org/10.1103/PhysRevA.89.022317`.

[55] F. Motzoi et al. "Simple Pulses for Elimination of Leakage in Weakly Nonlinear Qubits". In: *Phys. Rev. Lett.* 103 (2009), p. 110501.

[56] Felix Motzoi, K. Birgitta Whaley, and Mohan Sarovar. "Continuous joint measurement and entanglement of qubits in remote cavities". In: *Physical Review A - Atomic, Molecular, and Optical Physics* 92.3 (2015), pp. 1–17. ISSN: 10941622. DOI: `10.1103/PhysRevA.92.032308`. arXiv: `1503.04766`.

[57] Felix Motzoi et al. "Backaction-driven, robust, steady-state long-distance qubit entanglement over lossy channels". In: *Physical Review A - Atomic, Molecular, and Optical Physics* 94.3 (2016), pp. 1–11. ISSN: 10941622. DOI: `10.1103/PhysRevA.94.032313`. arXiv: `1512.03415`.

[58] Y. Nakamura, Yu. A. Pashkin, and J. S. Tsai. "Coherent control of macroscopic quantum states in a single-Cooper-pair box". In: *Nature* 398.April (1999), p. 786. ISSN: 0028-0836. DOI: `10.1038/19718`. arXiv: `9904003 [cond-mat]`. URL: `http://arxiv.org/abs/cond-mat/9904003`.

[59] A Narla et al. "Robust concurrent remote entanglement between two superconducting qubits". In: *Physical Review X* 6.3 (2016). ISSN: 21603308. DOI: `10.1103/PhysRevX.6.031036`. arXiv: `1603.03742`.

[60] J. A. Nelder and R. Mead. "A Simplex Method for Function Minimization". In: *The Computer Journal* 7.4 (1965), pp. 308–313.

[61] J. von Neumann. "Wahrscheinlichkeitstheoretischer Aufbau der Quantenmechanik". In: *Nachrichten von der Gesellschaft der Wissenschaften zu Göttingen, Mathematisch-Physikalische Klasse* 1927 (1927), pp. 245–272. URL: `http://eudml.org/doc/59230`.

[62] Michael a. Nielsen and Isaac L. Chuang. *Quantum Computation and Quantum Information: 10th Anniversary Edition*. 2011, p. 702. ISBN: 1107002176.

[63] Christoph Ohm and Fabian Hassler. "Measurement-induced entanglement of two transmon qubits by a single photon". In: *New Journal of Physics* 19.5 (2017). ISSN: 13672630. DOI: `10.1088/1367-2630/aa6d46`. arXiv: `1508.05104`.

[64] W. Pfaff et al. "Unconditional quantum teleportation between distant solid-state quantum bits". In: *Science* 345.6196 (May 2014), pp. 532–535. ISSN: 0036-8075. URL: `http://www.sciencemag.org/content/345/6196/532`.

[65] *Quantum technology is beginning to come into its own.* `http://www.economist.com/news/essays/21717782-quantum-technology-beginning-come-its-own`.

[66] M. D. Reed. "Entanglement and Quantum Error Correction with Superconducting Qubits". In: May (2013). arXiv: `arXiv:1311.6759v1`.

[67] D Ristè et al. "Deterministic entanglement of superconducting qubits by parity measurement and feedback." In: *Nature* 502.7471 (Oct. 2013), p. 350. ISSN: 1476-4687. DOI: `10.1038/nature12513`.

[68]   N. Roch et al. "Observation of measurement-induced entanglement and quantum trajectories of remote superconducting qubits". In: *Physical Review Letters* 112.17 (2014), pp. 1–18. ISSN: 10797114. DOI: `10.1103/PhysRevLett.112.170501`. arXiv: `1402.1868`.

[69]   D. I. Schuster. "Circuit Quantum Electrodynamics". PhD Dissertation. Yale University, 2007.

[70]   *Scikit-learn, Classification package*. `http://scikit-learn.org/stable/`. Accessed: 2017-09-24.

[71]   Peter W. Shor. "Polynomial-time algorithms for prime factorization and discrete logarithms on a quantum computer". In: *SIAM Journal on Computing* 26 (1997), p. 1484. DOI: `10.1137/S0097539795293172`.

[72]   Matti Silveri et al. "Theory of remote entanglement via quantum-limited phase-preserving amplification". In: *Physical Review A* 93.6 (2016), pp. 1–10. ISSN: 24699934. DOI: `10.1103/PhysRevA.93.062310`. arXiv: `1507.00732`.

[73]   Daniel Adam Steck. "Quantum and Atom Optics". In:

[74]   G. G. Stokes. "On the change of refrangibilit y of light". In: *Philosophical Transactions of the Royal Society of London* 142.January (1852), pp. 463 –562.

[75]   Michael Tavis and Frederick W. Cummings. "Exact Solution for an N-Molecule-Radiation-Field Hamiltonian". In: *Phys. Rev.* 170 (1968), pp. 379–384.

[76]   L. Tornberg and G. Johansson. "High-fidelity feedback-assisted parity measurement in circuit QED". In: *Physical Review A - Atomic, Molecular, and Optical Physics* 82.1 (2010), pp. 1–7. ISSN: 10502947. DOI: `10.1103/PhysRevA.82.012329`.

[77]   L. Tornberg and G. Johansson. "High-fidelity feedback-assisted parity measurement in circuit QED". In: *Phys. Rev. A* 82.1 (July 2010), p. 012329. ISSN: 1050-2947. DOI: `10.1103/PhysRevA.82.012329`.

[78]   Uri Vool and Michel H. Devoret. "Introduction to Quantum Electromagnetic Circuits". In: *arXiv* (2016), p. 1610.03438v1. arXiv: `1610.03438`. URL: `http://arxiv.org/abs/1610.03438`.

[79]   D.F. Walls and Gerard J. Milburn. *Quantum Optics*. 2008, p. 425. ISBN: 3540285733. DOI: `10.1007/978-3-540-28574-8`. URL: `http://books.google.com/books?id=LiWsc3Nlf0kC{\&}pgis=1`.

[80]   H. M. Wiseman and G. J. Milburn. *Quantum Measurement and Control*. Cambridge: Cambridge University Press, 2009.